

**Stellar magnetic activity
from the photosphere to circumstellar
disks**

Dissertation
zur Erlangung des Doktorgrades
des Departments Physik
der Universität Hamburg

vorgelegt von

Stefan Czesla

aus Hamburg

**Hamburg
2010**

Gutachter der Dissertation: Prof. Dr. J. H. M. M. Schmitt
Prof. Dr. E. D. Feigelson

Gutachter der Disputation: Prof. Dr. P. Hauschildt
Prof. Dr. D. Horns

Datum der Disputation: 11.11.2010

Vorsitzender des Prüfungsausschusses: Dr. R. Baade

Vorsitzender des Promotionsausschusses: Prof. Dr. J. Bartels

Dekan der MIN Fakultät: Prof. Dr. H. Graener

Zusammenfassung

Die Erforschung der Sonnenaktivität gehört zu den ältesten Zweigen der Astronomie. Der Fortschritt der Beobachtungstechnik ermöglichte eine Ausdehnung der Aktivitätsstudien weit über die Sonne hinaus in den Bereich der stellaren Aktivität. Die Entwicklung von satellitengestützten Instrumenten erlaubte den Astronomen den Zugriff auf Spektralbereiche, die von der Erdatmosphäre verdeckt werden. Die Erforschung des so erschlossenen Röntgenhimmels gestattet grundlegende Einsichten in die Natur stellarer magnetischer Aktivität, die besonders wertvoll für das Studium junger Sterne sind. Mit der Entdeckung des ersten extrasolaren Planeten vor 15 Jahren begann der rasante Aufstieg des bis dato kleinen, diesen Objekten gewidmeten, Forschungsbereichs zu einem der größten und aktivsten Zweige der Astronomie.

In der vorliegenden Arbeit werden unterschiedliche Aspekte stellarer Aktivität untersucht. Die Themen reichen von dem klassischen Feld der Sonnenflecken über die Erforschung zirkumstellaren Materials mittels reprozessierter Röntgenstrahlung bis hin zur magnetischen Aktivität substellarer Objekte. Die Daten hierzu stammen von CoRoT im Optischen und von *Chandra* im Röntgenbereich.

Zu Beginn wird die optische Lichtkurve des sonnenähnlichen, jedoch jungen Sterns CoRoT-2a im Hinblick auf den Einfluss von Aktivität auf die Transitlichtkurven eines bedeckenden, jupiterähnlichen Planeten untersucht. Des Weiteren wird eine neue Lichtkurveninversionstechnik angewandt, um die Helligkeitsverteilung auf dem Stern zu rekonstruieren.

Stellare Aktivität hat einen signifikanten Effekt auf die Transitlichtkurven, der bei genauer Bestimmung der Planetenparameter nicht vernachlässigt werden sollte. Wir waren in der Lage, die Oberflächenhelligkeitsverteilung des Sterns über ein halbes Jahr hinweg in zwei, durch die Bedeckung des Planeten definierten, Bereichen zu rekonstruieren. Die zugehörigen Karten zeigen einen Stern mit zwei aktiven Längen auf gegenüberliegenden Hemisphären.

Anschließend werden Röntgenquellen einer Sternentstehungsregion im Orion untersucht, die im Rahmen des *Chandra* Orion Ultradeep Project beobachtet wurden. In den Quellen wird nach der Fe K_{α} I Fluoreszenzlinie gesucht und gegebenenfalls ihr Zeitverhalten analysiert. Die vorherrschende Meinung ist, dass die Fe K_{α} I Linienemission auf Photoionisation in beleuchteten zirkumstellaren Scheiben zurückzuführen ist. Dieses Szenario kann mittels des Zeitverhaltens der Linienemission getestet werden.

Die Analyse liefert 23 Quellen, die signifikante Fe K_{α} I Linienemission zeigen. Die zeitliche Variabilität der Fe K_{α} I Linie weist eine große Vielfalt auf. Einige Beobachtungen scheinen der weitverbreiteten These der Anregung durch Photoionisation zu widersprechen, die trotzdem die plausibelste Erklärung für den Ursprung der Linie darstellt, wenn komplexe Geometrien in Erwägung gezogen werden.

Im letzten Teil der Arbeit wird über die Röntgendetektion des ersten bedeckenden Paares Brauner Zwerge berichtet, die auf der Massenskala den Platz zwischen Planeten und Sternen einnehmen. Das untersuchte System ist das erste, in dem die Parameter von Braunen Zwergen genau bestimmt werden können, und nimmt somit eine Schlüsselstellung in der Erforschung der frühen Entwicklung und Aktivität von massearmen Objekten ein.

Die im Rahmen dieser Arbeit präsentierten Studien demonstrieren die enorme Aussagekraft von Lichtkurvenanalysen. Während die Analyse der Fe K_{α} I Linie in stellaren Quellen bereits an die Grenzen des momentan verfügbaren Instrumentariums führt, birgt die Analyse von optischen Helligkeitsverläufen noch großes Potential, da zur Zeit tausende hochwertiger Lichtkurven von den Weltraumobservatorien CoRoT und Kepler beobachtet werden.

Abstract

The study of solar activity is among the oldest branches of astronomy. With the invention of new observation techniques, the scope of activity research was expanded beyond the Sun, giving rise to the field of stellar activity. An important phase of progress was initiated by the development of space-based instrumentation, allowing astronomers to access wavelength regimes obscured by the Earth's atmosphere. The thus opened spectral window of X-rays yields fundamental insights into the nature of stellar magnetic activity, particularly valuable for the study of young stars. No more than 15 years ago, the discovery of the first extrasolar planet sparked the inflation of a virtually nonexistent area of research, which has now evolved into one of the largest and most attractive branches of astronomy, namely that of extrasolar planets.

In this work, stellar activity is investigated from several points of view. The topics reach from the rather classical field of starspots to the study of circumstellar material via reprocessed X-ray light and magnetic activity in substellar objects. The studies are carried out using data from the optical observatory CoRoT and the *Chandra* X-ray observatory.

The starting point is an analysis of the optical light curve of the young, though otherwise solar-like, star CoRoT-2a aimed at studying the influence of stellar activity on the profile of transits caused by an eclipsing Jovian planet. Furthermore, a novel light curve inversion technique is applied to reconstruct the surface brightness distribution of the host star.

Stellar spots on the host star CoRoT-2a are found to have a significant impact on the shapes of the transit light curves, which cannot be neglected in an accurate procedure to determine the planetary parameters. For a continuous span of about half a year, the surface brightness distribution of the host star is simultaneously reconstructed in two distinct regions defined by the surface fraction eclipsed and not eclipsed by the planetary disk during a transit. The corresponding maps show a brightness distribution consistent with the presence of two active longitudes located on opposing hemispheres.

In the following part of the work, X-ray sources in the Orion star forming region, the target of the *Chandra* Orion Ultradeep Project, are searched for fluorescent Fe K_{α} I line emission, which is believed to originate from photoionization in illuminated circumstellar disks. A test for the validity of this formation scenario is provided by the temporal behavior of the line emission. Therefore, the light curve of the fluorescent line is examined in all sources with a detection.

Our analysis reveals 23 sources with significant emission in the Fe K_{α} I line. The temporal behavior of the line shows a large variety, which in some cases seems to contradict the most widely accepted photoexcitation scenario for the formation of the line. Nevertheless, photoexcitation remains the most plausible explanation, if complex source geometries are taken into account.

In the last part of the work at hand, the X-ray detection of the first known eclipsing brown-dwarf binary is reported. Brown dwarfs occupy an intermediate place between planets and stars on the mass scale, and the system under consideration is the first in which accurate parameters can be obtained for the constituents. Thus, it represents a potential landmark system for understanding the early evolution and activity of low mass objects.

The studies presented in this work demonstrate the enormous power of light curve analyses. While the study of the Fe K_{α} I line in stellar sources has probably reached the limits of currently available X-ray instrumentation, it will be interesting to pursue the analysis of optical light curves, because currently thousands of high quality, short cadence light curves are observed by the space-based planet searching missions CoRoT and Kepler.

Contents

1	Introduction - Cornerstones of stellar activity research	1
2	Analyzing photospheric activity in planetary transits	3
2.1	Solar spots	3
2.2	Spotlight on starspots	5
2.2.1	Observations and techniques	5
2.2.2	The most important findings	6
2.3	Planet hunting and stellar activity	7
2.3.1	Hunting planets	7
2.3.2	The CoRoT mission	7
2.4	Planetary transits and stellar activity	8
2.5	Publications	8
2.5.1	My contributions	9
	How stellar activity affects the size estimates of extrasolar planets	10
	A planetary eclipse map of CoRoT-2a. Comprehensive lightcurve modeling combining rotational-modulation and transits	16
	Planetary eclipse mapping of CoRoT-2a. Evolution, differential rotation, and spot migration	23
3	The X-ray perspective of magnetic activity in young stars and their environ- ments	33
3.1	A short history of X-ray astronomy	33
3.2	X-ray instrumentation	33
3.3	The <i>Chandra</i> X-ray observatory	34
3.4	Stars in X-rays	35
3.5	How to study cool material in X-rays	36
3.6	Publications	39
	The nature of the fluorescent iron line in V 1486 Orionis	39
	Puzzling fluorescent emission from Orion	43
3.7	Towards the substellar regime	58
3.8	Publication	59
	Discovery of X-ray emission from the eclipsing brown-dwarf binary 2MASS J05352184- 0546085	59
4	Summary and conclusion	63
5	Outlook	64
5.1	Projects in progress	65

1 Introduction - Cornerstones of stellar activity research

In ancient times, the Sun, the vital source of life on Earth, was perceived as an incarnation of immutable perfection. Nonetheless, thoughtful observers like Chinese astronomers of the Han dynasty or European monks have long noticed impurities on the solar (sur)face, dark spots disturbing the Sun’s perfect symmetry. Yet, it is not before the early 17th century, that we find empirical reports on those spots, and another 200 years passed before the 11 years solar cycle was discovered at the beginning of the 19th century by Samuel Heinrich Schwabe. These early reports mark the first steps into a new branch of astronomy, namely that of solar and stellar activity.

It is the marvelous accident that, in our epoch, the Moon nearly perfectly covers the solar disk during an eclipse to be credited with the next crucial advances in solar studies. In the few minutes of a total eclipse, the extended, filigree outer atmosphere of the Sun becomes visible, which is otherwise so greatly outshone by the photosphere. Subsequently, researchers became increasingly aware of the solar atmosphere, which has remained in scientific focus since. Figure 1 demonstrates the appearance of the outer Sun during an eclipse observed with modern instrumentation.

Curiously, the average temperature of the outer solar atmosphere does not decline with increasing height, as one might naively expect, but it rises. Today, we distinguish between the chromosphere and the corona, with the latter being the outermost, hottest, and most extended layer. The entire outer atmosphere of the Sun is a highly inhomogeneous region (cf., Fig. 1), pervaded by long-lived and evanescent structures (e.g., Roberts 1945; Bohlin et al. 1975). It has long been noted (Hall 2008) that the high level of organization and the

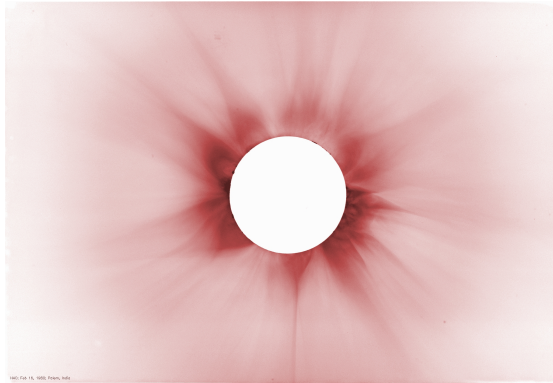


Figure 1: The solar atmosphere observed during an eclipse in 1980 ¹.

temperature structure in the outer Sun point to deviations from radiative equilibrium in these layers, i.e., energy is transported through other channels than radiation. It was only a natural consequence of these findings to search for the processes, collectively referred to as activity², responsible for the surplus of energy in the outer solar atmosphere.

The magnetic field of the Sun was identified as a major key for understanding the properties of the solar atmosphere. The Sun possesses a self-sustaining magnetic field generated via a dynamo process (e.g., Parker 1955a), which can be held responsible for the photospheric solar spots (e.g., Parker 1955b) as well as structures observed in the chromosphere and corona. The magnetic field is rooted in the photosphere, where its evolution is governed by the plasma motion, and it extends into the outer layers of the atmosphere where it, in turn, dominates the plasma motion. In this way, the magnetic field projects plasma motions from the outer solar convection zone into the upper layers of the atmosphere. Beyond a “passive” role as a structural element, the magnetic field also provides a channel for energy transport. The energy stored in the magnetic field can be released via magnetic reconnection (e.g., Priest & Forbes 2000), and, thus, become available as a source of additional heating in the outer atmosphere. Although there seems to be agreement

¹1980 eclipse image courtesy Rhodes College, Memphis, Tennessee, and High Altitude Observatory (HAO), University Corporation for Atmospheric Research (UCAR), Boulder, Colorado. UCAR is sponsored by the National Science Foundation.

²A rigorous definition of this term does not exist.

that magnetic reconnection is a major contributor to the outer solar atmosphere's energy budget and is also the origin of impulsive, violent events called flares, many of its facets remain elusive.

While early studies of activity necessarily concentrated on the Sun, which remains the best studied star because it can be resolved in great detail, the advent of increasingly powerful observation techniques has extended the horizon of activity research far beyond the limits of the solar system. One important observable tracer of the additional heating in the outer stellar atmosphere is the emission reversal in the lines of singly ionized metals as for example Ca II and Mg II. Long term monitoring programs, concentrating on activity indicators, such as the famous Mount Wilson Ca II H&K campaign (e.g., Baliunas et al. 1995) demonstrated that activity comparable to that of our Sun can also be observed in many other late-type stars. The detected activity patterns show a large variety in amplitude and temporal behavior, which ranges from cyclic to erratic, but a general trend indicates a decreasing amplitude of the observed activity in older stars; this decrease in activity is tightly correlated with the loss of stellar angular momentum and is known as the "activity-rotation-age paradigm" (e.g., Skumanich 1972).

Today, the large ground-based observatories are complemented by space-based telescopes, opening our eyes to wavelength bands obscured by the Earth's atmosphere. One of these spectral windows is the X-ray regime with photon energies between several hundred to many thousands of electron Volts. X-ray light is mostly produced in material heated to temperatures of millions of Kelvins or particles accelerated to relativistic energies. Beginning with their first astronomical detection in the early 1960s, the ability of X-ray photons to penetrate large columns of interstellar and intergalactic material caused their growing importance in the study of high energy processes throughout the universe.

In the beginning populated with sparse, strong sources detected with rocket-borne instrumentation, the X-ray sky has become a

crowded place, occupied with sources ranging from galaxy clusters to virtually all kinds of galactic bodies including our Sun. X-rays from late-type stars are predominantly produced in their coronae, so that they serve as a valuable diagnostic of stellar activity. Again, stellar youth was found to be a period of particular activity also in the X-ray regime, making star forming regions preferred targets for X-ray observers.

In 1972 Olin Wilson, the initiator and long-term manager of the Mount Wilson Ca II H&K campaign, noted in a provocative statement: 'It is important to realize that a chromosphere is a completely negligible part of a star. Neither its mass nor its own radiation makes a significant contribution to those quantities of the star as a whole' (Hall 2008); a statement in which one could easily replace chromosphere by corona. While there is a lot of truth in these words, it is also instructive to reveal its shortcoming (which Olin Wilson was of course aware of). While the outer atmospheric layers usually provide a negligible fraction of the stellar energy flux, they may, indeed, provide a major fraction of the energy flux in a specific spectral window such as the X-ray regime. The presence of the stellar magnetic field, among others, establishes an important connection between the processes in the stellar interior deep below the surface and the outer stellar atmosphere. More recently the influence of the stellar magnetic field, high energy radiation, and, thus, activity on the star's surroundings were recognized as a potential key to a better understanding of the evolution of protoplanetary disks, and, therefore, planet formation.

Consequently, the study of stellar activity and, hence, these *almost* negligible outer layers of the stars, can provide us with a better understanding of the star and its evolution as a whole.

2 Analyzing photospheric activity in planetary transits

Sunspots were the earliest known activity indicators, although they were not immediately recognized as such. Much like the lunar eclipse of the Sun promoted our understanding of its outer layers, my collaborators and I now use eclipses by a close-in Jovian planet to better understand the photospheric appearance and evolution of the active star CoRoT-2a.

2.1 Solar spots

Sunspots have been known for a long time, yet their nature remained mysterious for many centuries, and many details are still under debate today. In 1769 Alexander Wilson observed projection effects of sunspots approaching the solar limb, leading him to the conclusion that the spots are, indeed, located on the solar surface and that they constitute slight depressions in the solar photosphere. Since then, our knowledge has increased significantly, and the points most relevant to this work are discussed in the following.

Sunspots are regions on the solar surface, which are cooler than the ambient photosphere and, therefore, appear dark. Figure 2 (upper panel) shows a group of spots on the solar surface observed with SOHO. This picture demonstrates several typical aspects of sunspots. First, they rarely appear individually, but usually occur in spatially associated groups referred to as “active regions”. Second, they show substantial structure: shapes ranging from circular to irregular and a dark core, the umbra, surrounded by a brighter region called the penumbra. The umbra is the coolest part of the spot with an effective temperature ≈ 2000 K lower than that of the photosphere, while the effective temperature of the penumbra is typically only a few hundred Kelvin below photospheric values.

As soon as sunspots appear on the surface, they start to decay. Their lifetimes range from hours to months, with larger spots living longer

on average (e.g., Solanki 2003). The spot distribution on the Sun is not homogeneous, neither in time nor in space. The average area covered by spots varies cyclically with a period of 11 years. During one cycle, not only the spot covered area varies, but also the preferred location of spot appearance changes, migrating from $\pm 30^\circ$ latitude closer to the equator. This behavior is reflected in the famous butterfly diagram shown in the bottom panel of Fig. 2.

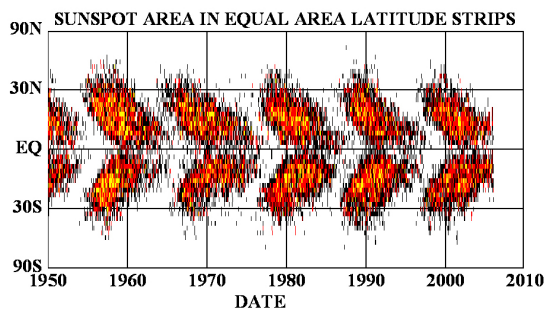
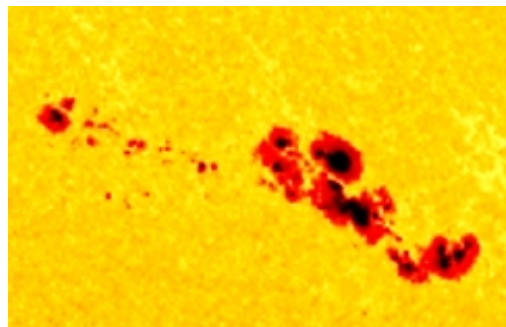


Figure 2: Upper panel: Sunspot group observed by SOHO (Credit: NASA/SOHO). Lower panel: Butterfly diagram showing the sunspot covered area as a function of time (from Solanki 2003).

The above mentioned sunspot phenomenology could long be observed before the attempts to understand it converged into a meaningful physical model of sunspot formation and evolution. It was already emphasized that the solar magnetic field is a key for understanding the structure and heating of the chromosphere and the corona. Yet, the solar dynamo, by which the magnetic field is generated, is mainly localized at the tachocline (cf. Sect. 3.7), which is

located far within the Sun at $\approx 70\%$ of its radius. Thus, there has to be some process bringing magnetic flux from the tachocline to the exterior, whereby it has to cross the intermediate layers.

Sunspots or active regions turned out not only to be distinguished by brightness, but also by increased magnetic field strength: The magnetic field in the umbra reaches $1000 - 5000\text{ G}$ and is nearly perpendicular to the photosphere, while it is weaker and more inclined in the penumbra. Thus, there is strong evidence that we are looking at different incarnations of a common phenomenon no matter whether we analyze the structure and heating of the chromosphere and the corona or we try to understand the origin of sunspots.

A thorough review of the transport processes bringing magnetic flux from the tachocline to the surface of the Sun can, for example, be found in Fan (2009). Although many details remain elusive, the general picture is that magnetic flux associated with the toroidal field of the Sun rises through the outer convection zone concentrated in magnetic flux tubes and eventually penetrates the photosphere. The rise is driven by the force of buoyancy, which originates from extra pressure provided by the magnetic field.

In equilibrium, there must be pressure balance between the ambient gas pressure, p_e , and the pressure within a magnetic flux tube so that

$$p_e = p_i + \frac{B^2}{8\pi}. \quad (1)$$

Here p_i is the gas pressure in the flux tube and the last term describes the magnetic contribution. In an isothermal ideal gas, this leads to a reduced density in the flux tube and, thus, to buoyancy. Although this remains an idealization, it demonstrates the basic idea of buoyancy driven magnetic flux tubes.

Active regions can, thus, be identified with places where rising magnetic flux from the solar interior penetrates the photosphere, but why should this lead to a reduction of the surface effective temperature? The reason for that can already be identified in Fig. 2. Disregarding the spots and concentrating on the ambient pho-

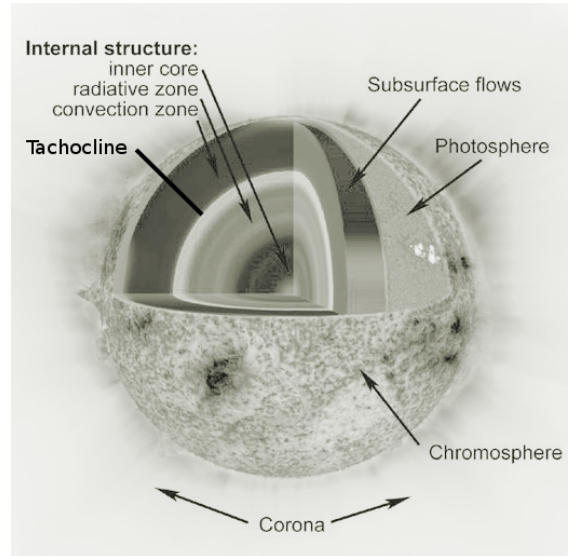


Figure 3: The internal structure of the Sun. Credit: NASA

tosphere, we notice that it has a small scale structure, which turns out to be the result of the energy transport in the outer Sun.

In stars, energy is transported either by convection, radiation, or heat conduction. The dominating process is determined by the environment in different layers of the star. Indeed, Fig. 3 demonstrates that the Sun itself possesses zones in which convective energy transport dominates and zones in which radiative energy transport prevails, while heat conduction is negligible in the solar interior. In particular, energy transport in the layer directly below the photosphere is convective, and the structure observed in the photosphere bears witness to the rise and fall of convection cells transporting energy to the surface.

The magnetic field couples to the ionized plasma in the convection zone and suppresses the motion of the convection cells, ensuing a deficit in energy transport in that region, which we perceive as a solar spot. It should be emphasized at this point that active regions are composed not only of spots, but also of bright structures such as plages and faculae, which are less prominent to the eye, but, on the Sun, overcompensate the brightness loss

due to spots, so that the Sun becomes brighter at spot coverage maximum. This, however, no longer holds for younger, more active stars (e.g., Radick et al. 1998). Needless to stress the connection between observable activity and solar interior again here.

The surface of the Sun is in a state of continuous change. Our present day knowledge reaches far beyond what is discussed above, yet it is not of immediate importance for the work at hand, and I refer the reader to the overview given by Solanki (2003) and references therein for a more complete collection.

2.2 Spotlight on starspots¹

Given the principles of sunspot formation, it is a small step to suggest that also other stars with a structure similar to that of the Sun, in particular, those with an outer convection zone and a magnetic field, should have spots. Today, this idea is commonly accepted, and the study of starspots has evolved into a major tool for understanding stellar structure, activity, and evolution.

In the following, the most important results of starspot studies are summarized, but as this remains an active topic of research there are many details and nuances, which cannot be mentioned, and I refer the reader for example to the reviews by Berdyugina (2005) or Strassmeier (2009) for a more complete overview.

2.2.1 Observations and techniques

In 1947 Kron analyzed the light curve of the eclipsing binary AR Lacertae, in which he noticed asymmetries in the profile of the secondary minimum. Kron (1947) stated the hypothesis ‘that the surface of the G5 star has upon it huge light and dark patches’, and he concluded that a thorough analysis of more data ‘may lead to a better understanding of the sizes, latitudes, and motions of the patches’. Although the hypothesis of starspots had been

¹I note that the term starspot is used here to refer to individual starspots as well as to active regions, where spots emerge and decay, because both can usually not be distinguished on other stars than the Sun.

around for hundreds of years already (see Hall 1994, for an overview of the history of starspot discovery), the work of Kron is now considered the first to have reported on the discovery of starspots, and many more were to come.

In a search for continuum variability among solar-like stars, Radick et al. (1983) found positive results for stars with spectral type K2–F7 within their limits of accuracy. Although Radick et al. (1983) claim physical reality neither for the K2 nor the F7 limit, their outcomes fit well into the picture of stars with outer convection zones having spots, if we attribute the variability to starspots.

For an in-depth analysis of starspots, it is necessary to resolve stellar surfaces in some detail. As direct imaging of stellar surfaces is today only possible in exceptional cases such as Betelgeuse (Young et al. 2000), several indirect techniques are applied to achieve this goal.

One of those is “Doppler Imaging” (e.g., Deutsch 1958; Vogt et al. 1987; Piskunov et al. 1990), in which the distortion of spectral-line profiles is used to reconstruct the brightness distribution on the stellar surface. Doppler Imaging requires high cadence, high resolution spectra with good phase coverage, and its application is, thus, limited to bright, fast rotating stars. Figure 4 shows an example of a Doppler Image derived for the star V889 Her by Huber et al. (2009b).



Figure 4: Doppler Images of V889 Her from Huber et al. (2009b).

Another technique is that of “light curve inversion” (e.g., Vogt 1981; Rodono et al. 1986), exploiting the influence of starspots on the stellar continuum emission to reconstruct its surface. Obtaining light curves is observationally

less challenging than obtaining the high resolution spectra needed to carry out Doppler Imaging, yet, they also contain less information. The reason for this is that a distortion of a spectral-line profile contains information on the radial velocity of the disturbing pattern, encoded in its position within the profile, whereas light curves lack this information. In a recent study of Huber et al. (2009b), it was, however, demonstrated that radial velocity measurements, carried out simultaneously with the photometric observations, can partly replace the information not contained in the light curve alone.

No matter whether Doppler Imaging or light curve inversion are used, the problem usually remains ill-posed, and a regularization is applied to limit the size of the solution space. Common approaches are the Tikhonov regularization (e.g., Piskunov et al. 1990) or a maximum entropy approach (e.g., Vogt et al. 1987).

Other techniques to study starspots comprise Zeeman Doppler-Imaging, combining the analysis of Doppler shifts and Zeeman splitting of spectral lines to recover the distribution of the stellar magnetic field (Semel et al. 1993; Donati et al. 1989), the modeling of molecular bands, which is based on the fact that certain molecular lines can only be formed in the cool spot region of a surface and not in the ambient photosphere (Vogt 1979), and the method of line depth ratios (Gray 1996; Catalano et al. 2002), being also based on the formation conditions for spectral lines in environments of different temperature.

All of these techniques have contributed to the picture of starspots, we have today.

2.2.2 The most important findings

While sunspots typically cover far less than 1 % of the solar surface, it was found that many stars show much larger spot coverages, reaching considerable fractions of the surface. Enormous photometric amplitudes of 0.63 mag were observed for the RS CVn stars II Peg (Tas & Evren 2000) and HD 12454 (Strassmeier 1999). In the latter case, the authors also report on strong color changes accompanying the pho-

tometric variability, indicating that cool spots cover approximately 20 % of the stellar surface or 40 % of the visible disk.

In their analysis of spot coverage and temperature among 5 active, evolved stars, O’Neal et al. (1996) find spot coverage factors between virtually zero and ‘just under 60 %’, with some of their filling factors considerably exceeding previously published values. However, the method of O’Neal et al. (1996) is sensitive not only to the asymmetric² spot coverage, but also to the symmetric part, which usually cannot be recovered with methods such as light curve inversion³ or Doppler Imaging. Thus, the authors conclude that some stars are spotted also during brightness maximum. Symmetric spot contributions may be present in the form of a homogeneously distributed population of smaller spots, or a large, persistent polar spot as for example in the case of V889 Her (see Fig. 4).

Analyses of the starspot lifetime are impeded by our (current) inability to distinguish between individual starspots evolving as units and active regions, where individual spots emerge and decay continuously. Hall (1994) studied 112 starspots on 26 stars and found lifetimes of the order of several days consistent with sunspot values. He concluded that the spot lifetime is determined by maximum spot area for small spots and limited by shear due to differential rotation for large spots. In contrast to this, other starspots seem to be much more persistent lasting for hundreds of days (e.g., Huber et al. 2009b) or years (e.g., Hatzes 1995).

One prominent starspot configuration, found in many active stars, is that of “active longitudes”, i.e., longitudes at which starspots preferentially appear. In RS CVn stars active longitudes were for instance reported on by Zeilik et al. (1988) and Henry et al. (1995), in FK Com stars by Jetsu et al. (1993), and in young, active solar analogs by Berdyugina

²The terms asymmetric and symmetric refer to the longitudinal distribution of spots on the stellar surface. The symmetric fraction of the spot distribution causes no variations in the stellar continuum light curve.

³See Huber et al. (2009a) for an example where it can be done.

et al. (2002). Active longitudes seem to be preferentially separated by $\approx 180^\circ$, i.e., located on opposing hemispheres, and a periodic switching of the amplitude of spot emergence from one hemisphere to the other was also observed in several stars; FK Com is the prototype for this so called “flip-flop” effect (Jetsu et al. 1993).

Today, starspots are believed to be common on active stars, and coverage fractions may exceed that of the Sun by orders of magnitude in the most active stars. Prominent starspot characteristics such as the presence of polar spots, the existence of active longitudes, and the flip-flop effect have been established for many stars, while the physical origin of these features remains debated.

2.3 Planet hunting and stellar activity

Within the last 15 years planetary science has grown into a major branch of astronomy. Many current and upcoming space missions are devoted to finding and studying extrasolar planets and planetary systems, and the attraction of the field is still increasing. While it remains the clearly stated goal of this effort, and one of the most natural desires of mankind, to find a second Earth, the giant wake of this science driver provides data en masse, allowing for extensive research on many other topics.

2.3.1 Hunting planets

Planets usually only produce negligible amounts of optical light, so that they can more easily be detected via their influence on other bodies, most notably their host stars.

One of the techniques exploiting this concept is the “radial velocity method”. Though the host star is, by definition, much more massive than a planet orbiting it, the planet nonetheless exerts a force of gravitational attraction on the host star, and, given a two body system, both will orbit the common barycenter. The radial velocity method is used to detect the planet-induced, periodic motion of the host star by the analysis of Doppler

shifts of spectral lines.

As signals with larger amplitude are usually easier to detect than weak signals, also the radial velocity method is most effective in finding those planets causing the most substantial host-star motions; in particular, this favors the discovery of close-in planets with a large mass.

Indeed, the first extrasolar planet reported on was such an object, 51 Pegasi b (Mayor & Queloz 1995), a Jovian mass planet orbiting the host star in a 4.2 d orbit at a distance of 0.05 AU. 51 Peg b was the first in the new class of “hot Jupiters”, a type of planet (fortunately) not existing in the solar system and, with few exceptions (e.g., Struve 1952), not widely foreseen by the scientific community. Today more than 400 such planets are known, and their number increases virtually every day.

The discovery of 51 Pegasi b and, thus, the class of hot Jupiters, provided substantial support for the rise of another technique of planet search, which is the “transit method”. Planetary transits are a well known phenomenon in the solar system, as both Mercury and Venus have often been observed to cross the solar disk. As the planets are much cooler than the solar photosphere, the apparent solar disk diminishes in brightness for the time of transit. Yet, the probability of finding any planet resembling one in our solar system via a transit was regarded as too low for the transit method to be of any practical relevance; this changed radically when astronomers became aware of hot Jupiters.

Ironically, a more than a thousand years old misinterpretation of a crossing solar spot as another transiting planet, is still a serious complication in detecting transits of extrasolar planets today. Signals resembling those caused by planets, whether in the photometry or the radial velocity, may be feigned by stellar activity, and as the planets under scrutiny approach Earth size, it becomes more and more complicated to uniquely identify planets.

2.3.2 The CoRoT mission

In order to detect Earth sized planets via the transit method, relative photometric accuracies of 10^{-5} need to be reached, which is hardly

possible from the ground mainly because atmospheric disturbances interfere with the measurements. Therefore, the space-based observatory CoRoT (CONvection ROTation and planetary Transits) was launched and successfully put in operation on December 27th, 2006 (Auvagne et al. 2009).

CoRoT basically consists of an optical telescope with a diameter of 27 cm. Its mission is to simultaneously monitor the brightness of several thousand stars and provide approximately half year long, continuous photometry of several fields in the sky with unprecedented time coverage, accuracy, and temporal cadence. The scientific goals of CoRoT are the search for extrasolar planets, of which it has discovered at least seven so far, and asteroseismological studies.

2.4 Planetary transits and stellar activity

Usually stellar activity is considered not much more than an annoying source of noise during the search for extrasolar planets, however, ‘one astronomer’s noise, is the other astronomer’s signal’⁴.

The profile of a planetary transit light-curve is determined by the properties of the planet as well as by the properties of the star. The brightness distribution on the stellar disk gives rise to a characteristic transit profile. Even when a star is perfectly inactive without any spots or faculae, the visible stellar disk is not homogeneously bright, because of limb darkening (Mandel & Agol 2002). The upper panel of Fig. 5 shows an image of the Sun, demonstrating the effect of limb darkening on the brightness distribution of the stellar disk, and the lower panel shows transit light-curves for three different cases of linear limb darkening, indicating the response of the transit light curve to changes of the disk brightness distribution.

If the star is active and has starspots, they influence the surface brightness distribution and, therefore, the transit profile (Silva 2003; Wolter et al. 2009). When a planet crosses

⁴A. Hatzes during a lecture on planetary transit on May 11th, 2010 in Hamburg.

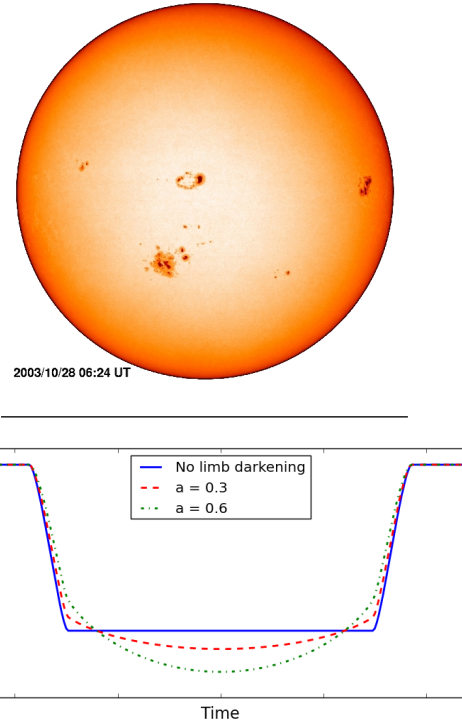


Figure 5: Upper panel: SOHO picture of the Sun; Credit: NASA/ESA. Lower panel: Transit profiles for different coefficients of linear limb darkening.

the stellar disk, it occults different parts of it at different times. As the transit profile is proportional to the amount of light blocked by the planet during its disk passage, the disk’s brightness distribution along the planetary path is encoded in the transit profile and can potentially be recovered.

The following publications represent a confluence of planetary science and stellar activity research and demonstrate the wealth of information, which can be extracted from photometry obtained during transit searches.

2.5 Publications

In the following pages I reproduce three works (Czesla et al. 2009; Huber et al. 2009a, 2010) on CoRoT-2, which were published in *Astronomy & Astrophysics*.

2.5.1 My contributions

In each paper included in this thesis, at least two authors are listed. In this section, I give an overview of my contributions to the works on CoRoT-2, especially for those works where I am not listed as the first author. The works on CoRoT-2 are the result of a collective effort, and it would neither be fair nor correct to attribute individual sections exclusively to me (or another collaborator). I will, therefore, rather outline where I provided major contributions, and where not.

All works on CoRoT-2 can be traced back to an idea promoted by my college and friend Klaus F. Huber, who is also (co)author of all of the papers. From the beginning he wanted to model the light curve and the transits simultaneously. During the early phase of this effort, we noticed that the previously published planetary parameters for CoRoT-2b are not appropriate for our purpose, which was the starting point of Czesla et al. (2009); I provided major contributions to all parts of this work.

Sometime during the work, an accident happened to me, which forced me to stay at home for a few weeks. In this time Klaus Huber frequently visited me at home, where we set up the computer code, which was later used to carry out the light curve modeling. It is due to my larger experience in programming and the programming language c++ in particular, that I can claim a major role in setting up the code. I think that Klaus and I provided approximately equal contributions to Huber et al. (2009a). The major part of Huber et al. (2010) was contributed by Klaus Huber, yet, I also have a share in every part of the work.

I shall not forget to note that also the other coauthors provided contributions to the works, which I, however, will not name in detail here.

How stellar activity affects the size estimates of extrasolar planets

S. Czesla, K. F. Huber, U. Wolter, S. Schröter, and J. H. M. M. Schmitt

Hamburger Sternwarte, Universität Hamburg, Gojenbergsweg 112, 21029 Hamburg, Germany
 e-mail: stefan.czesla@hs.uni-hamburg.de

Received 8 May 2009 / Accepted 1 July 2009

ABSTRACT

Light curves have long been used to study stellar activity and have more recently become a major tool in the field of exoplanet research. We discuss the various ways in which stellar activity can influence transit light curves, and study the effects using the outstanding photometric data of the CoRoT-2 exoplanet system. We report a relation between the “global” light curve and the transit profiles, which turn out to be shallower during high spot coverage on the stellar surface. Furthermore, our analysis reveals a color dependence of the transit light curve compatible with a wavelength-dependent limb darkening law as observed on the Sun. Taking into account activity-related effects, we redetermine the orbit inclination and planetary radius and find the planet to be $\approx 3\%$ larger than reported previously. Our findings also show that exoplanet research cannot generally ignore the effects of stellar activity.

Key words. techniques: photometric – stars: activity – starspots – stars: individual: CoRoT-2a – planetary systems

1. Introduction

The brightness distribution on the surface of active stars is both spatially inhomogeneous and temporally variable. The state and evolution of the stellar surface structures can be traced by the rotational and secular modulation of the observed photometric light curve. In the field of planet research, light curves including planetary transits are of particular interest, since they hold a wealth of information about both the planet and its host star.

The outstanding quality of the space-based photometry provided by the CoRoT mission (e.g., [Auvergne et al. 2009](#)) provides stellar light curves of unprecedented precision, temporal cadence and coverage. While primarily designed as a planet finder, the CoRoT data are also extremely interesting in the context of stellar activity. [Lanza et al. \(2009\)](#) demonstrated the information content to be extracted from these light curves in the specific case of CoRoT-2a. This star is solar-like in mass and radius, but rotates faster at a speed of $v \sin(i) = 11.85 \pm 0.50 \text{ km s}^{-1}$ ([Bouchy et al. 2008](#)). Its rotation period of ≈ 4.52 days was deduced from slowly evolving active regions, which dominate the photometric variations. Thus, CoRoT-2a is a very active star by all standards. Even more remarkably, CoRoT-2a is orbited by a giant planet ([Alonso et al. 2008](#)), which basically acts as a shutter scanning the surface of CoRoT-2a along a well defined latitudinal band.

The transiting planetary companion provides a key to understanding the surface structure of its host star. While previous analyses have either ignored the transits ([Lanza et al. 2009](#)) or the “global” light curve ([Wolter et al. 2009](#)), we show that there is a relation between the transit shape and the global light curve, which cannot generally be neglected in extrasolar planet research.

2. Observations and data reduction

[Alonso et al. \(2008\)](#) discovered the planet CoRoT-2b using the photometric CoRoT data (see Table 1). Its host star has a spectral type of G7V with an optical (stellar) companion too close

Table 1. Stellar/planetary parameters of CoRoT-2a/b.

Star ^a	Value \pm Error	Ref. ^b
P_s	$(4.522 \pm 0.024) \text{ d}$	L09
Spectral type	G7V	B08
Planet ^c	Value \pm Error	Ref.
P_p	$(1.7429964 \pm 0.0000017) \text{ d}$	A08
T_c [BJD]	$(2454237.53362 \pm 0.00014) \text{ d}$	A08
i	$(87.84 \pm 0.10)^\circ$	A08
R_p/R_s	(0.1667 ± 0.0006)	A08
a/R_s	(6.70 ± 0.03)	A08
u_a, u_b	$(0.41 \pm 0.03), (0.06 \pm 0.03)$	A08

^a P_s – stellar rotation period; ^b taken from [Lanza et al. \(2009\)](#) [L09], [Alonso et al. \(2008\)](#) [A08], or [Bouchy et al. \(2008\)](#) [B08]; ^c P_p – orbital period, T_c – central time of first transit, i – orbital inclination, R_p, R_s – planetary and stellar radii, a – semi major axis of planetary orbit, u_a, u_b – linear and quadratic limb darkening coefficients.

to be resolved by CoRoT. According to [Alonso et al. \(2008\)](#), this secondary contributes a constant $(5.6 \pm 0.3)\%$ of the total CoRoT-measured flux. CoRoT-2b’s orbital period of ≈ 1.74 days is about one third of CoRoT-2a’s rotation period, and the almost continuous CoRoT data span 142 days, sampling about 30 stellar rotations and more than 80 transits. The light curve shows clear evidence of strong activity: there is substantial modulation of the shape on timescales of several days, and the transit profiles are considerably deformed as a consequence of surface inhomogeneities ([Wolter et al. 2009](#)).

Our data reduction starts with the results provided by the CoRoT N2 pipeline (N2_VER 1.2). CoRoT provides three-band photometry (nominally red, green, and blue), which we extend by a virtual fourth band resulting from the combination (addition) of the other bands. This “white” band is, henceforth, treated as an independent channel, and our analysis will mainly refer to this band. It provides the highest count rates and, more

importantly, is less susceptible to instrumental effects such as long-term trends and “jumps” present in the individual color channels.

In all bands, we reject those data points flagged as “bad” by the standard CoRoT pipeline (mostly related to the South Atlantic anomaly). The last step leaves obvious outliers in the light curves. To remove them, we estimate the standard deviation of the data point distribution in short (≈ 3000 s) slices and reject the points more than 3σ off a (local) linear model. Inevitably, we also remove a fraction of physical data (statistical outliers) in this step, but we estimate that loss to be less than a percent of the total number of data points, which we consider acceptable.

In all bands apart from the white, we find photometric discontinuities (jumps), which are caused by particle impact on the CoRoT detector. In the case of CoRoT-2a, the jumps are of minor amplitude compared to the overall count rate level, and we correct them by adjusting the part of the light curve following the jump to the preceding level.

Finally, we correct the CoRoT photometry for systematic, instrumental trends visible in all bands apart from white. To approximate the instrumental trend, we fit the (entire) light curve with a second order polynomial, q , and apply the equation

$$c_{\text{corr},i} = c_{o,i} \cdot \frac{\bar{c}}{q_i}, \quad (1)$$

where $c_{o,i}$ is the i th observed data point, q_i is the associated value of the best-fit second order polynomial, \bar{c} represents the mean of all observed count rates in the band, and $c_{\text{corr},i}$ the corrected photometry.

The resulting light curve still shows a periodic signal clearly related to the orbital motion of the CoRoT satellite. This is again a minor effect in the white band, and we neglect this in the context of the following analysis.

In a last step, we subtract 5.6% of the median light curve level to account for the companion contribution. We use the same rule for all bands, which is only an approximation because, as [Alonso et al. \(2008\)](#) point out, the companion has a later type (probably K or M) and, therefore, a different spectrum from CoRoT-2a.

3. Analysis

3.1. Transit profiles and stellar activity

A planet crossing the stellar disk imprints a characteristic transit feature on the light curve of the star (e.g., [Pont et al. 2007](#); [Wolter et al. 2009](#)). The exact profile is determined by planetary parameters as well as the structure of the stellar surface. A model that describes the transit profile must account for both. One of the key parameters of the surface model is the limb darkening law. The presence of limb darkening seriously complicates transit modeling, because it can considerably affect the transit profile, while it is difficult to recover its characteristics from light curve analyses (e.g., [Winn 2009](#)).

Stellar activity adds yet another dimension of complexity to the problem, because a (potentially evolving) surface brightness distribution also affects the transit profiles. The local brightness on the surface can either be decreased by dark spots or increased by bright faculae compared to the undisturbed photosphere. Spots (or faculae) located within the eclipsed section of the stellar surface lead to a decrease (increase) in the transit depth, and the true profile depends on the distribution of those structures across the planetary path. Spots and faculae located on the non-eclipsed section of the surface do not directly affect the

transit profile but change the overall level of the light curve. As transit light curves are, however, usually normalized with respect to the count rate level immediately before and after the transit, the non-eclipsed spot contribution enters (or can enter) the resulting curve as a time-dependent modulation of the normalized transit depth.

3.2. Transit light-curve normalization

As mentioned above, the normalization may affect the shape of the transit profiles. We now discuss two normalization approaches and compare their effect on the transit profiles. We define f_i to be the measured flux in time bin i , n_i an estimate of the count rate level without the transit (henceforth referred to as the “local continuum”), and p a measure of the unspotted photospheric level in the light curve, i.e., the count rate obtained in the respective band, when the star shows a purely photospheric surface. Usually, the quantity

$$y_i = f_i/n_i \quad (2)$$

is referred to as the “normalized flux”.

If we normalize the flux according to Eq. (2), we may produce variations in the transit light-curve depth in response to non-uniform surface flux distributions as encountered on active stars. To demonstrate this, we assume that a planet transits its host star twice. During the first transit, the stellar surface remains free of spots, but during the second transit there is a large active region on any part of the star not covered by the planetary disk (but visible). Consequently, the local continuum estimate, n_i , for the second transit is lower, and the normalized transit appears deeper, although it is exactly the same transit in absolute (non-normalized) numbers.

To overcome this shortcoming, we define the alternative normalization to be

$$z_i = \frac{f_i - n_i}{p} + 1. \quad (3)$$

In both cases, the transit light curve is normalized with respect to the local continuum either by division or subtraction. The conceptual difference lies in the treatment of the local continuum level and how it enters the normalized transit light curve. Using Eq. (3), the observed transit is shifted, normalized by a constant, and shifted again. While the scaling in this case remains the same for all transits, the scaling applied in Eq. (2) is a function of the local continuum.

Following the above example, we assume that the same transit can be normalized by using Eqs. (2) and (3). To evaluate the differences between the approaches, we consider the expression

$$\frac{z_i}{y_i} = \frac{(f_i - n_i)/p + 1}{f_i/n_i} \geq 1. \quad (4)$$

For $n_i = p$, Eq. (4) holds as a strict equality, i.e., both normalizations yield identical results. The inequality equates to true, if $p > n_i$ and $n_i > f_i$. The first condition reflects that the local continuum estimate should not exceed the photospheric light-curve level, and the second one says that the light-curve level is below the local continuum. The second condition is naturally fulfilled during a transit, and the first is also met as long as faculae do not dominate over the dark spots during the transit. In the case of CoRoT-2a, [Lanza et al. \(2009\)](#) find no evidence of a significant flux contribution due to faculae, so that we conclude that the normalized transit obtained using Eq. (3) is always shallower than that resulting from Eq. (2), unless $n_i = p$, in which case the outcomes are equal.

3.2.1. Quantifying the normalization induced difference in transit depth

We now study a single transit and consider data points covered by index set j , for which the term $n_j - f_j$ reaches a maximal value of T_0 at some index value $j = T$. At this position, the normalization obtained from Eq. (3) is given by $z_T = (f_T - n_T)/p + 1 = -T_0/p + 1$, whereas Eq. (2) yields $y_T = f_T/n_T = (n_T - T_0)/n_T$. These values are now used to compare the transit depths provided by the two normalizations. We note that we assume that the normalized depth is maximal at index T ; this is always true for Eq. (3), but not necessarily for Eq. (2), a point that we assume to be a minor issue. We again find that $z_T = y_T$ if $n_T = p$. If, however, the local continuum estimate is given by $n_T \approx \alpha p$ ($\alpha \leq 1$), the results differ by

$$z_T - y_T = T_0 p^{-1} (\alpha^{-1} - 1). \quad (5)$$

Using the extreme values observed for CoRoT-2a ($\alpha \approx 0.96$ and $T_0 \approx 0.03 \times p$), the right-hand side of Eq. (5) yields $\approx 1.3 \times 10^{-3}$ for the difference in transit depth, caused exclusively by applying two different normalization prescriptions.

3.2.2. Which normalization should be used?

For planetary research it is important to “clean” the transit light curves of stellar activity before deriving the “undisturbed” profile associated with the planet *only*. Since transit light curves normalized using Eq. (3) are all scaled using the same factor, they preserve their shape and depth (at least relative to each other) and can, therefore, be combined consistently, which is not necessarily the case when Eq. (2) is used. This does not mean that the obtained transit depth is necessarily the “true” depth, because Eq. (3) includes the photospheric brightness level, p , as a time-independent scaling factor. At least in the context of the light-curve analysis, p cannot be determined with certainty since the star may not show an undisturbed surface during the observation, which may actually never be shown.

A problem evident in CoRoT light-curve analyses is the existence of long-term instrumental gradients in the data (cf. Sect. 2). By modeling these trends with a “sliding” response, R_d , of the detector, so that the relation between “true” photometry, c_i , and observation, $c_{o,i}$, is given by $c_{o,i} = c_i \cdot R_{d,i}$, we find that Eq. (1) yields

$$c_{\text{corr},i} = c_i \cdot \left(R_{d,i} \frac{\bar{c}}{q_i} \right). \quad (6)$$

Obviously, the true photometry is recovered when the embraced term equates to one. However, the scaling of \bar{c} in Eq. (1) is arbitrary, so that this is not necessarily the case. As long as q_i , however, appropriately represents the shape of $R_{d,i}$, the term provides a global scaling, which cancels out in both of the Eqs. (2) and (3).

For our transit analysis, we argue in favor of the normalization along Eq. (3). We estimate the photospheric level from the highest count rate during the most prominent global maximum (at JD ≈ 2454373.3) in each individual band. These estimates are based on the reduced light curves; in particular, we have accounted for both the instrumental trend and the stellar companion. Throughout our analysis, we use the values $p_{\text{white}} = 703\,000$, $p_{\text{red}} = 489\,000$, $p_{\text{green}} = 88\,500$, and $p_{\text{blue}} = 124\,500$ (in units of $e^-/32s$). Since even at that time, spots are likely to have been present on the stellar disk, these estimates might represent lower limits to the true value of p .

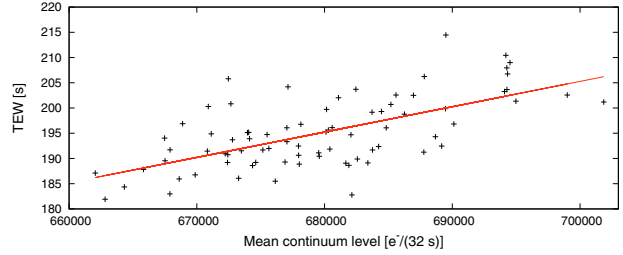


Fig. 1. Transit equivalent width (TEW) versus transit continuum level as well as the best-fit linear model.

3.3. Transit profiles in CoRoT-2a

The global light curve of CoRoT-2a shows pronounced maxima and minima and a temporally variable amplitude of the global modulation (Alonso et al. 2008). It is natural to expect the spot coverage on the eclipsed section of the stellar surface to be smallest where the global light curve is found at a high level, and transit events occurring during those phases should, thus, be least contaminated with the effects of stellar activity. The opposite should be true for transits during low light-curve levels.

To quantify the impact of activity on the transit profile, we define the transit equivalent width (TEW) of transit n

$$TEW_n = \int_{t_I}^{t_{IV}} (1 - z_n(t)) dt \approx \sum_i (1 - z_{n,i}) \delta t_i, \quad (7)$$

where t_I and t_{IV} must be chosen so that they enclose the entire transit. Extending the integration boundaries beyond the true extent of the transit does not change the expectation value of Eq. (7), but only introduces an extra amount of error. The nominal unit of the TEW is time.

3.3.1. The relation between transit equivalent width and global light-curve modulation

As outlined above, we expect activity to have greater impact when the overall light-curve level is low. When this is true, it should be reflected by a relation between the transit equivalent width and the transit continuum level (the overall light-curve level at transit time).

In Fig. 1, we show the distribution of TEWs as a function of the local continuum level for all 79 transits observed with a 32 s sampling. There is a clear tendency for larger TEWs to be associated with higher continuum levels, thus, providing obvious evidence of activity-shaped transit light curves. In the same figure, we also show the best-fit linear model relation, which has a gradient of $d(\text{TEW})/d(\text{CL}) = (5 \pm 1.5) \times 10^{-4} \text{ s}/(e^- 32 \text{ s})$.

To corroborate the reality of the above stated correlation, we calculated the correlation coefficient, R . Its value of $R = 0.642$ confirms the visual impression of a large scatter in the distribution of data points (cf., Fig. 1). We estimate the statistical error for a single data point to be $\approx 0.1\%$, so that the scatter cannot be explained by measurement errors. To check whether the continuum level and the TEW are independent variables, we employ a t-test and find the null hypothesis (independent quantities) to be rejected with an error probability of 1.8×10^{-10} , so that the correlation between the TEWs and the continuum level must be regarded as highly significant.

As a cross-check of the interpretation of this finding, we also investigated the distribution of TEWs against time, which shows no such linear relation ($R = 0.110$). Therefore, we argue that the

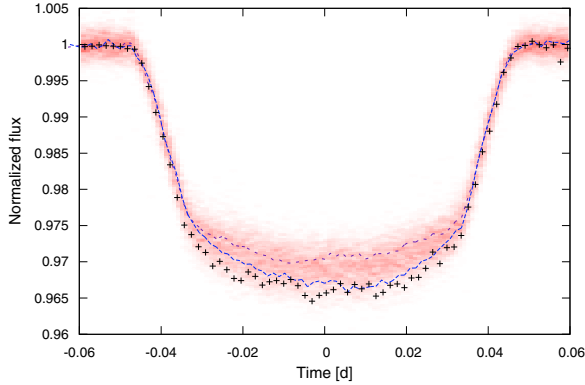


Fig. 2. Average transit light curves obtained by combining the ten profiles exhibiting the highest (thick dashes) and lowest (thin dashes) continuum levels. The crosses indicate our lower envelope estimate and the color gradient (red) illustrates the distribution of data points for all available transits.

effect is not instrumental or caused by our data reduction, but physical.

3.4. Comparing high and low continuum level transits

Since activity is evident in the profiles of the transit light curves, we further investigate its effect by comparing the most and least affected transit light curves. Therefore, we average the ten transits with the highest continuum levels (No. 3, 16, 42, 47, 50, 55, 68, 73, 76, and 81) and compare the result to an average of the ten transits with the lowest continuum level (No. 15, 23, 35, 40, 43, 69, 72, 75, 77, and 80). In Fig. 2, we show the two averages as well as our computed lower envelope (see Sect. 3.5) superimposed on the entire set of folded photometry data points. The distribution of the entire set is denoted by a color gradient (red) with stronger color indicating a stronger concentration of data points. The curve obtained from the transits at a “low continuum state” is clearly shallower, as was already indicated by the TEW distribution presented in Fig. 1.

The difference in TEW amounts to ≈ 15.5 s in this extreme case. We checked the significance of this number with a Monte Carlo approach. On the basis of 20 randomly chosen transits, we constructed two averaged light curves using 10 transits for each and calculated the difference in TEW. Among 1000 trials, we did not find a single pair with a difference beyond 12 s, so that the result is not likely to be caused by an accidental coincidence.

3.5. Obtaining a lower envelope to the transit profiles

As was demonstrated in the preceding section, activity shapes the transit light curves, and we cannot exclude that every transit is affected so that a priori no individual profile can be used as a template representing the “undisturbed” light curve. The distortion of the individual profiles is, however, not completely random, but the sign of the induced deviation is known as long as we assume that the dark structures dominate over bright faculae, which seems justified for CoRoT-2a (Lanza et al. 2009). In this case, activity always tends to raise the light-curve level and, thus, decreases the transit depth. Therefore, the most suitable model of the undisturbed profile can be estimated to be a lower envelope to the observed transit profiles.

We take a set of N_T transit observations and fold the associated photometry at a single transit interval, providing us with the set $LC_{T,i}$ of transit data points. If the lower envelope were already among the set of observed transits, it would in principle look like every other light curve. In particular, it shows the same amount of intrinsic scattering (not including activity), characterized by the variance σ_0^2 :

We estimate the variance to be

$$\sigma_0^2 \approx \frac{1}{N} \sum_j^N (LC_{T,j} - \mu_j)^2, \quad (8)$$

where μ_j is the (unknown) expectation value and N is the number of data points. The aim of the following effort is to identify the lowest conceivable curve sharing the same variance. To achieve this, we divide the transit span into a number of subintervals, each containing a subsample, s , of LC_T . The distribution of data points in s is now approximated by a “local model”, $lm(\gamma)$, with a free normalization γ ; lm can for instance be a constant or a gradient. Given lm , we adapt the normalization to solve the equation

$$\left(\frac{\sum_s (LC_s - lm(\gamma))^2 \cdot H(lm(\gamma) - LC_s)}{\sum_s H(lm(\gamma) - LC_s)} - \sigma_0^2 \right) = 0, \quad (9)$$

where H denotes the Heaviside function ($H(x) = 1$ for $x > 0$, and $H(x) = 0$ otherwise). In this way, we search for the local model compatible with the known variance of the lower envelope. The ratio on the left-hand side of Eq. (9) represents a variance estimator exclusively based on data points below the local model. It increases (strictly) monotonically except for the values of γ , where the local model “crosses” a data point and the denominator increases by one instantaneously. Therefore, there may be more than one solution to Eq. (9). From the mathematical point of view, all solutions are equivalent, but for a conservative estimate of the lower envelope the largest one should be used.

In Fig. 2, we show the lower envelope, which is in far closer agreement with the average of the high continuum transit profiles than with its low continuum counterpart. The derivation of the lower envelope is based on Eq. (9). To obtain an estimate of σ_0^2 , we fitted a 500 s long span within the transit flanks (3500 ± 250 s from the transit center), where activity has little effect, with a straight line and calculated the variance with respect to this model. The resulting value (using normalized flux) of $\sigma_0^2 = 1.6 \times 10^{-6}$ was adopted in the calculation. Furthermore, we chose a bin width of 150 s, and the “local model” was defined as a regression line within a ± 100 s time span around the bin center. Additionally, we postulated that at least 8 (out of ≈ 350) data points per bin should be located below the envelope, which improved the stability of the method to the effect of outliers but has otherwise little impact.

3.6. Transit profiles in different color channels

CoRoT observes in three different bands termed “red”, “green”, and “blue”. In the following, we present a qualitative analysis of the transit profiles in the separate bands. In the case of CoRoT-2a, approximately 70% of the flux is observed in the red band, and the remaining 30% is more or less equally distributed among the green and blue channels. To compare the profiles, we average all available transits in each band individually and normalize the results with respect to their TEW, i.e., after this step they all have the same TEW. The resulting profiles represent the curves that would be obtained if the stellar flux integrated along the planetary path was the same in all bands.

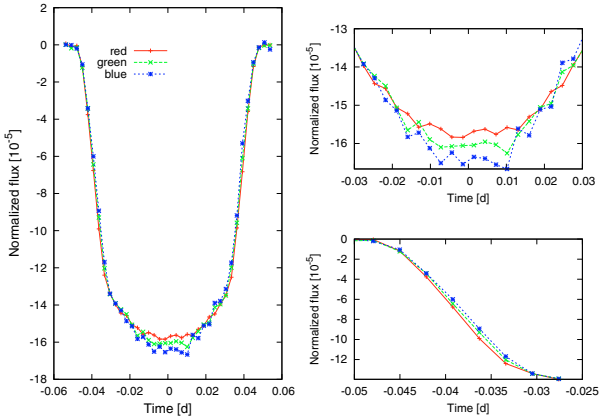


Fig. 3. *Left panel:* normalized transit in the three CoRoT bands red, green, and blue obtained by averaging all available data. *Upper right:* close-up of the transit center. *Lower right:* close-up of the ingress flank of the transit.

In Fig. 3, we show the transit light curves normalized in this way (TEW=1) obtained in the three bands.

The normalized transits show a difference in both their flank profile and their depth. The blue and green transit profiles are both narrower than the red one, and deeper at the center. This behavior is most pronounced in the blue band, so that the green transit light curve virtually always lies in-between the curves obtained in red and blue.

The behavior described above can be explained by a color-dependent limb darkening law, with stronger limb darkening at shorter wavelengths as predicted by atmospheric models (Claret 2004) and observed on the Sun (Pierce & Slaughter 1977). We checked that analytical transit models (Pál 2008) generated for a set of limb darkening coefficients, indeed, reproduce the observed behavior when normalized with respect to their TEW.

Normalizing the averaged transits not with respect to TEW but using Eq. (3) yields approximately the same depth in all bands, while the difference in the flanks becomes more pronounced. The reason for this could be an incorrect relative normalization, which can e.g., occur if the eclipsed section of the star is (on average) redder than the remainder of the surface because of pronounced activity or gravity darkening, or it may be a relic of an inappropriate treatment of the companion’s flux contribution. Whatever the explanation, it is clear from Fig. 3 that the flanks and centers in the individual bands cannot be reconciled simultaneously by a renormalization. Therefore, our analysis shows that the transit light curves are color dependent.

4. Stellar activity and planetary parameters

The preceding discussion shows that stellar activity has a considerable influence on the profile of the transit light curves, and the derivation of the planetary parameters will therefore also be affected. We now determine the radius and the orbit inclination of CoRoT-2b taking activity into account, and discuss the remaining uncertainties in the modeling.

4.1. Deriving the planetary radius and inclination from the lower envelope profile

In the analysis presented by Alonso et al. (2008), the fit to the planetary parameters is based on the average of 78 transit light

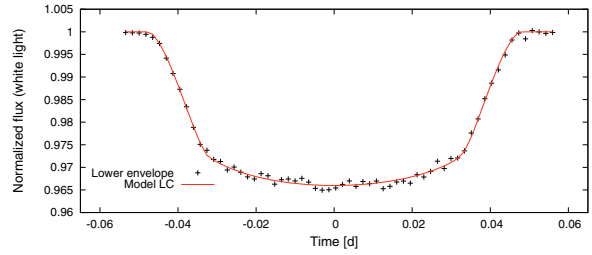


Fig. 4. Lower envelope of all normalized transit light curves (already shown in Fig. 2) and our model fit.

curves (see Table 1 for an excerpt of their results). While this yields a good approximation, the results still include a contribution of stellar activity, and an undisturbed transit is needed to calculate “clean” planetary parameters.

We follow a simplified approach to estimate the impact of activity on the planetary parameters. In particular, we use the lower envelope derived in Sect. 3.4 as the most suitable available model for the undisturbed transit. Starting from the results reported by Alonso et al. (2008), we reiterate the fit of the planetary parameters. In our approach, we fix the parameters of transit timing, i.e., the semi-major axis and stellar radius, and the limb darkening coefficients at the values given by Alonso et al. (2008) (cf. Table 1). The two free parameters are the planetary radius and its inclination.

We note that limb darkening coefficients recovered by light curve analyses are not reliable, especially when more than one coefficient is fitted (e.g., Winn 2009). However, since an accurate calibration of the CoRoT color bands is not yet available and the coefficients determined by Alonso et al. (2008) roughly correspond to numbers predicted by stellar atmosphere models¹, we decided to use the Alonso et al. values, which also simplifies the comparison of the results.

For the fit, we use the analytical models given by Pál (2008) in combination with a Nelder-Mead simplex algorithm (e.g., Press et al. 1992).

The result of our modeling is illustrated in Fig. 4. The most probable radius ratio is $R_p/R_s = 0.172 \pm 0.001$ at an inclination of $87.7^\circ \pm 0.2^\circ$. The quoted errors are statistical errors and only valid in the context of the model. These numbers should be compared with the values $R_p/R_s = 0.1667 \pm 0.0006$ and $87.84^\circ \pm 0.1^\circ$ (cf., Table 1) derived without taking activity effects into account. The best-fit model inclination is compatible with the value determined by Alonso et al. (2008), but “our” planet is larger by $\approx 3\%$. The planet’s size depends mainly on the transit depth, which is, indeed, affected at about this level by both normalization (Sect. 3.2.1) and stellar activity (Sect. 3.4).

Clearly, the derived change in R_p/R_s of 0.005 is much larger than the statistical error obtained from light-curve fitting, and, therefore, the neglect of activity leads to systematic errors in excess of statistical errors. While the overall effect in planet radius is $\approx 3\%$, the error in density becomes $\approx 10\%$. These errors are certainly tolerable for modeling planetary mass-radius relationships, but they are unacceptable for precision measurements of possible orbit changes in these systems.

¹ For $T_{\text{eff}} = 5600$ K and $\log(g) = 4.5$, the PHOENIX models given by Claret (2004) yield quadratic limb darkening coefficients of $u_a = 0.46$ and $u_b = 0.25$ in the Sloan- r' band.

4.1.1. Planetary parameters and photospheric level

As already indicated the normalization according to Eq. (3) relies on a “photospheric light-curve level”, p , which enters as a global scaling factor and, therefore, also impedes the constraint of the planet’s properties.

In a simple case, the star appears as a sphere with a purely photospheric surface, and the observed transit depth, f_0 , can be identified with the square of the ratio of the planetary to the stellar radius

$$f = \frac{\max(n_i - f_i)}{p} = \left(\frac{R_p}{R_*}\right)^2 L_d, \quad (10)$$

where L_d is a correction factor that accounts for limb darkening. However, when the observed star is active and the light curve is variable, there is no guarantee that the maximum point in the observed photometry is an appropriate representation of the photospheric stellar luminosity. Persistent inhomogeneities, such as polar spots and long-lived spot contributions, modulate the light curve, so that the pure photosphere might only be visible anytime the star is not observed or possibly never.

Assume our estimate, p_m , of the photospheric level underestimates the true value, p , by a factor of $0 < c \leq 1$ so that $p_m = p \cdot c$ and $f_{e,i}$ denotes the lower envelope transit light curve. The measured transit depth, f_m , then becomes

$$f_m = \frac{\max(n_i - f_{e,i})}{p_m} = \left(\frac{R_p}{R_*}\right)^2 \frac{L_d}{c}, \quad (11)$$

and another scaling factor must be applied to the radius ratio. While p_m is a measured quantity, c is unknown, and if we neglect it in the physical interpretation, i.e., the right-hand side of Eq. (11), the ratio of planetary to stellar radius will be overestimated by a factor of $1/\sqrt{c}$.

The value of c cannot be quantified in the context of this work; only an estimate can be provided. Doppler imaging studies have found that polar spots are common and persistent structures in young, active stars (e.g., Huber et al. 2009). Assuming that polar spots also exist on CoRoT-2a and that they reach to a latitude of 70° , they occupy roughly 2% of the visible stellar disk. Adopting a spot contrast of 50%, c becomes 0.99 in this case, and the planet size would be overestimated by 0.5%. Since the poles of CoRoT-2a are seen under a large viewing angle, their impact would, thus, be appreciably smaller than the amplitude of the global brightness modulation (ca. 4%). Nonetheless, in terms of sign, this effect counteracts the transit depth decrease caused by activity, and if the polar spots are larger or symmetric structures at lower latitudes contribute, it may even balance it.

5. Discussion and conclusion

Stellar activity is clearly seen in the CoRoT measured transit light curves of CoRoT-2a, and an appropriate normalization is necessary to derive the true transit light curve profile accurately.

The transit profiles observed in CoRoT-2a are affected by activity, as is obvious in many transits where active regions cause distinct “bumps” in the light curve (e.g., Wolter et al. 2009). Furthermore, our analysis indicates that not only profiles

with bumps but presumably all transit profiles are influenced by stellar activity. This is evident in the relationship between the transit equivalent width and the level of the global light curve: transits observed during periods where the star appears relatively bright are deeper than those observed during faint phases. We demonstrated that this correlation is extremely significant, but also that the data points show a large scatter around an assumed linear model relation. If the star were to modulate its surface brightness globally and homogeneously, this relation would be perfectly linear except for measurement errors. Therefore, we interpret the observed scatter as a consequence of surface evolution. When the global light curve is minimal, we also find more spots on the eclipsed portion of the surface, but only on average, and for an individual transit, this may not be the case. Thus, the surface configuration is clearly not the same for every minimum observed.

In addition, we demonstrated that the transit profiles exhibit a color dependence compatible with a color-dependent limb darkening law as expected from stellar atmospheric models and the analogy with the solar case.

All these influences can potentially interfere with the determination of the planetary parameters. Using our lower (white light) transit envelope, we determined new values for the planet-to-star radius ratio and the orbital inclination. While the latter remains compatible with previously reported results, the planet radius turns out to be larger (compared to the star) by about 3%. Although our approach takes into account many activity-related effects, a number of uncertainties remain. For example, the photospheric light curve level needed for transit normalization cannot be determined with certainty from our analysis and the same applies to the limb darkening law. We are therefore more certain than for the planetary parameters themselves, in our conclusion that the errors in their determination are much larger than the statistical ones.

While CoRoT-2a is certainly an extreme example of an active star, stellar activity is a common phenomenon especially on young stars. Therefore, in general, stellar activity cannot be neglected in planetary research, if the accuracy of the results should exceed the percent level.

Acknowledgements. S.C. and U.W. acknowledge DLR support (50OR0105). K.H. is a member of the DFG Graduiertenkolleg 1351 *Extrasolar Planets and their Host Stars*. S.S. acknowledges DLR support (50OR0703).

References

- Alonso, R., Auvergne, M., Baglin, A., et al. 2008, *A&A*, 482, L21
- Auvergne, M., Bodin, P., Boisnard, L., et al. 2009, *ArXiv e-prints*
- Bouchy, F., Queloz, D., Deleuil, M., et al. 2008, *A&A*, 482, L25
- Claret, A. 2004, *A&A*, 428, 1001
- Huber, K. F., Wolter, U., Czesla, S., et al. 2009, *A&A*, accepted
- Lanza, A. F., Pagano, I., Leto, G., et al. 2009, *A&A*, 493, 193
- Pál, A. 2008, *MNRAS*, 390, 281
- Pierce, A. K., & Slaughter, C. D. 1977, *Sol. Phys.*, 51, 25
- Pont, F., Gilliland, R. L., Moutou, C., et al. 2007, *A&A*, 476, 1347
- Press, W. H., Teukolsky, S. A., Vetterling, W. T., et al. 1992, *Numerical recipes in C. The art of scientific computing*, ed. W. H. Press, S. A. Teukolsky, W. T. Vetterling, & B. P. Flannery
- Winn, J. N. 2009, in *IAU Symposium*, 253, *IAU Symp.*, 99
- Wolter, U., Schmitt, J. H. M. M., Huber, K. F., et al. 2009, *A&A*, accepted

A&A 508, 901–907 (2009)
 DOI: 10.1051/0004-6361/200912867
 © ESO 2009

**Astronomy
&
Astrophysics**

A planetary eclipse map of CoRoT-2a

Comprehensive lightcurve modeling combining rotational-modulation and transits

K. F. Huber, S. Czesla, U. Wolter, and J. H. M. M. Schmitt

Hamburger Sternwarte, Universität Hamburg, Gojenbergsweg 112, 21029 Hamburg, Germany
 e-mail: khuber@hs.uni-hamburg.de

Received 10 July 2009 / Accepted 12 September 2009

ABSTRACT

We analyze the surface structure of the planet host star CoRoT-2a using a consistent model for both the “global” (i.e., rotationally modulated) lightcurve and the transit lightcurves, using data provided by the CoRoT mission. After selecting a time interval covering two stellar rotations and six transits of the planetary companion CoRoT-2b, we have adopted a “strip” model of the surface to reproduce the photometric modulation inside and outside the transits simultaneously. Our reconstructions show that it is possible to achieve appropriate fits for the entire subinterval using a low-resolution surface model with 36 strips. The surface reconstructions indicate that the brightness on the eclipsed section of the stellar surface is $(6 \pm 1)\%$ lower than the average brightness of the remaining surface. This result suggests a concentration of stellar activity in a band around the stellar equator similar to the behavior observed on the Sun.

Key words. techniques: photometric – stars: activity – planetary systems – starspots – stars: individual: CoRoT-2a

1. Introduction

Astronomers have long been interested in the surface structure of active stars and their evolution; yet, the surfaces of stars other than the Sun can hardly be resolved directly, so that indirect techniques must be used to obtain an image of the surface. One such technique is Doppler imaging (Vogt & Penrod 1983), which requires a dense series of high-resolution spectra and stellar rotation velocities of $v \sin(i) \gtrsim 20 \text{ km s}^{-1}$ (compared to $v_{\text{eq}} \approx 2 \text{ km s}^{-1}$ for the Sun). Alternatively, lightcurves also yield information on stellar surface structures and can usually be obtained at low observational cost. However, photometry provides less information and the problem of lightcurve inversion is known to be notoriously ill-posed.

Since the launch of CoRoT in 2006, an increasing amount of high-quality space-based photometry has become available. Without the limitations the atmosphere and the day-night cycle impose on ground-based observatories, CoRoT is able to provide photometry with unprecedented temporal coverage and cadence, which is enormously interesting in the context of stellar activity and surface reconstruction.

In the course of the CoRoT planet-hunting project, the giant planet CoRoT-2b (Alonso et al. 2008) was detected. The host star of this planet, CoRoT-2a, is solar-like in mass and radius, but rotates approximately four times faster than the Sun and is considerably more active. The planet orbits its host star approximately three times per stellar rotation and, during its passage across the stellar disk, acts as a shutter scanning the surface of the star along a well-defined latitudinal band. Because the “local” surface structure is imprinted on the transit profiles (Wolter et al. 2009; Czesla et al. 2009), they can be used to partially resolve the ambiguity of the lightcurve inversion problem.

While Lanza et al. (2009) used the “global” lightcurve of the host star to reconstruct its surface inhomogeneities, without

considering the transits, Wolter et al. (2009) concentrated on a single transit lightcurve to reconstruct a fraction of the surface, neglecting the “global” lightcurve. In this work, we combine and refine these approaches to present a reconstruction that simultaneously describes both the overall lightcurve and the transits during two stellar rotations.

2. Observations and data reduction

Alonso et al. (2008) discovered the planet CoRoT-2b using photometric data provided by the CoRoT mission (for a detailed description, see Auvergne et al. 2009). The planet was detected in the field observed during the first *long run* carried out between May 16 and Oct. 15, 2007. The default sampling rate of CoRoT photometry is $1/512 \text{ s}^{-1}$. The CoRoT-2 lightcurve was observed at this rate only for the first five days, after which the transits were detected and the satellite switched to alarm mode, continuing to take data every 32 s. The light collected by the CoRoT telescope is dispersed using a prism and recorded by a CCD chip. Individual sources are separated by a photometric mask, which also defines three broadband channels (nominally red, green, and blue). Currently, there is no appropriate calibration available for these channels, so that it is unfeasible to use the color information in this work. The signal obtained by summing up the individual channels, often referred to as “white light”, corresponds to an optical measurement with a filter transmission maximum in the red wavelength region (Auvergne et al. 2009). Accordingly, Lanza et al. (2009) assume an isophotal wavelength of 700 nm for their passband. The CoRoT data undergo a standard pipeline processing, during which data points are flagged that are significantly affected by known events, as for example the South Atlantic Anomaly (SAA), so that they can be removed from the lightcurve.

Table 1. Stellar/planetary parameters of CoRoT-2a/b.

Star ^a	Value ± Error	Ref. ^b
P_s	(4.522 ± 0.024) d	L09
P_s^*	4.57 d	
Spectral type	G7V	B08
Planet ^c	Value ± Error	Ref.
P_p	(1.7429964 ± 0.0000017) d	A08
T_c [BJD]	(2 454 237.53362 ± 0.00014) d	A08
i	(87.7 ± 0.2)°	C09
R_p/R_s	(0.172 ± 0.001)	C09
a/R_s	(6.70 ± 0.03)	A08
u_a, u_b	(0.41 ± 0.03), (0.06 ± 0.03)	A08

^a P_s – stellar rotation period, P_s^* – stellar rotation period used for the observation interval analyzed in this paper (see Sect. 3.4). ^b Taken from Lanza et al. (2009) [L09], Alonso et al. (2008) [A08], Bouchy et al. (2008) [B08], or Czesla et al. (2009) [C09]. ^c P_p – orbital period, T_c – central time of first transit, i – orbital inclination, R_p, R_s – planetary and stellar radii, a – semi major axis of planetary orbit, u_a, u_b – linear and quadratic limb darkening coefficients.

The host star CoRoT-2 has a spectral type of G7V with an optical companion at a distance of approximately 4.3'' (2MASS, Skrutskie et al. 2006), too close to be resolved by CoRoT. According to Alonso et al. (2008) the secondary contributes a constant fraction of (5.6 ± 0.3)% to the total CoRoT-measured flux. In Table 1 we list the system parameters of CoRoT-2a/b, which are used throughout our analysis. CoRoT-2b’s orbital period of ≈1.74 days is about a third of CoRoT-2a’s rotation period; hence, the almost continuous CoRoT data sample of 142 days covers about 30 stellar rotations and more than 80 transits. The lightcurve shows signatures of strong stellar activity and substantial rotational modulation (Lanza et al. 2009). We use the same CoRoT raw data reduction procedures as described in Czesla et al. (2009, Sect. 2).

3. Analysis

3.1. Modeling approach

The measurements of the Rossiter-McLaughlin effect by Bouchy et al. (2008) suggest that the rotation axis of the host star and the planet’s orbit normal are approximately co-aligned ($\lambda = 7.4 \pm 4.5^\circ$). The sign λ represents the misalignment angle projected on the plane of the sky, and its value strongly favors aligned orbital and rotational axes, even though it does not prove it. More support for a co-aligned geometry comes from the following argument. Comparing the measured $v \sin(i) = 11.85 \text{ km s}^{-1}$ with a calculated equatorial velocity of $v_{\text{eq}} = 2\pi R_s/P_s \approx 10 \text{ km s}^{-1}$ derived with the theoretically obtained value $R_s = 0.9 \cdot R_\odot$ (Alonso et al. 2008) also favors $\sin(i) \approx 1$.

As a result, the planet always eclipses the same low-latitude band between 6 and 26 degrees. The transits separate the stellar surface into two observationally distinct regions, i.e., a region eclipsed by CoRoT-2b and another region that is not. In the case of CoRoT-2a, the eclipsed section covers ≈21% of the stellar disk corresponding to ≈17.3% of its surface. The time-resolved planet migration across the visible stellar disk sequentially covers and uncovers surface fractions, so that the brightness profile of the underlying stellar surface is imprinted on the transit lightcurve.

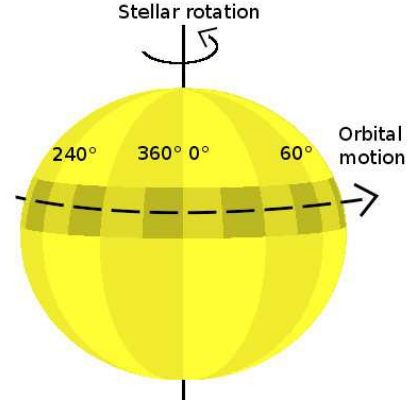


Fig. 1. Our model geometry using 12 longitudinal strips for the noneclipsed and 24 strips for the eclipsed section, respectively.

For our modeling, we separate the surface into the eclipsed and the noneclipsed section, which are both further subdivided into equally sized, longitudinal bins or “strips” as demonstrated in Fig. 1. Let N_e be the number of bins in the eclipsed section and N_n be the number of noneclipsed strips. As is apparent from Fig. 1, N_e and N_n need not be the same. Altogether, we have $N_{\text{tot}} = N_e + N_n$ bins enumerated by some index j . A brightness b_j is assigned to each of these surface bins, with which it contributes to the total (surface) flux of the star. Then let V_{ji} denote the visibility of the j th bin at time t_i . The visibility is modified in response to both a change in the viewing geometry caused by the stellar rotation and a transit of the planet. The modeled flux $f_{\text{mod},i}$ at time t_i is then given by the expression

$$f_{\text{mod},i} = \sum_{j=1}^{N_{\text{tot}}} V_{ji} b_j. \quad (1)$$

We determine the unknown brightnesses, b_j , by comparing $f_{\text{mod},i}$ to a set of M_C CoRoT flux measurements using a specifically weighted version of the χ^2 -statistics:

$$\chi_m^2 = \sum_{i=1}^{M_C} \frac{(f_{\text{mod},i} - f_{\text{obs},i})^2}{\sigma_i^2} \cdot w_i, \quad (2)$$

where χ_m^2 differs from χ^2 by a weighting factor, w_i , which we choose to be 10 for lightcurve points in transits and 1 otherwise. In this way, the global lightcurve and the transits are given about the same priority in the minimization process. Error bars for the individual photometric measurements were estimated from the datapoint distribution in the lightcurve, and the same value of $\sigma = 1000 \text{ e}^-/32 \text{ s} (= 1.4 \times 10^{-3}$ after lightcurve normalization) was used for all points.

In our modeling we currently exclude surface structures with a limb-angle dependent contrast. This particularly refers to solar-like faculae, for which Lanza et al. (2009) find no evidence in their analysis. The planet CoRoT-2b is modeled as a dark sphere without any thermal or reflected emission. This approximation is justified by the findings of Alonso et al. (2009), who report a detection of the secondary transit with a depth of (0.006 ± 0.002)%, which is negligible in our analysis.

The actual fit is carried out using a (nongradient) Nelder-Mead simplex algorithm (e.g. Press et al. 1992). All strips are mutually independent, and as we define only a rather

coarse strip subdivision for the noneclipsed section of the surface and since the eclipsed section is thoroughly covered by the transits, no further regularization is necessary.

3.2. Fit parameter space – parametrization, restrictions, and interpretation

Our fit space has a total of $N_{\text{tot}} = N_e + N_n$ dimensions, and the associated parameters are the brightnesses, $b_{j=1\dots N_{\text{tot}}}$. The most obvious choice of fit parameters are the brightnesses themselves. Nevertheless, using a slightly different definition in our algorithm provides some advantages. Instead of using the brightness of the global strips in our fits, we replace them with a weighted sum of the brightnesses of the eclipsed and the noneclipsed strips covering the same longitudes. This quantity z is a measure of the total flux emitted from all strips enclosed within a certain longitude range and, therefore, represents the level of the global lightcurve independent of how the brightness is distributed among the individual strips contributing to the sum. Without any transit observations, the distribution of flux among the individual contributors could hardly be restricted further, because latitudinal information could not be recovered. Thus, we use the tuple $(b_{l=1\dots N_e}, z_{k=1\dots N_n})$ for our reconstructions, where z is defined by

$$z_k = b_{N_e+k} + \frac{1}{c \cdot q} \sum_{s=q_0}^{s<q_0+q} b_s. \quad (3)$$

In Eq. (3), b_{N_e+k} denotes the brightness of the k th global strip, q is defined by N_e/N_n (the factor by which the eclipsed section is oversampled compared to the noneclipsed section), the index range $q_0 \leq s < q_0 + q$ enumerates all eclipsed strips covering the same longitudes as the global strip referred to by b_{N_e+k} , and c is a scaling factor accounting for the size difference between the eclipsed and the noneclipsed sections.

The practical advantage of using z instead of the brightness values themselves lies in the parameter interdependence. If we assume a fit algorithm adjusts the structure of a transit lightcurve using the eclipsed strips, every modification of their brightness causes a modification of the global lightcurve level, which might possibly be compensated by an appropriate adjustment of the global strip's brightness. Such an adjustment is inherent in the definition of z , so that $b_{l=1\dots N_e}$ and $z_{k=1\dots N_n}$ become largely independent quantities. In our fits we use $c = 5$, which roughly corresponds to the ratio of disk area covered by global and eclipsed strips.

To normalize the observed CoRoT-2a lightcurve, we divided all measurements by the highest flux value in our lightcurve so that $0 < (\text{normalized flux}) \leq 1$. The matrix V_{ji} in Eq. (1) is normalized according to

$$\sum_{j=1}^{N_{\text{tot}}} V_{ji} = 1 \text{ for all } i,$$

which yields $f_{\text{mod},i} = 1$ for $b_j = 1$, i.e., a constant model lightcurve at level 1. In a first, tentative interpretation, a surface element with the brightness 1 corresponds to a photospheric element free of any spots. Nonetheless, this is only correct as long as we assume that the largest observed flux in the lightcurve indeed represents the “spot-cleaned” photospheric luminosity. As CoRoT-2a is, however, a very active star, it seems probable that polar spots persist on its surface. Moreover, it seems likely that lower latitude structures cover a fraction of the stellar surface

even if the lightcurve is at maximum. For this reason, individual surface elements (strips) may be brighter than the “average surface” during the maximum observed flux. While such information could not be recovered if no transits were observed, individual surface regions eclipsed by the planet can conceivably be brighter than the “global” photosphere seen during lightcurve maximum. Therefore, we do not exclude strips with brightness values above 1 in our fits; i.e., we do not fix the photospheric brightness. This results in brightnesses above 1 for individual strips (e.g. Fig. 5). The only parameter space restriction applied during our fits is that the brightness must be positive.

3.3. Which part of the lightcurve should be used?

To derive a meaningful model, we need to select a time span, which is both long enough to provide an appropriate coverage of the surface, and short enough to minimize the effects of surface evolution. The latter, while doubtlessly present, appears slow compared to the stellar rotation period. Lanza et al. (2009) give typical lifetimes of 55 d (≈ 12 rotations) for active regions and 20–30 d for some individual spots. In our analysis, we use the time span ranging from phase 1.85 through 3.85 (BJD = 2 454 245.988 to BJD = 2 454 255.128, BJD = Barycentric Julian Date), which covers 6 transits and shows only small variations in the global lightcurve. The data are re-binned using a bin size of 128 s for the transit covered periods and 2016 s for the remaining lightcurve.

Our binning approach has to take into account interruptions of the lightcurve due to data drop outs (for instance caused by the South Atlantic Anomaly) and, of course, has to account for the change in bin size when a transit period begins or ends. Moreover, the CoRoT-2 lightcurve is sampled at two different rates ($1/512 \text{ s}^{-1}$ and $1/32 \text{ s}^{-1}$), which does not, however, cause any problem during the time span under consideration here. To obtain the binned curve, we averaged all flux values comprised of a bin and place the resulting value at the barycenter of the contributing time stamps. To compute the error, we divided the standard deviation for individual points by the square root of the number of averaged points. With this approach we (typically) obtain an error of 7×10^{-4} for in-transit points and 1.8×10^{-4} for out-of-transit points.

In Fig. 2 we demonstrate the coverage of the eclipsed surface section by these 6 transits within the selected phase interval. A single rotation phase including three transits only provides a very inhomogeneous “scan” of the eclipsed surface because of limb darkening, projection geometry, and the distribution of transit intervals (cf. Fig. 2). As a transit occurs every ≈ 0.4 stellar rotations, a homogeneous coverage of one full rotation is achieved using five transits. Nonetheless, we decided to use an integer number of stellar rotations and used six transits with the last one showing virtually the same part of the eclipsed surface as the first.

3.4. Surface evolution, rotation period, and model limits

Although the lightcurve of CoRoT-2a shows remarkably periodic minima and maxima, the rotation period of the star is not known exactly. Using a Lomb-Scargle periodogram, Lanza et al. (2009) find a rotation period of (4.52 ± 0.14) d for the star, which is further refined in the course of their surface modeling. Assuming that the longitudinal migration of the active longitudes should be minimal, Lanza et al. pin down the stellar rotation period to 4.5221 d. While this rotation period minimizes the

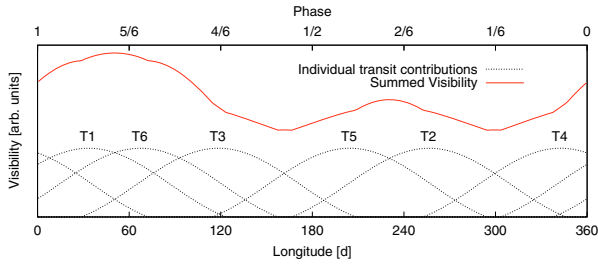


Fig. 2. Visibility of the eclipsed stellar surface during the transits in the selected observation interval. Low visibility means that a stellar feature at the corresponding longitude has a low impact on the transit profiles.

migration of the active longitudes, it results in individual spots showing a retrograde migration with an apparent angular velocity $\approx 1.3\%$ lower than the stellar rotation.

For our modeling we determine an “effective” period, representing the rotation period of the dominating surface features we are mainly interested in. We use the selected part of the lightcurve, remove the transits, and fold the remaining lightcurve back at a number of periods between 4.4 d and 4.7 d. The best match is obtained using a period of 4.57 d, which also results in the best fits of our models, so we use it throughout our analysis. This period also agrees with the values given by Lanza et al. (2009) assuming a rotation period of 4.5221 d and a mean retrograde migration “slowing down” the spots by 1.06%; however, changes in the rotation period on this scale do not result in significantly different surface reconstructions.

Even though we identified a lightcurve interval with relatively weak surface evolution, and refined the rotation period to account for some evolutionary effects, there is still a remaining modulation. This modulation imposes a fundamental limit on the fit quality that can be achieved by adopting a static model to the lightcurve, because both stellar rotations have to be described by the same model. To estimate this limit, again for the global lightcurve alone, we estimated the quantity

$$\langle \Delta \chi^2 \rangle = \frac{1}{N} \sum_{i=1}^N \left(\frac{f(p_i) - f(p_i + 1.0)}{2\sigma} \right)^2 \approx 14.2. \quad (4)$$

Here, $f(p_i)$ is the normalized flux in the i th phase bin, $f(p_i + 1.0)$ is the flux measured at the same phase during the next stellar rotation, and the sum stretches over all phases pertaining to the first rotation. The flux $f(p_i + 1.0)$ was obtained by interpolation, because the phase sampling is not exactly the same in both rotations. Since $\sigma_i \approx \sigma$, the best conceivable common model with respect to χ^2 at phase point p_i is given by $(f(p_i) + f(p_i + 1.0))/2$, so that the sum in Eq. (4) estimates the χ^2 contributions induced by surface evolution for each point. If there was no surface evolution, the expression in Eq. (4) would equate to 0.5, because statistical errors are, of course, still present. Therefore, a limit of $\chi^2 \approx 14.2$ per (global) lightcurve point will not be overcome by any static model. Equivalently, the expectation value, $\langle \Delta f/2 \rangle$, for the flux deviation from the best model equals $\langle \Delta f/2 \rangle = \langle (f(p_i) - f(p_i + 1.0))/2 \rangle = 5.6 \times 10^{-4}$ and cannot be surpassed.

3.5. Model resolution

The parameters N_e and N_n specify the model resolution of the eclipsed and noneclipsed sections. An appropriate choice of

these parameters balances fit quality and model ambiguity; this way the largest possible amount of information can be extracted.

To find the optimal value for the number of noneclipsed strips, we carry out fits to only the global lightcurve using an increasing number of global strips. Starting with only 4 strips, we find the reduced χ^2 value, χ_R^2 , to decrease rapidly until 8 strips are used. From this point, χ_R^2 only responds weakly to an increase in the strip number, but still decreases. Using 12 strips, we find $\chi_R^2 = 16$. With an estimated “socket” contribution of ≈ 14.4 provided by surface evolution, we attribute a fraction of $\chi_R^2 \approx 1.6$ to statistical noise. This fraction decreases to ≈ 1 if we use 30 strips, in which case we obtain a longitudinal resolution of 12° , comparable to what is achieved by Lanza et al. (2009). According to our test runs, we obtain reasonably stable results using 12 strips. As the stability of the solutions decreases for larger strip numbers, while χ_R^2 only slightly improves, we argue in favor of using 12 global strips in our modeling, to extract the largest possible amount of physically relevant results.

The resolution used on the eclipsed surface band is determined according to the following considerations. The extent of the planetary disk at the center of the stellar disk is about $20^\circ \times 20^\circ$. All stellar surface elements simultaneously (un)covered by the planet’s disk are equivalent in our lightcurve modeling. Individual features can, thus, be located (or smeared out) along the edge of the planetary disk to provide the same effect in the lightcurve. This edge stretches across 10° in longitude (only the “forward” part) and 20° in latitude, which defines a fundamental limit for the resolution. Assuming a particular shape for the features, decreases the degree of ambiguity as was for example shown by Wolter et al. (2009).

A meaningful structure in the transit profile should comprise at least 3 consecutive lightcurve bins corresponding to about 360 s or $\approx 6^\circ$ of planet movement across the center of the stellar disk. The extent of individual strips should, therefore, not fall below this limit, but be even larger.

Combining these arguments with the results of our test runs, we decided to use 24 strips on the eclipsed section, so that a longitudinal resolution of 15° is achieved. With this choice, a single strip on the eclipsed band appears about the same size (face-on) as the planetary disk. Additionally, we note that this approximately corresponds to the resolution used by Lanza et al. (2009) in their maximum entropy reconstructions.

3.6. Results of the modeling

In our analysis, we achieve a longitudinal resolution of $\approx 15^\circ$ on the eclipsed section making up $\approx 17\%$ of the stellar surface and 30° for the rest.

In Figs. 3 and 4 we present the results of our modeling. Figure 3 shows the entire subsample of CoRoT data points used in our modeling, along with our lightcurve model in the upper panel. In the lower panel we show the model residuals (see Sect. 3 for the definition of the error). Obviously, the data are matched well; however, there are systematic offsets between the observation and the model. In particular, the model tends to overestimate the observations during the first half of the time span, whereas it underpredicts it in the second half. This effect is related to surface evolution already detectable on timescales below the rotation period (Lanza et al. 2009, also see Sect. 3.4). Within the transits the residuals remain small compared to the rest of the lightcurve. This must be regarded a consequence of both the smaller bin size of 128 s used here and the twice better resolution of the model on the eclipsed section. During the fit the

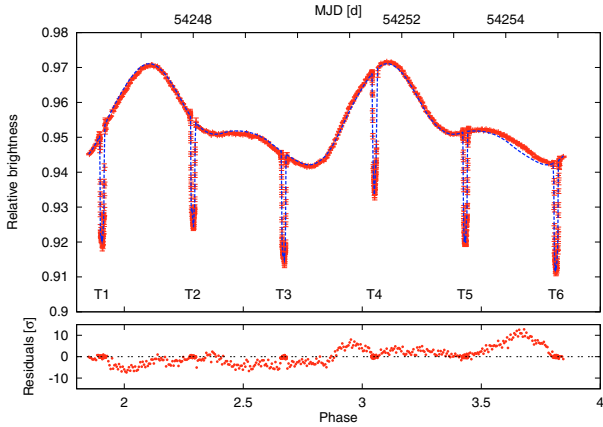


Fig. 3. *Upper panel:* CoRoT data for rotational phases 1.85 to 3.85 (2016 s binning for the global lightcurve and 128 s for the transits, red symbols) and our model lightcurve (dashed blue curve). *Lower panel:* residuals of our model.

transit residuals are “overweighted” by a factor of ten to avoid them to be prevailed by the much larger global residuals. Although, the deviations can be as large as 10σ , the mean deviation of the global lightcurve from the model amounts to 620×10^{-6} not far from the theoretical limit of 560×10^{-6} (cf. Sect. 3.4).

The lightcurve presented in Fig. 3 contains six transits (labeled “T1 – 6”). The associated transit lightcurves are shown in detail with our models in Fig. 4. Each individual panel shows the same transit twice: the lower curve represents a transit reconstruction from the full data sample (phases 1.85–3.85), and the upper curve denotes a reconstruction from only the first (T1–3) or second (T4–6) half of the sample data (shifted up by 0.03). The dotted lines show the transits as we would observe them without any activity on the eclipsed section of the surface, where we assume a brightness of 1 for the underlying photosphere.

The transit reconstructions obtained from half of the sample data reproduce the transit substructure very accurately. The resulting surface reconstructions are, however, unreliable where the surface is insufficiently covered (cf. Fig. 2, around longitudes of 180° and 320°). Interestingly, those reconstructions based on data from two rotation phases also recover most of the transit substructure and are by no means off the mark. When both rotation periods are used, χ^2 typically increases by 10–20%, a difference hardly visible in Fig. 4. As an exception, the fit quality of the third transit (T3) decreases dramatically, with χ^2 increasing by a factor of ≈ 2.5 . This is, however, mainly a consequence of the observed surface evolution shifting the continuum level. The overall stability of the fit quality indicates that lifetimes of surface features are a few stellar rotations, which agrees with the results of Lanza et al. (2009).

In Fig. 5 (lower and middle panels) we present the strip brightness distribution pertaining to the lightcurve model shown in Figs. 3 and 4, i.e., a 1D-reconstruction of the surface. We estimated mean and errors by recording the distribution of the parameter values obtained from 50 reconstructions with randomized starting points, and the respective distributions are indicated by the color gradients in Fig. 5. The error bars correspond to the associated standard deviations. They reflect the ability of the fitting algorithm to converge to a unique extremum, which is determined by both the characteristics of the algorithm and the structure of the fit statistics. Investigating the brightness

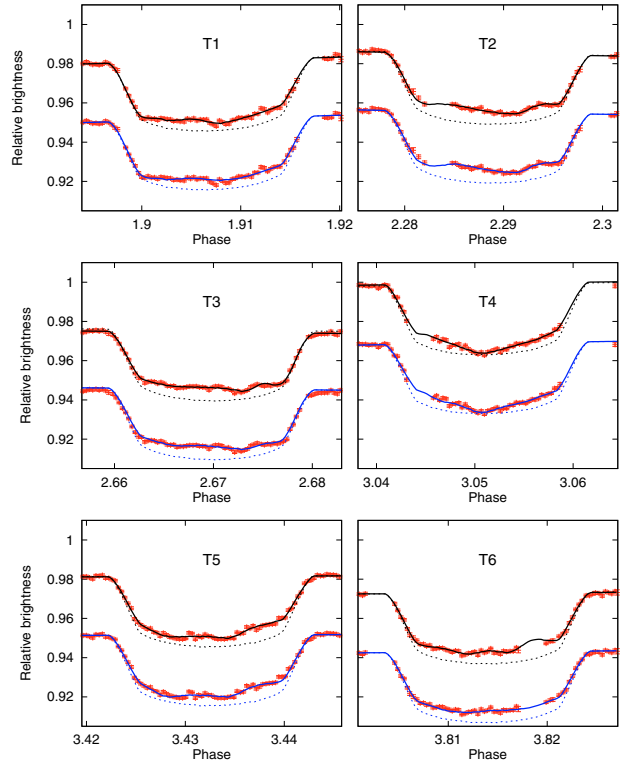


Fig. 4. Close-up of the six individual transits (128 s binning). Observations are drawn as red points (including 1σ errors). The upper curve (black) in each panel shows the fit obtained from 1 rotation (phases 1.85 to 2.85 for T1–3 and 2.85 to 3.85 for T4–6); the lower curve (blue) gives the fit obtained by modeling both rotations (as seen in Fig. 3). The dashed lines show the undisturbed transit profile for comparison.

distribution of the noneclipsed strips, we notice a slight degeneracy in some of the 12 noneclipsed strips; i.e., a fraction of the brightness may be redistributed without considerable loss of fit quality. The averaging of the 50 reconstructions flattens out such features, thus acting like a regularization of the brightness distribution. No such effect is observed for the eclipsed strips.

We compared our results to the reconstructions given by Lanza et al. (2009, their Fig. 4) and find our longitude scale to be shifted by $\approx 70^\circ$ with respect to the Lanza et al. scale. Our reconstructions show the same bright band at a longitude of $\approx 260^\circ$ (330° in our work). Tentatively averaging over an appropriate “time band” in their Fig. 4, we also find qualitative agreement for the remaining spot distribution.

Clearly, the flux fraction contributed by the eclipsed strips is less than that of the noneclipsed strips, because the area they cover is smaller by a factor of five. In the upper panel of Fig. 5 we show the lightcurve model contributions provided by the eclipsed and the noneclipsed section with their sum making up the model for the CoRoT data, which is also shown. The median flux level was subtracted from all curves to emphasize the modulation amplitude in favor of flux level. Obviously, the modulation amplitudes induced by the eclipsed and noneclipsed section balance approximately. This indicates that their influence on the stellar variability is about the same despite their large difference in size.

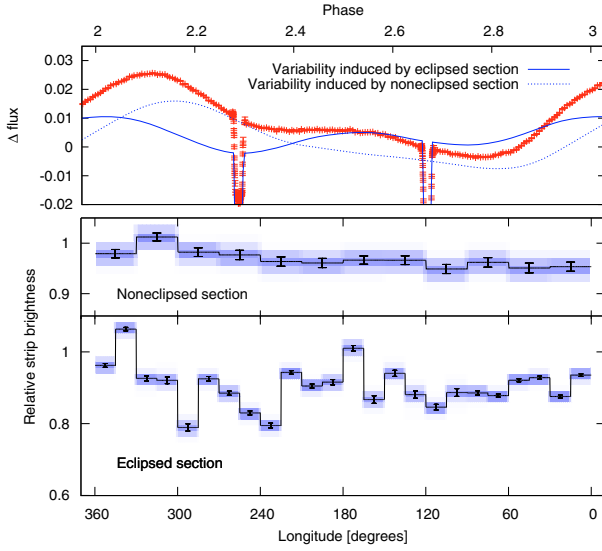


Fig. 5. *Upper panel:* the CoRoT data (red symbols) and the flux modulation contributed in our model by the eclipsed (blue curve) and noneclipsed section (dotted gray curve) individually. All curves are median-subtracted. *Middle and lower panels:* Brightness distribution of the strips located on the eclipsed and noneclipsed sections of the surface. The color gradient renders the distribution obtained from 50 reconstructions with randomized starting points.

A visualization of our best-fit surface reconstruction is presented in Fig. 6, showing a Hammer projection of the associated distribution of surface brightnesses. The planet-defined low-latitude band shows especially dark features, e.g. in the range of 200° to 300° in longitude, and is clearly visible. Also the noneclipsed sections of the star show significant variations. Note that our map only shows the average brightness of these regions; since the noneclipsed regions are larger by area, they contribute more flux; however, the “missing” flux in these regions is likely to also be concentrated in spots. In the following section we address the issue of the flux contribution from the eclipsed and noneclipsed sections.

3.6.1. Brightness distribution and spot coverage

Without a very precise absolute flux calibration (as e.g. in Jeffers et al. 2006), lightcurve analyses can usually only investigate the inhomogeneous part of the entire spot coverage. This statement is, however, partially invalidated by a transiting planet because it breaks the symmetry of the problem. Spots eclipsed by the planetary disk distort the transit profiles regardless of whether they belong to a structure that appears symmetric on a global scale or not.

As an example, assume that half the eclipsed section of CoRoT-2a, say longitudes 0° – 180° , is spotted, while the other half is covered by an undisturbed photosphere. Clearly, the transits will be shallower when the planet eclipses the dark portion of the star, and they will be deeper when the bright section is eclipsed. Also, the lightcurve will be distorted. Assume as well that a comparable section between longitudes 180° – 360° is dark on the opposite hemisphere of the star outside the eclipsed band. In this case the global spot configuration is perfectly symmetric with respect to longitude and the global lightcurve does not show any trace of activity. Nevertheless, the transits will still be

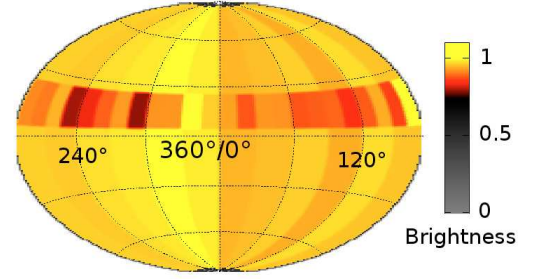


Fig. 6. Surface map of CoRoT-2a showing the reconstructed brightness distribution. Spots located on the noneclipsed surface are blurred over the entire reconstruction strip because of their unknown latitude resulting in the lower contrast compared to the eclipsed section.

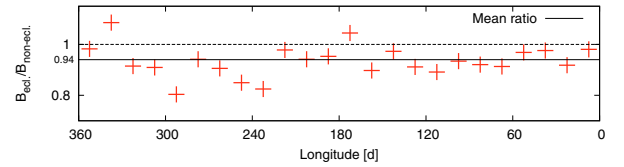


Fig. 7. Ratio of the surface brightness in the eclipsed ($B_{\text{ecl.}}$) and noneclipsed ($B_{\text{non-ecl.}}$) sections.

shallower when the planet eclipses the dark band, and they will still be deeper when the bright surface is eclipsed.

If the spots were distributed symmetrically across the stellar surface, we would expect the stellar surface to be homogeneously bright. In Fig. 7 we show the brightness ratio of eclipsed and noneclipsed sections as a function of longitude. Since there are more eclipsed than noneclipsed strips, we always compare strips covering the same longitude. Only in two cases is the eclipsed section brighter than its noneclipsed counterpart, while in 22 cases it is not.

The mean ratio is 0.94 ± 0.01 so that the part of the star passingly covered by the planet is found to be 6% darker than the rest of the surface. The remaining (nontransited) surface is brighter *on average*, but locally it may even be darker.

4. Discussion and conclusions

We present a surface reconstruction for the planet host star CoRoT-2a. Our modeling is based on a CoRoT data interval covering two full stellar rotations, and it treats the entire lightcurve – including the planetary transits – in a consistent way.

We show that a consistent modeling of the lightcurve is possible using a static model, i.e., not including any spot evolution. Although surface evolution on scales of the stellar rotation period is seen in both the reconstruction of the global lightcurve (as already reported by Lanza et al. 2009) and the transit lightcurves, this effect is weak in the context of our analysis. The static model provides reasonable fits to six consecutive transit lightcurves. The associated surface configuration changes little during this period, so the surface evolution must be relatively slow compared to the timescale of ≈ 9 d under consideration. This timescale is also valid for the lifetimes of spots on the eclipsed surface section.

Our results indicate that the planet-eclipsed band on the stellar surface is – on average – about 6% darker than the remaining part of the surface. Lanza et al. (2009) note that the strength

of differential rotation derived from their lightcurve fits seems much lower than the expected values derived from measurements in other systems (Barnes et al. 2005). They speculate that this may indicate a spot distribution limited to a narrow latitude band. If this is true, the latitude band is possibly located at low latitudes, i.e., within $\pm 30^\circ$ around the equator as observed on the Sun. In this case it covers the eclipsed section where we find a darker surface, i.e., higher spot coverage. We caution that this result may also be influenced by the adopted planetary parameters (mainly the size), which are hard to determine accurately (Czesla et al. 2009).

We checked whether the effect of gravitational darkening could significantly contribute to a darker surface in the vicinity of the equator. For the stellar parameters of CoRoT-2a, we find that the (effective) gravitational accelerations at the poles and at the equator are equal to within 0.07%, so that gravitational darkening does not significantly contribute to the brightness gradient found in our modeling. This result is nearly independent of the assumed coefficient, β_1 ($T_{\text{eff}}^4 \propto g^{\beta_1}$ with the effective surface temperature T_{eff} and the surface gravity g), which is approximately 0.3–0.4 for CoRoT-2a (Claret 2000).

The “narrow-band hypothesis”, i.e., a higher spot coverage in the planet-eclipsed section compared to the noneclipsed surface, also provides a natural explanation for the fact that both the eclipsed and noneclipsed surface regions account for about the same amplitude of variation in the lightcurve. Using the Sun as an analogy again, we would qualitatively expect the same structure, as seen under the planet path, on the opposite hemisphere as well: two “active belts” that are symmetric with respect to the equator. The noneclipsed activity belt, which would be only observable in the global lightcurve, would then be primarily responsible for the variability of the lightcurve contributed by the noneclipsed surface section.

We conclude that our results support a surface model consisting of active regions north and south of the equator, possibly even bands of spots at low latitudes analogous to the Sun. Further investigations of this system using more sophisticated models (first of all surface evolution) and using the entire observation interval of approximately 140 days have the potential of revealing more information on the constantly changing surface distribution of spots on CoRoT-2a.

Acknowledgements. K.H. is a member of the DFG Graduiertenkolleg 1351 *Extrasolar Planets and their Host Stars*. S.C. and U.W. acknowledge DLR support (50OR0105).

References

- Alonso, R., Auvergne, M., Baglin, A., et al. 2008, *A&A*, 482, L21
 Alonso, R., Guillot, T., Mazeh, T., et al. 2009, *A&A*, 501, L23
 Auvergne, M., Bodin, P., Boisnard, L., et al. 2009, *A&A*, 506, 411
 Barnes, J. R., Cameron, A. C., Donati, J.-F., et al. 2005, *MNRAS*, 357, L1
 Bouchy, F., Queloz, D., Deleuil, M., et al. 2008, *A&A*, 482, L25
 Claret, A. 2000, *A&A*, 359, 289
 Czesla, S., Huber, K. F., Wolter, U., Schröter, S., & Schmitt, J. H. M. M. 2009, *A&A*, accepted
 Jeffers, S. V., Barnes, J. R., Cameron, A. C., & Donati, J.-F. 2006, *MNRAS*, 366, 667
 Lanza, A. F., Pagano, I., Leto, G., et al. 2009, *A&A*, 493, 193
 Press, W. H., Teukolsky, S. A., Vetterling, W. T., & Flannery, B. P. 1992, *Numerical recipes in C. The art of scientific computing*, ed. W. H. Press, S. A. Teukolsky, W. T. Vetterling, & B. P. Flannery (Cambridge University Press)
 Skrutskie, M. F., Cutri, R. M., Stiening, R., et al. 2006, *AJ*, 131, 1163
 Vogt, S. S., & Penrod, G. D. 1983, *PASP*, 95, 565
 Wolter, U., Schmitt, J. H. M. M., Huber, K. F., et al. 2009, *A&A*, 504, 561

A&A 514, A39 (2010)
 DOI: 10.1051/0004-6361/200913914
 © ESO 2010

**Astronomy
&
Astrophysics**

Planetary eclipse mapping of CoRoT-2a Evolution, differential rotation, and spot migration

K. F. Huber, S. Czesla, U. Wolter, and J. H. M. M. Schmitt

Hamburger Sternwarte, Universität Hamburg, Gojenbergsweg 112, 21029 Hamburg, Germany

Received 18 December 2009 / Accepted 17 February 2010

ABSTRACT

The lightcurve of CoRoT-2 shows substantial rotational modulation and deformations of the planet's transit profiles caused by starspots. We consistently model the entire lightcurve, including both rotational modulation and transits, stretching over approximately 30 stellar rotations and 79 transits. The spot distribution and its evolution on the noneclipsed and eclipsed surface sections are presented and analyzed, making use of the high resolution achievable under the transit path.

We measure the average surface brightness on the eclipsed section to be $(5 \pm 1)\%$ lower than on the noneclipsed section. Adopting a solar spot contrast, the spot coverage on the entire surface reaches up to 19% and a maximum of almost 40% on the eclipsed section. Features under the transit path, i.e. close to the equator, rotate with a period close to 4.55 days. Significantly higher rotation periods are found for features on the noneclipsed section indicating a differential rotation of $\Delta\Omega > 0.1$. Spotted and unspotted regions in both surface sections concentrate on preferred longitudes separated by roughly 180° .

Key words. planetary systems – techniques: photometric – stars: activity – starspots – stars: individual: CoRoT-2a

1. Introduction

The space-based CoRoT mission (e.g. [Auvergne et al. 2009](#)), launched in late 2006, provides stellar photometry of unprecedented quality. One of CoRoT's primary tasks is the search for extra-solar planets using the transit method. So far several systems with eclipsing exoplanets were found, one of them CoRoT-2 harboring a giant close-in “hot-jupiter”.

The planet CoRoT-2b was discovered by [Alonso et al. \(2008\)](#), who determined the system parameters from transits and follow-up radial velocity (RV) measurements. [Bouchy et al. \(2008\)](#) observed the Rossiter-McLaughlin effect using additional RV measurements and determined the projected angle $\lambda = (7.2 \pm 4.5)^\circ$ between the stellar spin and the planetary orbital axis. [Lanza et al. \(2009\)](#) used the strong rotational modulation of the lightcurve to study the spot distribution and its evolution; they detect a stellar rotation period of $P_{\text{rot}} = (4.522 \pm 0.024)$ d and two active longitudes on opposite hemispheres. The secondary eclipse of the planet was first detected by [Alonso et al. \(2009\)](#) in white light. Later the analysis was refined and extended by [Snellen et al. \(2010\)](#), detecting significant thermal emission of the planet; [Gillon et al. \(2009\)](#) repeated this work using additional infrared data. They also find an offset of the secondary transit timing indicating a noncircular orbit.

The determination of the planetary parameters by [Alonso et al. \(2008\)](#) did not account for effects of stellar activity, which is in general not negligible for active stars. [Czesla et al. \(2009\)](#) re-analyze the transits and derive new parameters for the planet radius R_p/R_s and the orbital inclination i considering the deformation of transit profiles due to spot occultation. This is especially important for attempts to reconstruct active surface regions from transit profiles. An analysis of a single transit by [Wolter et al. \(2009\)](#) shows the potential of eclipse-mapping and yielded constraints on the properties of the detected starspot. Similar

approaches to analyze signatures of starspots in transit profiles were also carried out by [Pont et al. \(2007\)](#) (HD 189733) and [Rabus et al. \(2009\)](#) (TrES-1) primarily using data obtained with the Hubble Space Telescope. In a more comprehensive approach, [Huber et al. \(2009\)](#) reconstructed an interval of the CoRoT-2 lightcurve over two stellar rotations including the transits.

This work is based on the paper of [Huber et al. \(2009\)](#). We now analyze the *entire* data set of CoRoT-2, modeling both the rotational modulation of the global lightcurve and transits simultaneously. In this way we derive stellar surface maps for both the noneclipsed and the eclipsed section of the star.

2. Observations and data reduction

The data were obtained in the first *long run* of the CoRoT satellite (May 16 to Oct. 15, 2007). The planetary system CoRoT-2 (Star CorotID 0101206560) consists of an active solar-like G7V star and a large planetary companion on a close orbit. Due to its edge-on view and an orbit period of only about 1.7 days, this lightcurve contains about 80 transits, roughly 3 during each stellar rotation.

The large surface inhomogeneities of this very active star are clearly visible in the rotational modulation of the CoRoT lightcurve taken over approximately 140 days. Although there is surface evolution even on timescales of one stellar rotation, these changes are small compared to the modulation amplitude. Significant deformations of the transit profiles due to spots are also visible throughout the whole time series.

The stellar and planetary parameters used throughout this analysis are given in Table 1. The extensive raw data analysis and reduction follows the descriptions in [Czesla et al. \(2009\)](#) and [Huber et al. \(2009\)](#).

In this paper we only analyze the *alarm mode* data of CoRoT-2, when the satellite switched from a sampling

A&A 514, A39 (2010)

Table 1. Stellar/planetary parameters of CoRoT-2a/b.

Star ^a	Value \pm Error	Ref.
P_s	(4.522 \pm 0.024) d	L09
Spectral type	G7V	B08
Planet ^b	Value \pm Error	Ref.
P_p	(1.7429964 \pm 0.0000017) d	A08
T_c [BJD]	(2 454 237.53562 \pm 0.00014) d	A08
i	(87.7 \pm 0.2) $^\circ$	C09
R_p/R_s	(0.172 \pm 0.001)	C09
a/R_s	(6.70 \pm 0.03)	A08
u_a, u_b	(0.41 \pm 0.03), (0.06 \pm 0.03)	A08

References. taken from Lanza et al. (2009) [L09], Alonso et al. (2008) [A08], Bouchy et al. (2008) [B08], or Czesla et al. (2009) [C09].

Notes. ^(a) P_s - stellar rotation period; ^(b) P_p - orbital period, T_c - central time of first transit, i - orbital inclination, R_p, R_s - planetary and stellar radii, a - semi major axis of planetary orbit, u_a, u_b - linear and quadratic limb darkening coefficients.

rate of $1/512 \text{ s}^{-1}$ to $1/32 \text{ s}^{-1}$ (which started after 3 transits), and use the combination of the three color channels (“white” light). Our analysis starts after one stellar rotation at $\text{JD} = T_c + P_s = 2454242.05562$ (see Table 1) or a stellar rotation phase of $\phi_s = 1.0$, respectively. We use units of stellar rotation phase in our analysis, the last point of our data interval corresponds to $\phi_s = 31.24$. This leaves us with an observation span of more than 30 stellar rotations containing 79 transits. In the following the first transit inside our data interval is labeled 0, the last 78.

3. Analysis

3.1. The model

The projected axes of the planetary orbit and the stellar rotation are co-aligned (Bouchy et al. 2008), which strongly suggests a 3-dimensional alignment. Hence, the rotation axis of CoRoT-2a is inclined by approximately 88° . While this impedes the reconstruction of latitudinal information of surface features, the existence of a planet crossing the stellar disk allows to access latitudinal information on spots beneath its path. During a planetary passage the surface brightness distribution is mapped onto the lightcurve as deformations of the transit profiles. As a consequence of the co-aligned orientation of the planetary orbit and the stellar spin, the surface band scanned by the planetary disk remains the same: the planet constantly crosses the latitudinal band between 6° and 26° . Accordingly, the stellar surface can be subdivided into two sections: the eclipsed section and the noneclipsed section (cf., Huber et al. 2009).

Our surface model subdivides the two individual sections into a number of “strips”; N_e is the number of strips in the eclipsed and N_n in the noneclipsed section, respectively. Each strip represents a longitudinal interval inside the latitudinal boundaries of the corresponding section. The layout of our surface model is shown in Fig. 1 of Huber et al. (2009).

3.1.1. Model resolution and error estimation

The problem of lightcurve inversion is well known to be ill-posed, so that the parameter space is usually further constraint by a regularization. One such regularization is the maximum

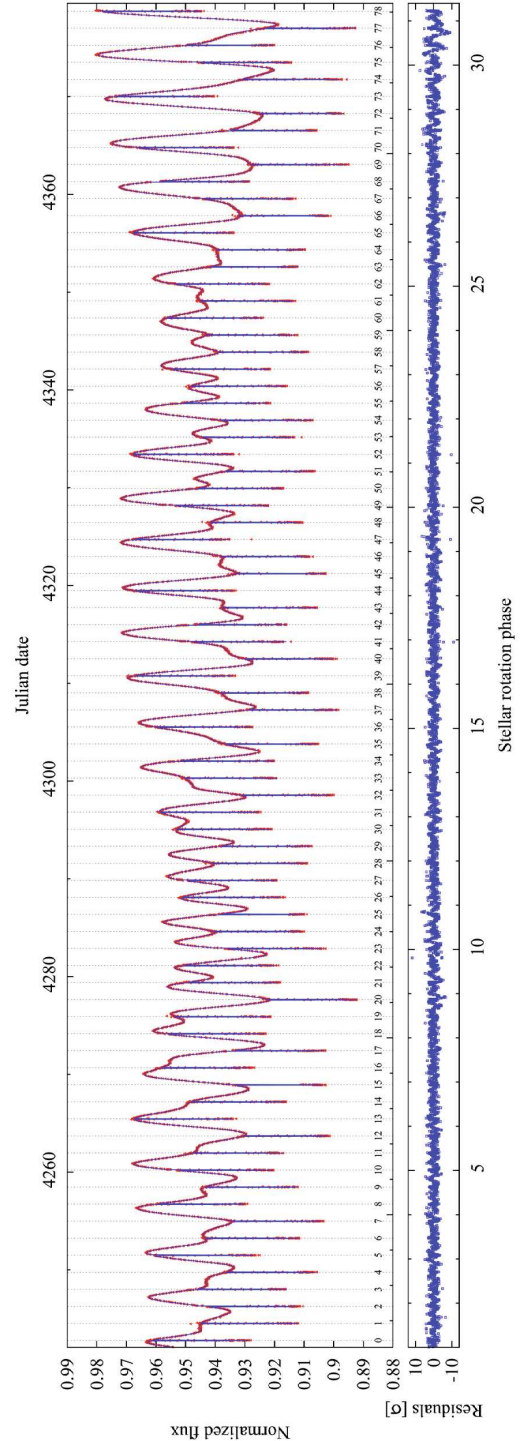


Fig. 1. Observations and best fit model for CoRoT-2. The transit numbers are plotted below the lightcurve; for a detailed presentation of the transits see Fig. 9. See Sect. 3.4 for discussion.

entropy approach, applied, for example, by Lanza et al. (2009) in their analysis of CoRoT-2a.

We use a Nelder-Mead (NM) Simplex algorithm for minimization (Press et al. 1992). Our model does not require any

K. F. Huber et al.: Planetary eclipse mapping of CoRoT-2a

regularization because of its relatively small number of parameters. As discussed by Huber et al. (2009), we choose a number of strips balancing the improvement in χ^2 and the deterioration in uniqueness. For higher strip numbers, adjacent strips increasingly influence each other because brightness can be redistributed without significant loss of fit quality. In our error analysis we assume that there is a unique best-fit solution to our problem and that the NM algorithm approaches it to within the limits of its ability to converge. Starting from the yet unknown best-fit solution, brightness can be redistributed among the strips at the expense of fit quality. A set of Nelder-Mead fit runs will, therefore, provide a sequence of solutions with different realizations of this brightness redistribution.

We calculate 50 reconstructions with randomized starting points and adopt the average of all reconstructions as our most appropriate model. As an estimate for the error of the strip brightness, we use the standard deviation of the parameter values, obtained from the set of reconstructions.

We do point out that the averaged solution appears smoother than most individual reconstructions in the sense that the difference between adjacent strip brightnesses is smaller. This can be understood in the picture of brightness redistribution, because the brightening of one strip may preferably be compensated by darkening an adjacent one, which increases their contrast. This effect is largely canceled out by the averaging, which makes it appear much like a regularization of the solutions.

It may be criticized that the brightness error we use is largely determined by the ability of the NM algorithm to converge to a unique solution. We emphasize, however, that the χ^2 range covered by the 50 reconstructions exceeds that required for ‘classical’ error analysis, and the estimate will, therefore, remain rather conservative from that point of view.

Our test runs indicate that for our purpose the most appropriate number of strips to choose for the noneclipsed section is $N_n = 12$, which will be used in our analysis. Larger numbers of N_n appear to already oversample the surface significantly. The strip number for the eclipsed section is chosen to be $N_e = 24$ which approximately reflects the size of features that are resolvable inside of transits (Huber et al. 2009).

3.2. Normalization

The observations are normalized with respect to the ab initio unknown spot-free photospheric flux of the star, which is defined as maximum brightness $b_{\text{phot}} = 1$. Unfortunately, it is not trivial to obtain this photospheric flux level because spots are likely to be located on the visible disk at all times.

A possible solution for this problem is to adopt the maximum observed flux as photospheric. However, this presumably introduces an error because the brightest part of the lightcurve shows only the flux level of the stellar disk during the minimum observed spot coverage, which needs not be zero. Lanza et al. (2009) determine an average minimum of flux deficit of approximately 2.5%. Tests with slightly varying maximum brightness values in our reconstructions show no qualitative difference in the brightness distribution except for a change in the average total spot coverage; however, they show a significant decrease in χ^2 of the lightcurve reconstructions for a maximum brightness 1% to 2% larger than the highest observed flux. As a result we choose a photospheric flux level of 2% higher than the maximum observed flux. The entire lightcurve is normalized with respect to this value.

3.3. Lightcurve modeling

For analysis, the lightcurve is split into equally sized intervals, each covering one stellar rotation and three transits. Due to surface evolution detectable on timescales smaller than one stellar rotation, we choose to define a new interval after each transit. Thus, the resulting intervals overlap. Interval 0 contains the transits number 0 to 2, interval 1 contains the transits number 1 to 3, and so on. This way we end up with 76 lightcurve intervals which are individually reconstructed by our modeling algorithm.

Using fit intervals smaller than one stellar rotation could further reduce the influence of surface evolution. However, we need at least three transits in each interval to sufficiently cover the eclipsed section. Therefore, we always use a complete rotation for each reconstruction interval.

We use the fitting method presented in Huber et al. (2009). Each fit interval is rebinned to $94 \times 32 = 3008$ seconds for the global lightcurve and to 128 seconds inside of transits. Transit points are weighted with a factor of 10 higher than global points to give them approximately the same weight in the minimization process. We assume the planet to be a dark sphere without any emission; this seems to be a good approximation considering a secondary transit depth of about $(0.006 \pm 0.002)\%$ (Alonso et al. 2009). All other necessary parameters can be found in Table 1.

We introduce a penalty function to suppress reconstructed brightnesses above the photospheric value of one. Without this boundary the brightness of individual strips exceeds this limit in some reconstructions. Strips with values above unity must be interpreted as regions with a brightness greater than the (defined) photosphere; however, in this approach we want to consider only cool surface features, which was found to be a good approximation by Lanza et al. (2009). Several tests showed that this penalty function does not significantly alter the outcome of our reconstructions; it primarily prevents the minimization process from getting stuck in (local) minima outside the relevant parameter range.

To analyze the transits accurately, we require an ‘undisturbed transit profile’, which means a profile corrected for the effects of stellar activity. This ‘standard transit profile’ was determined by Czesla et al. (2009), where a planet size of $R_p/R_s = 0.172$ was found. With the planetary parameters derived by Alonso et al. (2008) no satisfactory fits to the transits and global lightcurve can be produced.

3.4. Results of the modeling

We present our lightcurve reconstruction in Fig. 1. It shows the observed CoRoT-2 lightcurve (red triangles), including the transits, and our reconstruction (blue solid line). The shown reconstructed lightcurve is a combination of all models for the 76 fit intervals; their overlaps were combined using a Gaussian weighting. Each transit is labeled with its number on the lower edge of the graph; a more detailed picture of their fits is given in Fig. 9, where we present all transits in a stacked plot.

Below the lightcurve the residuals $\sigma = (O - C)/\sigma_O$ (O -observed lightcurve, C -reconstructed lightcurve, σ_O -error of observation) are given. The mean values for σ_O are 1.8×10^{-4} outside and 6.9×10^{-4} inside of transits. Maximum values of the residuals are approximately 10σ , which corresponds to a deviation of about 0.2% between the observed and reconstructed lightcurves. On average, the absolute values of residuals are 1.12σ or $O - C = 4.4 \times 10^{-4}$, respectively.

A&A 514, A39 (2010)

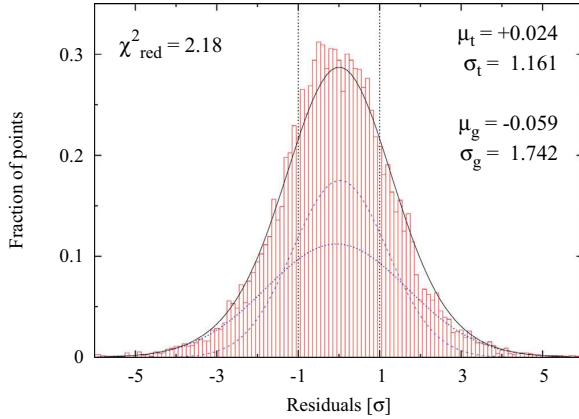


Fig. 2. Distribution of residuals σ between the observations and the best fit model (see Fig. 1). The overall distribution is the sum of two Gaussians, one coming from inside the transits (mean μ_t and width σ_t) and the other coming from outside of them (global, mean μ_g and width σ_g). For details see Sect. 3.4.

Figure 2 shows the distribution of residuals from Fig. 1. It is approximately Gaussian, although the underlying distribution is twofold: one component is a Gaussian distribution of residuals from inside the transits with $\sigma_t = 1.161$, and another broader component is coming from the residuals of the global lightcurve, which is significantly wider with $\sigma_g = 1.742$. The addition of both Gaussians reproduces the overall distribution of residuals accurately. We calculate $\chi^2_{\text{red}} = 2.18$ from all residuals of the entire lightcurve.

The interpretation of χ^2_{red} as an actual goodness-of-fit indicator is not straightforward in this case. An increase of the strip number should lead towards χ^2_{red} values of 1. Test calculations show that our fit quality cannot be substantially improved beyond a certain level when the number of strips is increased. This level of χ^2_{red} primarily reflects the evolution of the lightcurve within one stellar rotation, which cannot be improved within our static model, and which is especially visible in the global lightcurve ($\sigma_g \gg \sigma_t$). Unfortunately, it is very hard to quantify this effect.

3.5. Construction of brightness maps

In Fig. 3 we present maps of the temporal evolution of the brightness distributions. The left panel gives the brightness map for the noneclipsed, the right panel for the eclipsed surface section. The rows show the reconstructed brightness distributions for all 76 lightcurve intervals; each interval is labeled by the number of the first transit it contains. Due to the different resolutions in the two surface sections, we linearly interpolate the brightness values in each individual row; there is no interpolation applied between different rows. To generate the combined brightness map shown in Fig. 8 (left panel), the maps of the two separated sections are weighted, corresponding to their disk fraction of 0.79 for the noneclipsed and 0.21 for the eclipsed section, and added. The errors are combined the same way. Adjacent rows in our maps are not independent because the fit interval is only shifted by one transit ($\approx 1/3$ stellar rotation) when moving from one row to the next.

The errors are displayed directly below each map. For the brightness values of the global lightcurve fit (Fig. 3, left panel), the mean error is about 1%, for the transits (Fig. 3, right panel) it

is approximately 3%. The errors in the latter map are larger (on average) and more inhomogeneously distributed because they also reflect the coverage of the eclipsed section by the transits; areas only marginally visible in transits cannot be reconstructed with high accuracy.

The stellar longitude scale of our maps runs backwards from 360° to 0° . This is due to our retrograde definition of the stellar longitude l compared to stellar phases ϕ_s ; their relation is $l = (\phi_N - \phi_s) \cdot 360^\circ$ (with an integer stellar rotation number $\phi_N = [\phi_s] + 1$).

The identification of significant structures in these maps deserves some attention. The brightness information is color coded using black color for the darkest structures and white for photospheric brightness. Considering the approximate mean error of each map, we indicate areas with a brightness significantly below unity with yellow color. Hence, not only black areas of these maps are spots but yellow structures represent a significant decrease in brightness as well.

4. Discussion

In this section we discuss and interpret the spot distributions of our brightness maps and their evolution. This involves quite a few different aspects, which are often difficult to disentangle, and on which we focus on individually in the following subsections.

4.1. Identifying physical processes and detection limits

Our brightness maps allow us to witness the evolution of the stellar surface and, to some degree, to discriminate between individual processes causing changes of the spot distribution: Emergence/dissociation, differential rotation, or migration of surface features leave potentially distinguishable signatures. Unfortunately, the high diversity of CoRoT-2a's surface and a limited resolution complicate the interpretation of these signatures.

On the eclipsed section the position of a feature is fairly well known and it is likely to be physically coherent. On the noneclipsed section it is not clear whether a feature is actually a single connected active region or a superposition of two (or even several) different regions.

Features on the eclipsed section provide a valuable reference point for the detection of differential rotation. Systematic longitudinal movements of spots in the transit map do not indicate differential rotation but rather a difference to the input rotation period. However, a comparison of transit and global maps could reveal different rotation periods on different surface sections.

Systematic longitudinal movements of structures in the global map do not necessarily indicate differential rotation either. A simultaneous decay and growth of two distinct active regions at different longitudes might leave a signature similar to a single differentially rotating active region. Therefore, the processes of differential rotation and spot evolution are hard to discern.

A very interesting scenario is the possibility to find spot migration due to the planet. If a spot moves from the noneclipsed to the eclipsed section, its signature also moves from the global to the transit brightness map. If present, such signatures are detectable in high quality brightness maps.

In the following discussion we attempt to attribute signatures in the brightness maps to the specific *processes* discussed above. Depending on the number of longitudinal strips used, map structures have an estimated error in longitude of about half the strip

K. F. Huber et al.: Planetary eclipse mapping of CoRoT-2a

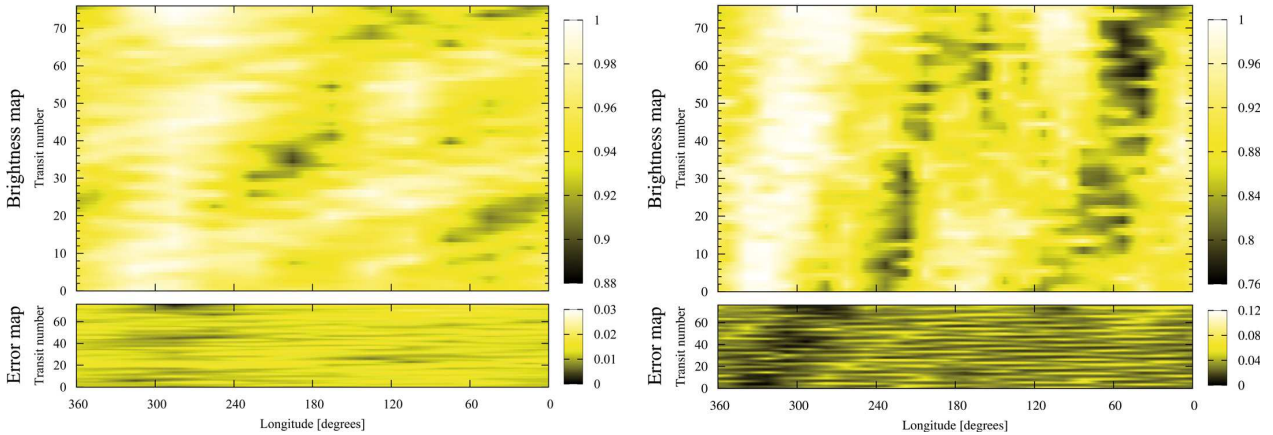


Fig. 3. *Left panel:* brightness map reconstructed from the global lightcurve (noneclipsed surface). *Right panel:* brightness map for the reconstructions of the transits (eclipsed surface). The combination of both maps is presented in Fig. 8. Each row presents the reconstructed brightness distribution of one fit interval; the transit number indicates the number of this interval’s first transit. Each step in transit number equals a temporal step of 1.74 days. The brightness is color-coded, the maximum photospheric brightness is unity. The error maps at the bottom of each panel show the estimated reconstruction error. See Sects. 3.3 and 3.5 for details.

width, which is about $\pm 7.5^\circ$ for the transit and $\pm 15^\circ$ for the global map, respectively.

4.2. Spot coverage

The brightness maps of Fig. 3 show clear evidence of (a) a coverage of a large fraction of the surface with dark features and (b) a substantial evolution of this spot distribution within the roughly 140 days of observations. Considering the pronounced rotational modulation of the lightcurve, and the persistently changing shape between individual rotations, this result is hardly surprising. The lowest flux of the rotationally-modulated lightcurve is about 0.92 (modulo the uncertainty in lightcurve normalization, see Sect. 3.2); if the starspots were absolutely dark, they would still cover 8% of the disk. The largest peak-to-peak variation during one rotation spans from 0.98 to 0.92 indicating roughly 6% more spots on the darker hemisphere.

Using a spot contrast of $c_s = 0.7$, which is about the average bolometric contrast of sunspots (Beck & Chapman 1993; Chapman et al. 1994), we determine a maximum spot coverage of 37% on the eclipsed and 16% on the noneclipsed section. For the entire stellar surface a maximum and minimum spot coverage of 19% and 16% are derived.

Details on brightness values and spot coverage can be found in Fig. 4. The average brightness B is the mean brightness of each reconstruction interval. The top panel gives the ratio between the mean brightness of the eclipsed and noneclipsed sections, the second and third panel (from top) the eclipsed and noneclipsed brightnesses separately, and the bottom panel shows the variation of the total brightness $B_{\text{Total}} = (1 - A) \cdot B_{\text{ecl.}} + A \cdot B_{\text{non-ecl.}}$ with $A = 0.79$. The associated spot coverage fraction is calculated using $(1 - B)/(1 - c_s)$.

Instead of converting brightness into spot coverage, we can also reverse the process. Assuming the darkest element of the transit map is entirely covered by one spot, the reconstructed brightness represents the spot contrast. One strip on the eclipsed section has a size of about 1% of the entire surface. We obtain a value of 0.76 for the darkest surface element of the transit map, which is not far from the solar spot contrast of 0.7. The minimum brightness of 0.76 can be translated into a temperature contrast

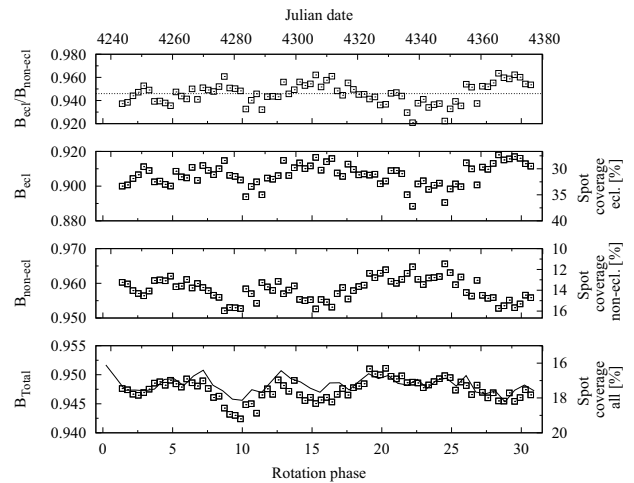


Fig. 4. Average brightness values of the eclipsed ($B_{\text{ecl.}}$) and noneclipsed ($B_{\text{non-ecl.}}$) sections for each reconstruction interval. The y -axes on the right show the corresponding spot coverage for a spot contrast of 0.7. *Top panel:* ratio $B_{\text{ecl.}}/B_{\text{non-ecl.}}$ of the mean brightnesses. *Second panel from top:* mean brightness and spot coverage for the eclipsed section. *Third panel from top:* mean brightness and spot coverage for the noneclipsed section. *Bottom panel:* total brightness B_{Total} ; the black curve shows the results of Lanza et al. (2009) shifted by +9% (see Sect. 4.2).

of ~ 400 K between the spot and the photosphere, which is at $T_p = 5625$ K (Bouchy et al. 2008).

4.3. Rotation period

For CoRoT-2a Lanza et al. (2009) determine a rotation period of (4.52 ± 0.14) d by means of the Lomb-Scargle periodogram, which the authors later refine to be $P_s = (4.522 \pm 0.024)$ days by minimizing the longitudinal migration of their active longitudes. We adopted P_s for our reconstructions. It is almost identical to the largest peak in the Lomb-Scargle periodogram (Fig. 5)

A&A 514, A39 (2010)

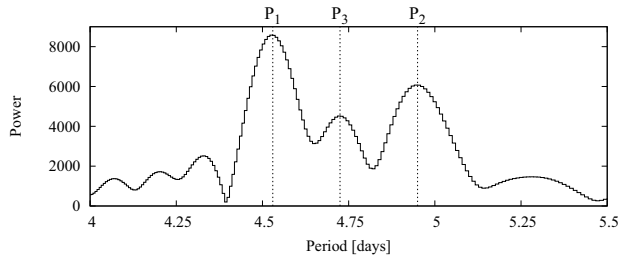


Fig. 5. Section of the Lomb-Scargle periodogram of the CoRoT-2 lightcurve containing the highest peak. The three peaks are labeled $P_1 = 4.53$, $P_2 = 4.95$, and $P_3 = 4.72$ days according to decreasing power. The adopted rotation period of our reconstructions, $P_s = 4.522$ days (Lanza et al. 2009), is close to P_1 .

centered at $P_1 = 4.53$ d. P_1 is accompanied by two other distinguishable peaks at $P_2 = 4.95$ d and $P_3 = 4.72$ d, which are related to structures in our surface maps as discussed in Sect. 4.4.

Since the planet crosses the stellar disk in a latitudinal band between 6° and 26° , spots on the eclipsed section must be located close to the equator. The approximate vertical alignment of the darkest features in the transit map indicates that low-latitude features rotate close to the adopted rotation period of 4.522 days used in our reconstructions. In contrast, features on the noneclipsed section do show longitudinal migration, which may be attributed to differential rotation of spot groups at latitudes $\geq 30^\circ$. This finding suggests that active regions close to the equator dominate the modulation of the lightcurve.

A closer inspection of the transit map shows a small but constant longitudinal shift of about 60° over the entire 30 rotations. It is not only visible in the dark structures located at $\sim 200^\circ$ and $\sim 60^\circ$ longitude, but for the bright region at $\sim 300^\circ$ as well. As a consequence, these low-latitude features do not rotate exactly with a rotation period of 4.522 days but about 2° per rotation more slowly, which translates into a rotation period of approximately 4.55 days. Lanza et al. (2009) state a retrograde migration of their second active longitude corresponding to this rotation period.

We recalculated the surface reconstructions adopting a rotation period of 4.55 days. As expected the longitudinal shift previously detected in the transit map disappeared, but some features now seem to migrate in the other direction. Therefore, the exact rotation period of features on the eclipsed section is probably slightly smaller than 4.55 days. The global map changes accordingly when using a rotation period of 4.55 days; the brightness distribution reconstructed at larger transit numbers is shifted towards larger longitudes, but remains qualitatively the same, so that these maps are not presented separately.

4.4. Longitudinal movement / differential rotation

Some attributes of the global map suggest a longitudinal movement of surface structures; a labeling of particularly interesting regions is given in Fig. 6. Especially considering the inactive regions, the bright structure B1 at the bottom left appears to move from $\sim 300^\circ$ to $\sim 100^\circ$ (B2) within about 4 stellar rotations. It continues moving in the direction of decreasing longitude reaching roughly 240° near transit number 50 (B3). Regions B4 and B5 do not seem to fit well into the line drawn by B1, B2, and B3. However, a line connecting B4 and B5 roughly matches with the previously detected rotation period between 4.8 and 5.0 days. The tilted shape of the dark structure D1 roughly agrees with

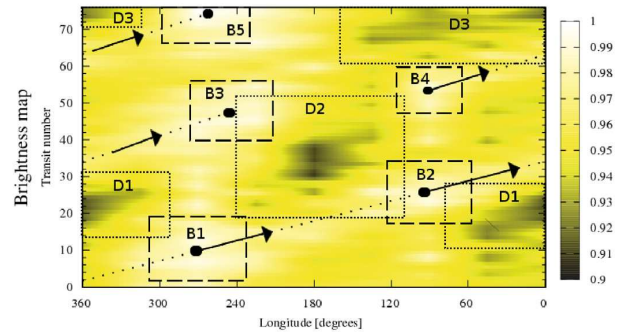


Fig. 6. The global surface map (left panel of Fig. 3) with pronounced dark and bright features marked and labeled D1 – D3 and B1 – B5, respectively. The dash-dotted line and the arrows indicate the tentative movement of bright regions (see Sect. 4.4).

this range of periods as well. D2 indicates a smaller rotation period consistent with P_3 .

Although such surface map characteristics do not necessarily prove differential rotation, they are certainly suggestive of differential rotation. Assuming now this to be correct, we will elaborate on its consequences. The largest rotation periods we obtain from structures of the global map lie between about 4.8 and 5.0 days. We studied the longitudinal movements of these structures on surface maps obtained from lightcurve reconstructions applying different rotation periods and always end up with similar results. An examination of CoRoT-2's periodogram reveals a splitting up of the highest peak into three components: $P_1 = 4.53$ d, $P_2 = 4.95$ d, and $P_3 = 4.72$ d (see Fig. 5). It is striking that P_2 is close to the rotation period determined from tilted structures in our global map.

If these rotation periods do arise from differential rotation, we can estimate a lower limit of its strength. The rotation period of eclipsed spots close to the equator is consistent with the highest peak $P_1 = 4.53$ days of the periodogram, the largest periods detected in the global map are around $P_2 = 4.95$ days; therefore, we adopt this period for the most slowly rotating active regions. This way we determine a lower limit of $\Delta\Omega > 0.1$ rad/d or $\alpha > 0.08$. This is consistent with values expected for stars with temperatures and rotation periods similar to that of CoRoT-2 (Barnes et al. 2005). Using a 3-spot model approach, Fröhlich et al. (2009) derive an estimate of $\Delta\Omega > 0.11$ rad/d, which is in good agreement with our result.

Although the peaks in the periodogram fit nicely in with our brightness maps, attributing them to three active regions with associated rotation periods may not be fully adequate. We simulated several lightcurves with differentially rotating spots and examined their periodograms. Although the main peak splits up into different components, the periodogram does not necessarily map the exact rotation periods of the differentially rotating spots to the peak barycenters. An exhaustive analysis of the periodogram is beyond this work's scope, but the above approach may serve as an approximation, and it shows that the characteristics of the periodogram can be aligned with surface map attributes.

As an alternative, or maybe extension, to the interpretation in terms of differential rotation, an evolution of the global activity pattern should be considered, which does not invoke longitudinal movement of individual surface features, but a redistribution of strength between active regions. The spot distribution on the global map suggests sudden longitudinal relocations of

K. F. Huber et al.: Planetary eclipse mapping of CoRoT-2a

the most active feature. For the first ~ 25 transits the dominant spotted region D1 keeps its position at $\sim 30^\circ$ showing an apparent movement towards smaller longitudes at the end of this interval. Afterwards the dominant active region is found approximately 180° apart from the previous position in region D2. Such 180° -jumps, or rather “hemisphere-jumps”, as the value of 180° should not be taken too seriously here, are found for inactive (bright) regions as well.

An appealing explanation for this apparent shift is a change of the relative strength of two active regions, which does not involve movement of any of the structures themselves. These jumps are possibly a sign for some flip-flop scenario as already claimed for other stars (Jetsu et al. 1993; Korhonen et al. 2001), where the relative strength between two active longitudes is changing suddenly and periodically. The timescale of these “jump periods” derived from our global brightness map is roughly 10 stellar rotations; however, this is not seen in the transit map.

4.5. Lifetimes of features

Both the global and the transit map provide the possibility to measure lifetimes of spotted regions. For the noneclipsed section it is not clear whether a dark structure actually is a single connected active region or a superposition of several individual ones at roughly the same longitude but completely different latitudes.

The transit map shows a high stability of the spot positions. One group of spots is located between 200° and 240° , which is stable up to transit number 35; then the spot coverage seems to decrease for about one stellar rotation. Afterwards the spot distribution becomes more complicated and spreads over a larger area. The left part of this more complex region, at about 210° longitude, is probably a continuation of the preceding active region; however, at about 160° longitude a new, clearly separated group of spots appears. This latter structure appears to have a lifetime of approximately 10 stellar rotations, which would be in good agreement with timescales observed on the global map.

Another group of spots is located between 0° and 100° . At the beginning of the observation these spots are spread over this larger interval of about 100° on the eclipsed section; later, approximately after transit number ~ 50 , they seem to concentrate in a smaller interval. This active region seems to have a significant fine structure in time, which might indicate smaller lifetimes of individual spot groups; however, those structures could also be artifacts of the reconstruction algorithm. We prefer the interpretation that this active region, and the left side of the other active region, are persistent over all 30 rotations, although they probably contain smaller spots undergoing significant evolution on much shorter timescales.

The left side of both maps (around 300° in longitude) shows bright regions which are least covered by spots during all observations, indicating a lifetime of half a year for this “inactive longitude”. For the darkest structures of the global map, maximum lifetimes of about 10 to 15 stellar rotations can be estimated. This is in agreement with the results of Lanza et al. (2009), who determine a lifetime of ≈ 55 days (=12 stellar rotations) for active regions, and identify this time span with the “beat period” visible in the lightcurve.

Although there are some structures in the transit map that suggest smaller lifetimes than half a year for individual spot groups, the lifetimes of features on the two different surface sections seem to be different. A direct comparison of the global and the transit map is shown in Fig. 7. The active regions on

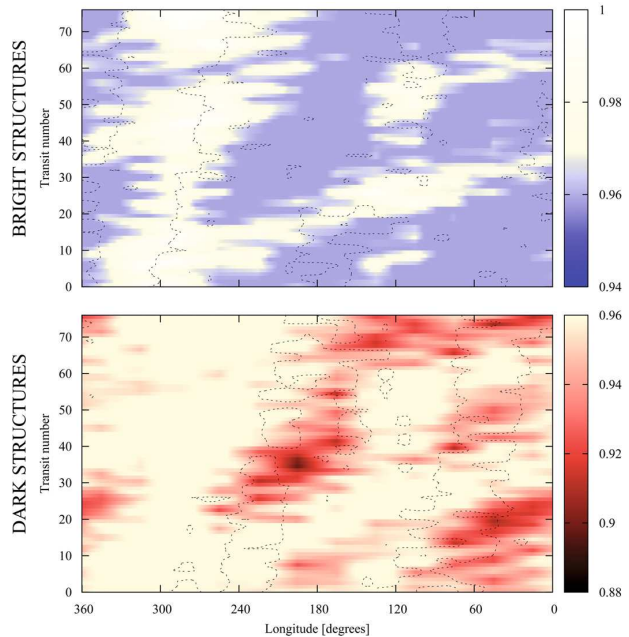


Fig. 7. Direct comparison of the two brightness maps of Fig. 3. The global map is drawn in color, structures of the transit map are shown with contour lines. *Upper panel:* map of bright structures in the global map with $b_{\text{non-ecl.}} > 0.95$. The contour line delimits brightness values of the transit map above $b_{\text{ecl.}} = 0.94$. *Lower panel:* map of dark structures with $b_{\text{non-ecl.}} < 0.95$. Here the contour lines indicate a transit map brightness of $b_{\text{ecl.}} = 0.87$.

the eclipsed section remain active all the time despite their possibly significant fine structure. In contrast, active regions on the noneclipsed section evolve faster showing more pronounced changes and a longitudinal movement compared to the spots on the eclipsed section. The reason for the apparent lifetime difference is not clear. Possibly the darkest structures represent only a superposition of several spotted groups at about the same latitude. If these groups change their mutual longitudinal positions, or a fraction of the spot groups dissolves, the dark structures in our maps would brighten. In this case the darkest structures would only represent special configurations of the spot distribution and their “lifetimes” in our maps would not be directly connected to the lifetimes of individual active regions on the surface.

The stable vertical alignment of features in our transit map cannot be caused by a systematically incorrect transit profile used in our reconstructions. The transits do not always cover exactly the same part of the eclipsed section, which is also visible in the error distribution of the transit map; dark structures indicate where the coverage is best, bright where it is worst. Thus, an error introduced by the transit profile would be distributed over the entire map.

4.6. Comparing global and transit maps: spot migration?

Finally, there is the possibility of detecting signatures of spot migration – the movement of spots from the equator to the poles or vice-versa – in our brightness maps. Figure 7 presents the direct comparison of the brightest structures (upper panel) and the darkest structures (lower panel) of the global and the transit map. Especially the dark structure D2 (see Fig. 6) in the middle of the lower panel’s map suggests that features on the eclipsed

A&A 514, A39 (2010)

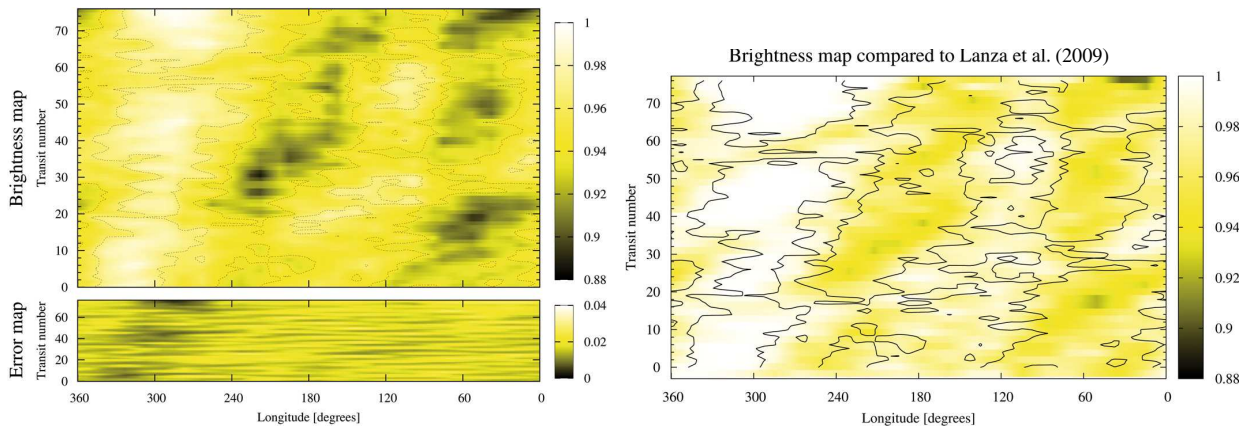


Fig. 8. *Left panel:* brightness distribution of the *entire* surface for all reconstructed intervals; it represents a combination of both the global and the transit map. The error for each bin of the brightness map is shown below. *Right panel:* comparison of our brightness distribution (contours) to the reconstruction of Lanza et al. (2009), which are shown in color coding. See Sect. 4.7 for details.

and noneclipsed sections are related. For the first 30 transits there is a dark feature of the transit map at this longitude, then it starts to disappear when D2 becomes darker. This reflects a scenario where a spot group moves from the eclipsed section to the noneclipsed. After transit number 40, D2 starts to disappear while other structures appear on the eclipsed section. If this really represents a case of spot migration, the spot group either moves back onto the eclipsed section, or it stays outside and new spots emerge under the transit path.

A similar observation can be made concerning the bright structures in the upper panel of Fig. 7. The bright structures in the transit map between 60° and 120° alternate with the bright regions B2 and B4. First there is a bright structure on the eclipsed map below region B2, then there is a little bit of both between B2 and B4, and after region B4 a bright structure is emerging in the transit map.

It is impossible to prove whether these signatures really represent spot migration; probably some of them are due to other processes, e.g. short-term evolution of spotted regions. Nevertheless, there is a similarity to what one would expect to see in brightness maps from surfaces showing spot migration. A behavior supporting a shift of spots from the eclipsed to the noneclipsed sections (and vice-versa) can be observed in Fig. 4 (second and third panel). It suggests a correlation between the mean brightnesses of the two sections; when the average brightness of the eclipsed section decreases, it increases on the noneclipsed part. However, this correlation does not necessarily prove a steady motion between the two sections and might as well indicate that vanishing spots just reappear somewhere else.

4.7. Comparison to previous results

Figure 8 (left panel) displays the combined brightness map derived from both the eclipsed (transit map) and noneclipsed sections (global map) of Fig. 3: the single maps are multiplied by their corresponding surface fractions (0.21 for the eclipsed and 0.79 for the noneclipsed) and added.

Lanza et al. (2009) present a map of the surface evolution derived from a fit to the global lightcurve (their Fig. 4) not including the transits. In the right panel of Fig. 8 we present a comparison of their results to ours. Since we do not use filling factors, we translated their map into brightnesses using their spot contrast of 0.665. We take the resulting map (color coding) and

superimpose it on our combined map from both the eclipsed and noneclipsed sections (contours). In the left panel of Fig. 8 the same contour lines are drawn to provide a better comparison. Lanza et al.'s and our results show good agreement, although a perfect match in fine-structure is neither found nor expected. Dark and bright structures are located at very similar positions and the shapes are consistent.

Adding up the brightness values of each reconstruction interval of the map in Fig. 8 (left panel), we can study the variations of the mean total brightness B_{Total} of the star. This is presented in Fig. 4 (bottom panel). With a maximum of $B_{\text{Total}} = 0.951$ and a minimum value of 0.942, the maximum difference between the highest and lowest average total brightness is only about 1%, which is much less than the maximum brightness differences within the brightness maps. This implies that the star as a whole does not change its overall spot coverage as dramatically as it redistributes it; when spots disappear, other spots show up. The solid line in the panel gives the comparison to the results of Lanza et al. (2009). We translated their values to our spot contrast of 0.7 and shifted it by a constant spot coverage of +9% to match our points. Our average spot coverage of 17.5% is roughly twice as high. Although, a 9% shift seems to be enormous, about 80% of it (+7%) can be attributed to a different normalization of the lightcurve and, thus, photosphere. While Lanza et al. (2009) define the maximum flux in the lightcurve as their photospheric level, our photosphere is 2% brighter (cf. Sect. 3.2), which has to be compensated by spots. We attribute the remaining 2% to the differences in the adopted models. In particular, we use longitudinal strips and spots can only be distributed homogeneously across a strips, while Lanza et al. (2009) localize the spots in 200 bins on the surface.

Previously, we detected an average brightness under the eclipsed section ($6 \pm 1\%$) higher than on the noneclipsed section (Huber et al. 2009). This value is redetermined from the reconstruction of the *entire* lightcurve presented in this paper. It decreases to ($5.4 \pm 0.9\%$) (see top panel of Fig. 4).

4.8. Brightness maps and lightcurve modulation

It is striking that the rotational variations of the star are additionally modulated with a beat period about a factor 10 to 15 larger. During the maxima of this large-scale modulation (at about transit numbers 15, 45, and at the end of the lightcurve), the minima

K. F. Huber et al.: Planetary eclipse mapping of CoRoT-2a

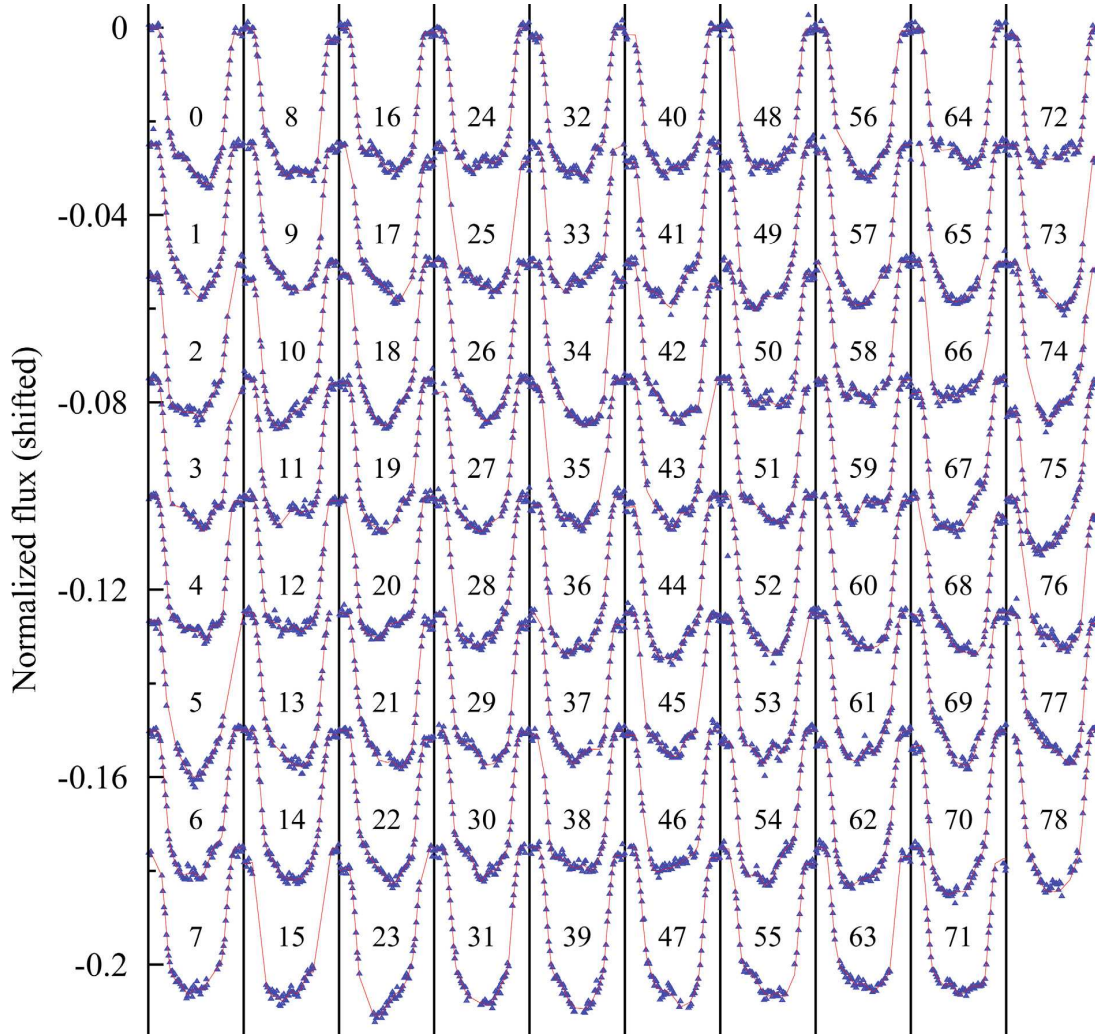


Fig. 9. Observation (blue triangles) and reconstruction (red solid line) of 79 transits from the CoRoT-2 lightcurve. The first transit of each column is shifted to a continuum of zero, each subsequent transit is shifted by -0.025 . The number of each transit is annotated inside the plot. See Fig. 1 for the entire lightcurve.

of the stellar rotation are deep and regular, i.e., the lightcurve has only one distinct minimum per rotation. During the minima of this beat period (at about transit numbers 30 and 60), the rotational modulation is flatter and more complex; the minima are split up in two. The beat period maxima indicate the existence of one large active region or longitude dominating the stellar surface. The minima indicate that two smaller active regions at significantly different longitudes imprint their signatures onto the lightcurve leaving double-peaked structures during one stellar rotation. This means dark regions are redistributed on timescales of 10 to 15 stellar rotations from essentially one large feature to at least two smaller, longitudinally separated ones, and then back to a large one.

This is also observable in our brightness maps. Figure 8 shows a change of the dominant surface feature from $\sim 60^\circ$ to $\sim 220^\circ$ at about transit number 20. Earlier the lightcurve was dominated by one large active longitude leading to one broad minimum during each rotation. During the transition phase, especially around transit number 25, the lightcurve minima become double-peaked. After transit number 30 the activity center

of the active longitude at 220° moves to about 180° and, thus, closer to the other active longitude at about 60° , which has not entirely disappeared and starts to grow stronger again. Because the active longitudes are closer now, the minima grow deeper; additionally, the bright region at 300° becomes larger and the maxima rise.

Again there are double-peak structures between transit numbers 55 and 60 for the same reasons. The decrease of the strong maxima is primarily due to the temporary change of the bright longitude at 300° . Interestingly, the amplitude and width of the minima become even larger at the end of the lightcurve, where the active longitudes first move closer together. In the end, the feature at $\sim 20^\circ$ becomes dominant spreading over almost 60° in longitude and leading to very low lightcurve minima.

The main reason why the rotation period of the star is so nicely indicated by almost constantly separated maxima of the lightcurve – despite the pronounced surface evolution – is that the on average brightest part of the surface, located on the inactive longitude at 300° , remains stable at its position.

A&A 514, A39 (2010)

5. Conclusions

We present a reconstruction of the complete CoRoT-2 lightcurve – including transits – covering about 140 days or 30 stellar rotations. In contrast to previous work, both the transit profiles and the rotationally-modulated global lightcurve are fitted simultaneously leading to a *consistent* solution for the entire lightcurve. From the transits the brightness distribution on the eclipsed surface section is recovered, which is the part of the surface between 6° and 26° latitude constantly eclipsed by the planet. The noneclipsed section is reconstructed from the rotational modulation.

The evolution of the spot distributions on both surface sections is presented in two maps showing the surface brightness distribution as a function of time. The composite map, which shows the evolution of the entire surface, is juxtapositioned with previously published results. The results are found to be in agreement taking into account different modeling approaches and assumptions.

The transit map shows two preferred longitudes densely covered with spots and separated by approximately 180° . Both active regions persist for the entire observing time of ~ 140 days, although they undergo significant evolution in size, structure, and brightness. In the transit map they show a constant retrograde movement indicating that the adopted stellar rotation period of $P_s = 4.522$ days does not exactly describe their rotation. We determine that these low-latitude features rotate at a period of approximately 4.55 days, which is also true for the long-lived inactive longitude at $\sim 300^\circ$.

The global map is more complex than the transit map presumably because the structures it describes represent a superposition of features at similar longitudes but different latitudes. Usually it shows only one dominant dark feature at a time, which changes position after approximately 10 to 15 stellar rotations. Again these dominant features are separated by about 180° in longitude. A persistent inactive longitude exists at about 300° similar to the one in the transit map and at about the same position. The global map indicates that there are features located on the noneclipsed section with significantly larger rotation periods than 4.522 days. This suggests the presence of differential rotation with spots moving more slowly at high latitudes than at low latitudes. We estimate a differential rotation of $\Delta\Omega > 0.1$ or $\alpha > 0.08$, respectively.

Assuming a spot contrast of 0.7, the spot coverage of the eclipsed section reaches a maximum of 37%, which is more than twice as large as the maximum on the noneclipsed section. *On average* the eclipsed section is $(5 \pm 1)\%$ darker than its noneclipsed counterpart. Sunspots are located within $\pm 30^\circ$ around the solar equator. Similarly, our results indicate that spot groups on CoRoT-2 are also concentrated in a low-latitude “active belt”.

Acknowledgements. We thank A. F. Lanza for kindly providing us with their results for comparison. K.H. is a member of the DFG Graduiertenkolleg 1351 *Extrasolar Planets and their Host Stars* and acknowledges its support. S.C. and U.W. acknowledge DLR support (50OR0105).

Note added in proof: Late in the review process, we became aware of a paper by Silva (2003, ApJ, 585, L147) where planetary eclipse mapping is modeled using images of the Sun. Contemporaneously to our work, Silva-Valio et al. (2010, A&A, 510, A25) used a very different approach to examine the transits of the CoRoT-2 lightcurve for properties of starspots.

References

- Alonso, R., Auvergne, M., Baglin, A., et al. 2008, A&A, 482, L21
 Alonso, R., Guillot, T., Mazeh, T., et al. 2009, A&A, 501, L23
 Auvergne, M., Bodin, P., Boisnard, L., et al. 2009, A&A, 506, 411
 Barnes, J. R., Cameron, A. C., Donati, J.-F., et al. 2005, MNRAS, 357, L1
 Beck, J. G., & Chapman, G. A. 1993, Sol. Phys., 146, 49
 Bouchy, F., Queloz, D., Deleuil, M., et al. 2008, A&A, 482, L25
 Chapman, G. A., Cookson, A. M., & Dobias, J. J. 1994, ApJ, 432, 403
 Czesla, S., Huber, K. F., Wolter, U., Schröter, S., & Schmitt, J. H. M. M. 2009, A&A, 505, 1277
 Fröhlich, H., Küker, M., Hatzes, A. P., & Strassmeier, K. G. 2009, A&A, 506, 263
 Gillon, M., Lanotte, A. A., Barman, T., et al. 2010, A&A, 511, A3
 Huber, K. F., Czesla, S., Wolter, U., & Schmitt, J. H. M. M. 2009, A&A, 508, 901
 Jetsu, L., Pelt, J., & Tuominen, I. 1993, A&A, 278, 449
 Korhonen, H., Berdyugina, S. V., Strassmeier, K. G., & Tuominen, I. 2001, A&A, 379, L30
 Lanza, A. F., Pagano, I., Leto, G., et al. 2009, A&A, 493, 193
 Pont, F., Gilliland, R. L., Moutou, C., et al. 2007, A&A, 476, 1347
 Press, W. H., Teukolsky, S. A., Vetterling, W. T., & Flannery, B. P. 1992, Numerical recipes in C. The art of scientific computing, ed. W. H. Press, S. A. Teukolsky, W. T. Vetterling, & B. P. Flannery (Cambridge University Press)
 Rabus, M., Alonso, R., Belmonte, J. A., et al. 2009, A&A, 494, 391
 Snellen, I. A. G., de Mooij, E. J. W., & Burrows, A. 2010, A&A, in press
 Wolter, U., Schmitt, J. H. M. M., Huber, K. F., et al. 2009, A&A, 504, 561

3 The X-ray perspective of magnetic activity in young stars and their environments

In this section I outline the development of X-ray astronomy and describe the most important characteristics of X-ray instrumentation. I give an overview of those aspects putting my work into context, and, finally, present my own contributions.

3.1 A short history of X-ray astronomy

The dawn of X-ray astronomy came in the wake of a new technology; namely that of rocketry. As the mean free path of X-ray photons in air (at sea level) is of the order of meters, the Earth's atmosphere must be left behind to observe an extraterrestrial source. The first X-ray observations were carried out using rocket-borne instrumentation. During one of the flights, the first extrasolar X-ray source, Scorpius X-1, was discovered (Giacconi et al. 1962). Although subsequent rocket experiments were carried out, the total X-ray exposure time available in 1970 was no more than about one hour.

This changed dramatically after December 12, 1970, when the first X-ray satellite, *UHURU*, was launched. *UHURU* carried out both an all-sky survey and pointed observations. It discovered 300 new X-ray sources and achieved an angular resolution of a few arcminutes, which allowed to identify the sources with various kinds of celestial objects. Among the most notable results of the mission are the discovery of enormous amounts of hot gas in galaxy clusters, which in one fell swoop doubled the mass of known baryonic matter in the local universe, and the realization that accretion can serve as a highly efficient energy source (for a summary see, e.g., Giacconi 2003).

The success of *UHURU* provided substantial momentum for the realization of successor missions, of which the first was Skylab, a

manned American space laboratory. It was, among others, equipped with instruments providing the first spatially resolved X-ray images of the Sun (e.g., Zombeck et al. 1978). The next extrasolar X-ray mission followed in 1978 when the *EINSTEIN* satellite was launched into orbit. Compared to *UHURU*, the *EINSTEIN* observatory provided enhanced resolution, sensitivity, and, for the first time, allowed for spectroscopy in the X-ray regime. With *EINSTEIN*, the number of X-ray sources and the detail in which they could be studied increased significantly. The data provided by *EINSTEIN* not only deepened our understanding of the extragalactic sources, but also revealed X-ray emission associated with virtually all kinds of main sequence stars. About two decades after *UHURU*, the ROSAT observatory was launched to carry out the next, much more efficient survey of the X-ray sky during which more than 100 000 sources were discovered. Besides the survey, many pointed observations were carried out until the mission ended in 1999. Although, more sensitive X-ray observatories are operated today, the ROSAT data remain the most recent all-sky survey.

Today, important X-ray telescopes for extrasolar observations are *Chandra*, *XMM-Newton*, *Suzaku*, and *Swift*, of which *Chandra* is the most relevant for the work at hand.

3.2 X-ray instrumentation

A major challenge in observational high energy astronomy is focusing the radiation. In the X-ray regime conventional mirrors as used in optical telescopes proved to be inappropriate for collecting light, so that an alternative approach was needed. A possible solution was proposed by Wolter (1952), and it was named after him.

The basic physical concept behind the working of a Wolter telescope is total reflection of X-ray photons after grazing incidence on metallic surfaces. Because of the required grazing photon incidence, the appearance of Wolter telescopes differs substantially from optical mirrors. As an example, Fig. 6 shows the telescope build for the *Chandra* X-ray observatory, which

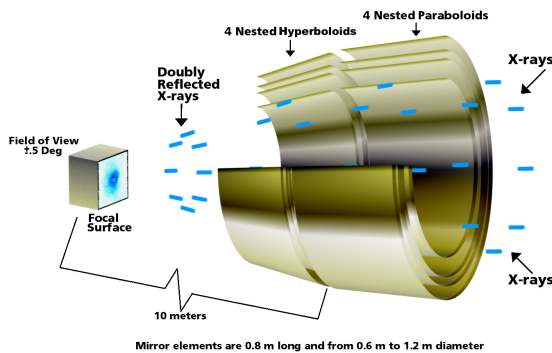


Figure 6: The Wolter telescope build for the *Chandra* X-ray observatory. Credit: NASA/CXC/D.Berry

consists of several nested shells of hyperbolic and parabolic metallic mirrors.

Although already proposed in 1952, it needed about three decades to realize the first Wolter telescope as a part of the *EINSTEIN* observatory. The typical wavelength scale of X-rays is 1 \AA , and this also defines the level of accuracy to be achieved in the production and placement of the reflecting surfaces. The mirror quality, which can be achieved, largely defines the angular resolving power of the telescope. Currently, the best resolution is about ≈ 0.5 arcsec reached only by *Chandra*.

For an X-ray telescope to be of any use, the collected photons have to be recorded. Several kinds of detectors have been used for this, whereof the most important are photographic plates applied in early experiments on board Skylab as well as proportional counters and microchannel plates for example build for *UHURU* and *ROSAT*. Today, the most widely used technique is the Charged-Coupled Device (CCD) detector, which provides both spatial and spectral resolution. It is, thus, possible to obtain imaging and spectroscopy simultaneously. For bright sources, a higher spectral resolution can be achieved using dispersion gratings, which are for example available for *XMM-Newton* or *Chandra*.

3.3 The *Chandra* X-ray observatory

The *Chandra* observatory is the third in the NASA series of “Great Observatories”, four major space-based observing facilities. It was proposed in 1976 and funding began soon after in 1977. First termed *AXAF* (Advanced X-ray Astrophysics Facility) the satellite was later renamed in honor of the Indian physicist Subrahmanyan Chandrasekhar.

After a long period of development, design, and building, the observatory was successfully launched on July 23, 1999. The *Chandra* orbit is highly eccentric ($e = 0.8$), placing it mostly above the Earth’s radiation belts. This leads to very advantageous background characteristics with a low level of contamination. A sketch indicating the major components of the observatory is given in Fig. 7. The spacecraft is 13.8 m long and harbors a mirror setup with an aperture of 1.2 m, illustrated in Fig. 6.

Chandra is equipped with four science instruments:

- HRC - High Resolution Camera,
- ACIS - Advanced CCD Imaging Spectrometer,
- HETG - High Energy Transmission Grating, and the
- LETG - Low Energy Transmission Grating.

Although the HRC and ACIS instruments can both be used for imaging, they are designed quite differently. The ACIS instrument is a CCD detector, and the HRC is basically a microchannel plate, which amplifies and records the electron cascades initiated by the ionizing X-ray photons. While the HRC provides the best spatial resolution, ACIS yields a better spectral resolution. This work mainly relies on ACIS data, which provide a spatial resolution of ≈ 0.5 arcsec and a spectral resolution of ≈ 100 eV at 6 keV.

Both the HETG and LETG are diffraction gratings, which can be inserted into the path of

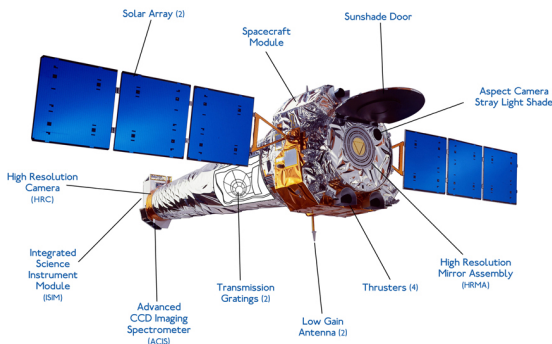


Figure 7: Major components of the *Chandra* X-ray observatory. Credit: NASA/CXC/NGST

light to obtain high resolution spectra of individual sources, which are recorded using ACIS.

Due to the great success of *Chandra* the initial 5 year mission schedule has been extended, and *Chandra* has currently been in operation for more than 10 years.

3.4 Stars in X-rays

The first direct detection of X-ray emission from the solar corona was made during a rocket flight in 1949 (Burnight 1949). About two decades later, Catura et al. (1975) reported the first discovery of X-ray emission from a stellar system, Capella, and their result was soon corroborated by Mewe et al. (1975), who were the first to explain the observed X-ray emission with the presence of a corona.

With the exception of extraordinarily hot sources such as white dwarfs, coronal X-ray emission of stars does not interfere with photospheric contributions, as is the case for optical or ultraviolet light. Therefore, X-ray emission provides an excellent means to study stellar coronae and stellar activity. Fortunately, we find a perfect example of a corona on our Sun, where it can be spatially resolved and studied in great detail. Rosner et al. (1978) formulated a model of the quiet solar corona, in which the magnetic field was a main ingredient, and the corona was made up of magnetic loops. The authors derived scaling laws for the coronal loops, which allowed to interpret the structure

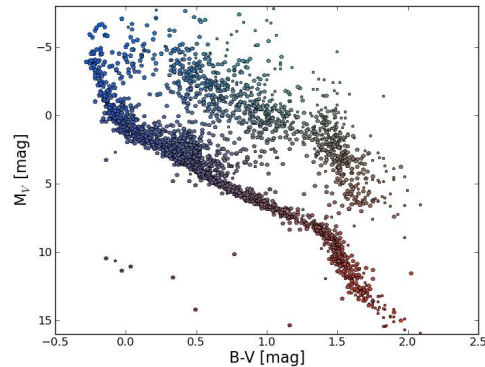


Figure 8: X-ray sources across the Hertzsprung-Russel diagram. Source sample compiled from Berghoefer et al. (1996), Hünsch et al. (1998a), Hünsch et al. (1998b), and Hünsch et al. (1999).

in the coronae of other stars as scaled versions of solar structures, without being able to actually resolve them.

Although stars have also been observed with other X-ray observatories, the progress achieved by the *EINSTEIN* and, in particular, the ROSAT observatory were outstanding. Before *EINSTEIN* only the most extreme stellar sources were known, but as *EINSTEIN* was observing the sky, stars all across the Hertzsprung-Russel diagram showed up as X-ray sources (Vaiana et al. 1981), and so were identified as a class of abundant X-ray emitters. The enhanced sensitivity of ROSAT allowed to study stellar populations in much more detail, in particular, it was possible to analyze volume limited samples of stars.

Schmitt et al. (1995) report an X-ray detection rate of $\approx 90\%$ among M and K type stars in the solar neighborhood (7 pc), and as the study was extended (Schmitt 1997) the authors found similar detection rates for G and F type stars within 13 pc from the Sun. Yet, Schmitt (1997) failed to detect a single A type star earlier than A7 from their sample; an outcome, consistent with X-ray emission originating in magnetically heated coronae, which should, indeed, not be present in such stars, because they

posses no outer convection zones. It should be noted that early A stars may actually be intrinsically X-ray bright in some cases, due to other mechanisms (Czesla & Schmitt 2007a, and references).

Massive B and O type stars were also found to be X-ray bright (Berghoefer et al. 1996), and their emission is believed to originate in shocks driven by their massive winds (e.g., Lucy & White 1980). Figure 8 shows the distribution of a ROSAT sample of X-ray sources in the Hertzsprung-Russel diagram. Clearly, the main sequence and the giant branch can be identified, and there is no type of star not showing up as an X-ray source.

Studies of activity indicators in the visual such as Ca II H&K (e.g., Baliunas et al. 1995) had already revealed that the stellar youth is a particularly active phase, a conclusion soon confirmed by X-ray observations. Star forming regions arise from the collapse of a large molecular cloud, in which dozens or thousands of stars are formed (see, e.g., McKee & Ostriker 2007, for an extensive review). The evolution of the newly born stars is divided into four categories, class 0-III. This classification mainly describes steps in the stellar evolution ranging from deeply embedded cores still in the process of collapse (class 0), over evolved protostars with envelopes and disks (class I), which evolve into pre main-sequence stars with disks from which they still accrete significant amounts of matter (class II, classical T-Tauri stars), and, finally, reach the weak-line T Tauri stage (class III) when accretion has virtually ceased.

It was *EINSTEIN* to discover the first X-rays from T Tauri stars. Feigelson & Decampli (1981) report the detection of X-ray emission from 8 T Tauri stars in Taurus and Orion, of which one, DG Tauri, was found to be highly variable; all were found to be quite X-ray bright with X-ray luminosities in the range of 10^{30-31} erg/s. The number of X-ray detected young stellar objects (YSO) was greatly increased by ROSAT. Yet, star forming regions are locations with a high source density, which are often deeply embedded in circumstellar material located in disks and envelopes as well

as in the remains of the cloud from which they emanated. This combination interfered with both the spatial resolution provided by the early X-ray observatories and the relatively soft bands (≤ 3 keV) which were covered.

The advent of XMM-*Newton* and *Chandra* revolutionized the study of star forming regions, because the available resolution and effective area increased by about an order of magnitude, and also the accessible band was extended mainly into the harder regime ($\approx 0.2 - 10$ keV). Using these observatories, several studies of star forming regions have been carried out; most notably the Taurus region was extensively observed with XMM-*Newton* in the frame of the “XMM-*Newton* extended survey of the Taurus molecular cloud” (Güdel et al. 2007) and Orion was targeted with *Chandra*. The observation of Orion is the deepest *Chandra* observation dedicated to a single star forming region and was carried out in the frame of the “*Chandra* Ultra-Deep Project” (COUP), which comprises about 1 Ms of exposure time distributed over ≈ 13 days. COUP revealed 1616 X-ray sources in Orion (Getman et al. 2005b), and the sources were then studied in many respects. For example, Getman et al. (2005a) investigated the Orion membership of the sources, Feigelson et al. (2005) analyzed the X-ray properties of the Orion region, and Preibisch et al. (2005) focused their effort on the origin of X-ray emission in T Tauri stars, to name but a few⁵.

The space-based X-ray observatories have demonstrated that virtually all stars are X-ray emitters, and the study of this emission has become a major tool in understanding the stellar activity and evolution.

3.5 How to study cool material in X-rays

X-rays can only be produced in environments, which allow the transfer of sufficiently large energy portions to photons. Appropriate conditions can for example be found in plasmas heated to millions of Kelvins or when

⁵see <http://www.astro.psu.edu/coup/> for a more complete listing of related works.

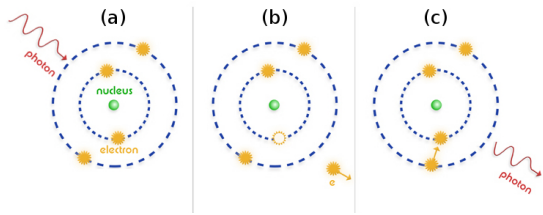


Figure 9: Sketch of a fluorescent event. Credit: NASA/CXC/M.Weiss

particles are accelerated to relativistic energies. Nonetheless, it is possible, under certain conditions, to study cold material in the X-ray regime.

Cold material can be studied by its effect on already produced X-rays. One possibility is to study the absorption characteristics of cold material. For example absorption edges, i.e., sudden changes in the absorption cross section originating in the structure of the atomic electron shells, can be used to draw conclusions on cold material, which, of course, must be located in the line of sight to do so. This restriction can be overcome by studying the radiation originating from reprocessing of X-rays in cold material. One such reprocessing channel is fluorescence.

The term “fluorescence” was coined by Stokes (1852) and derives from the mineral “fluorite”. A sketch of a fluorescent process is given in Fig. 9. A photon of energy ϵ_i is absorbed by an atom or ion (panel a) being left in an excited state with an electron vacancy on an inner shell (panel b). The ion possibly releases its excess energy in form of a photon with well defined energy, ϵ_o , i.e., a fluorescent photon (panel c), and the result of many such deexcitations is a narrow emission line at that energy. As already noted by Stokes, the energy of the reemitted photon is generally lower than that of the absorbed one ($\epsilon_o < \epsilon_i$). In the process, any charged particle, for example an electron, may take the role of the photon exciting the ion.

Fluorescent lines may in principle be observed from all elements contained in an illuminated cold plasma, yet, not all are of the same

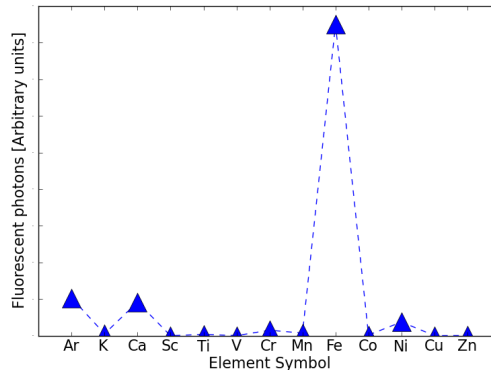


Figure 10: Estimate for the strength of the fluorescent $K\alpha$ line of several elements.

importance in astrophysics today. The fluorescent line gaining the most attention is that originating in neutral or lowly ionized iron (henceforth “Fe $K\alpha$ I line”) for several reasons. There is a strong fourth power dependence of the fluorescence yield, i.e., the probability for fluorescent deexcitation, on atomic number, making heavier elements stronger fluorescent sources, and iron is by an order of magnitude the most abundant element heavier than Neon. Assuming similar cross sections for photoelectric absorption, a rough estimate for the number of fluorescent photons contributed by a specific element, X , can be derived from

$$\text{strength} \sim Z^4 \times Ab(X) \times \int_{K_e}^{\infty} \frac{1}{\epsilon} e^{\epsilon/kT} d\epsilon. \quad (2)$$

Here, Z is the atomic number of the element, K_e is its K edge energy, and $kT = 3$ keV was assumed. Figure 10 shows the estimate for all elements with atomic numbers between 18 and 30, demonstrating the dominance of the iron contribution.

The Fe $K\alpha$ I line energy of ≈ 6.4 keV lies in a spectral region where the continuum contribution of typical thermal X-ray spectra with temperatures of a few keV is small, the density of other spectral features is low, and, finally, the energy band can be observed with today’s X-ray observatories.

The study of the Fe $K\alpha$ I line has not only become a major tool to analyze the

innermost portions of the engines operating in active galactic nuclei, where the gravitational attraction of the black hole dominates its environment, but is also a valuable instrument to study the less extreme environments of stars. In our Sun the Fe K_{α} I line has long been detected and used to study the composition of the solar photosphere. Promising sources beyond the solar system are young stars, which are still surrounded by the remains of the cloud they emanated from. In the two following publications, fluorescent X-ray emission from young stars in Orion is analyzed with a special emphasis on its temporal evolution.

The major contribution to these works was provided by myself, however, not without support and ideas provided by my supervisor J.H.M.M. Schmitt.

A&A 470, L13–L16 (2007)
 DOI: 10.1051/0004-6361:20077741
 © ESO 2007

**Astronomy
&
Astrophysics**

LETTER TO THE EDITOR

The nature of the fluorescent iron line in V 1486 Orionis

S. Czesla and J. H. H. M. Schmitt

Hamburger Sternwarte, Universität Hamburg, Gojenbergsweg 112, 21029 Hamburg, Germany
 e-mail: stefan.czesla@hs.uni-hamburg.de

Received 27 April 2007 / Accepted 24 May 2007

ABSTRACT

The fluorescent 6.4 keV iron line provides information on cool material in the vicinity of hard X-ray sources as well as on the characteristics of the X-ray sources themselves. First discovered in the X-ray spectra of the flaring Sun, X-ray binaries and active galactic nuclei (AGN), the fluorescent line was also observed in a number of stellar X-ray sources. The young stellar object (YSO) V1486 Ori was observed in the framework of the *Chandra* Ultra Deep Project (COUP) as the source COUP 331. We investigate its spectrum, with emphasis on the strength and time variability of the fluorescent iron K_{α} line, derive and analyze the light curve of COUP 331 and proceed with a time-resolved spectral analysis of the observation. The light curve of V 1486 Ori shows two major flares, the first one lasting for ≈ 20 ks with a peak X-ray luminosity of 2.6×10^{32} erg/s (dereddened in the 1–10 keV band) and the second one – only partially observed – for >60 ks with an average X-ray luminosity of 2.4×10^{31} erg/s (dereddened). The spectrum of the first flare is very well described by an absorbed thermal model at high temperature, with a pronounced 6.7 keV iron line complex, but without any fluorescent K_{α} line. The X-ray spectrum of the second flare is characterized by even higher temperatures (≥ 10 keV) without any detectable 6.7 keV Fe XXV feature, but with a very strong fluorescent iron K_{α} line appearing predominantly in the 20 ks rise phase of the flare. Preliminary model calculations indicate that photoionization is unlikely to account for the entire fluorescent emission during the rise phase.

Key words. stars: early-type – stars: activity – X-ray: stars

1. Introduction

The COUP data set provides a nearly continuous 13 day long X-ray observation of the Orion nebula star forming region and is currently one of the best suited data sets for the exploration of the X-ray properties of large and homogeneous samples of young stars. Substantial analysis of this data set has already been performed (e.g. by Getman et al. 2005). In particular, Tsujimoto et al. (2005) carried out a systematic search for the occurrence of the fluorescent iron K_{α} line at 6.4 keV, identifying 7 COUP sources with detectable fluorescent emission. This emission line is particularly interesting since it can provide a wealth of information on the emitting source(s). Fluorescent 6.4 keV photons – hereafter referred to as Fe I K_{α} photons – result from a de-excitation of neutral or lowly ionized iron atoms, following an excitation leaving the iron ion with a K-shell vacancy. When the latter is filled by another (mostly L-shell) electron, the excess energy can be carried by a fluorescent photon. Highly ionized iron can also show this behavior, but the transition energy rises because of the reduced screening of the inner electrons from the nuclear charge. Several processes lead to the ejection of a K-shell electron and, thus, to the creation of the Fe I K_{α} line. During the process of photoionization a K-shell electron is ejected from iron after the absorption of a photon with an energy exceeding 7.11 keV. Alternatively, high energy particles can eject K-shell electrons with the same threshold energy.

The first detection of the fluorescent Fe I K_{α} line was reported in the context of solar physics (e.g. Neupert et al. 1967). A model succeeding in explaining most of the solar Fe I K_{α} emission with photoionization only was proposed and

evaluated by Bai (1979), yet, e.g., Zarro et al. (1992) argue that photoionization alone is not sufficient to account for all of the solar Fe I K_{α} emission. Fluorescent K_{α} line emission has also been reported from other celestial X-ray sources. It is typically encountered in the high-energy emission from AGN and X-ray binaries, which are characterized by high X-ray luminosities and rather hard X-ray spectra, thus providing large photon numbers above the 7.11 keV threshold for photoionization. Fabian et al. (1989) detect the fluorescent iron line in the spectrum of the X-ray binary Cyg-X1, and Tanaka et al. (1995) were the first to report the relativistically broadened line in the spectrum of the AGN MCG-6-30-15. Recent observations with *XMM-Newton* and *Chandra* extended the class of Fe I K_{α} line emitters to a number of stellar sources, such as the class I YSO Elias 2-29 (Favata et al. 2005), the above seven COUP sources discussed by Tsujimoto et al. (2005), and the YSO YLW 16A for which Imanishi et al. (2001) carried out time-resolved spectroscopy.

In this letter we present a detailed analysis of the X-ray properties of the YSO V 1486 Ori (=COUP 331) with emphasis on its Fe I K_{α} emission, which was already reported by Tsujimoto et al. (2005), who measured a normalization of $2.6(0.1-4.6) \times 10^{-7}$ ph/(cm² s) with an equivalent width of 126 eV for the fluorescent line. Unfortunately, the YSO V 1486 Ori has so far not received much attention at other energy bands. From the 2MASS-all-sky survey we infer its infrared magnitudes as 12.5 mag, 10.6 mag, and 9.4 mag, in the *J*, *H*, and *K_s* bands, respectively. Tsujimoto et al. (2005) show that the infrared colors of V 1486 Ori do not match the regions of reddened dwarfs or giants and argue for the presence of a NIR-emitting inner disk. Moreover a rotation period of (6.09 ± 0.3) d is known for

L14

S. Czesla and J. H. H. M. Schmitt: The nature of the fluorescent iron line in V 1486 Orionis

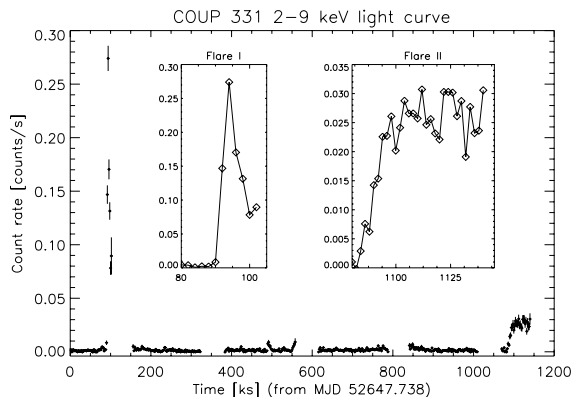


Fig. 1. Background-subtracted light curve of COUP 331 with 2 ks binning. Inserted panels show close-up views of the flares I and II.

V 1486 Ori (Herbst et al. 2002; Stassun et al. 1999). Following Tsujimoto et al. (2005) we adopt a distance of 450 pc for Orion.

2. Observations and data analysis

The COUP data was obtained during 13 consecutive days in Jan. 2003 with the Advanced CCD Imaging Spectrometer (ACIS) on board the *Chandra* X-ray observatory. The total exposure time is ≈ 840 ks, separated into 6 observation segments extending over a total time of ≈ 1140 ks. All observations have the same aimpoint ($\alpha = 5^{\text{h}}35^{\text{m}}17^{\text{s}}$ and $\delta = -5^{\circ}23'40''$) and the field of view covers an area of $17' \times 17'$; the source COUP 331 is located at $\alpha = 5^{\text{h}}35^{\text{m}}9.2^{\text{s}}$ and $\delta = -5^{\circ}30'58''$ (cf. Getman et al. 2005). Our analysis is based on the pre-processed photon data provided by the *Chandra* pipeline; for further analysis we applied the CIAO-software in version 3.4. We first screened the photon data for events in the 0.3–13 keV energy band to suppress background. Thereafter, we defined source and background regions as a circle with an 8 arcsec radius and an annulus extending from ≈ 14 –32 arcsec, both centered on the nominal source position.

2.1. The light curve

We generated the background-subtracted 2–9 keV band light curve of COUP 331 shown in Fig. 1. The 6 observation segments can be clearly identified. For most of the COUP observations COUP 331 was recorded at a count rate of 3.3×10^{-3} cts/s, except for two periods. A strong flare (termed “flare I”) occurred ≈ 90 ks after the beginning of the observation. The flare rapidly rises to its peak within ≈ 4 ks, the decay is again quite rapid with an e-folding time of $\tau_{\text{decay}} = 5.2$ ks, but, unfortunately, is only partially observed. A second, less prominent but very significant count rate enhancement (termed “flare II”) occurred 1080 ks after the start of the COUP campaign. This second flare was also not fully covered. Flare II has a much slower rise phase lasting for ≈ 20 ks, and thereafter, the 2–9 keV band count rate remains more or less constant for at least 40 ks when the COUP observations were terminated. For the rest of the observations COUP 331 was found in quiescence.

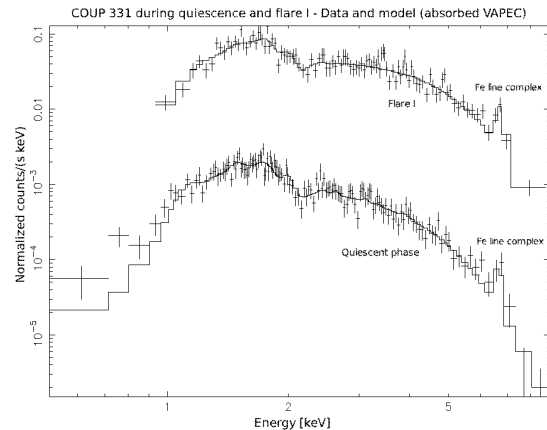


Fig. 2. Spectrum of COUP 331 during flare I (upper curve) and the quiescent phase (lower curve), both fitted with an absorbed VAPEC model.

2.2. Spectral analysis

In the following section we carry out temporally resolved spectral analysis of the flare I, flare II, and quiescent phases of COUP 331; note that all quoted errors refer to 90% confidence intervals unless stated otherwise. COUP 331 is located about 7 arcmin off-axis, hence it does not appear as a perfectly symmetric point-source. However, we regard its image distortion as weak and apply the CIAO standard tools for the extraction of point-source spectra (i.e. *psextract*). The spectra were analyzed using the XSPEC environment in version 11.3.1.

2.2.1. The quiescent phase

The quiescent phase spans the 0–1050 ks time interval with the exception of the first flare event, and is the longest lasting phase, covering $\approx 90\%$ of the total observation time. Note that we disregard a ≈ 20 ks contribution preceding flare II. During quiescence COUP 331 is detected with a net count-rate of 3.3×10^{-3} cts/s corresponding to an (unabsorbed) X-ray luminosity of 1.6×10^{30} erg/s. We checked for temporal changes in the quiescent spectrum, but did not find evidence for any significant variations. The quiescent X-ray spectrum is well described by an absorbed thin-thermal plasma model (we used the VAPEC models) with all metal abundances – apart from Fe, which is left as a free parameter – fixed to 0.3 times the solar values. In Fig. 2 we show the data and the fit; the best fit model parameters are presented in Table 1, where we list the derived absorbing hydrogen column-density, the temperature, the iron abundance and the fit quality.

2.3. Flare I

For an analysis of flare I we considered all data recorded in the time interval from 87.5 to 102 ks; the spectrum of flare I is shown in Fig. 2. The flare spectrum is very well described by the same model as applied for the quiescent phase (cf. Sect. 2.2.1) with somewhat different spectral parameters listed in Table 1. We find – as expected for a flare – an enhanced temperature of 6.8 keV, leading to a spectrum with a clearly detected Fe line feature at 6.7 keV, but with no detected excess emission at 6.4 keV. From the spectrum we derive an (unabsorbed) peak X-ray luminosity of $L_X = 2.6 \times 10^{32}$ erg/s (in the 1–10 keV band) reached directly after the rise phase, and – with an e-folding time of 5.2 ks for the decay phase – a total energy output of

Table 1. Fit parameters for the absorbed VAPEC model.

Phase	n_{H} [10^{22} H/cm 2]	Temp. [keV]	Ab_{Fe} [Ab_{\odot}]	$\chi^2/\text{d.o.f.}$
Quiescent	$1.09^{1.21}_{0.97}$	$3.0^{3.4}_{2.6}$	$0.32^{0.54}_{0.12}$	131.6/134
Flare I	$1.28^{1.41}_{1.18}$	$6.8^{8.2}_{5.5}$	$0.73^{1.02}_{0.46}$	94.2/99
Flare II	$1.55^{1.66}_{1.41}$	≥ 13	$\approx 0.88^a$	102/95

^a This value is ill-constrained since temperature-dependent.

$\Delta E \approx 1.4 \times 10^{36}$ erg in the same band. With these numbers, flare I observed on COUP 331 is among the largest stellar flares ever observed.

2.4. Flare II

For the analysis of flare II we considered all data recorded after 1080 ks (cf. Fig. 1). The X-ray spectrum was generated and analyzed in the same fashion as those of the quiescent and flare I phases. From the spectrum of the entire observed flare II phase (see Fig. 3) we calculate a 1–10 keV band X-ray luminosity of 2.4×10^{31} erg/s. Considering a duration of at least 60 ks, the total energy output in this energy band is $\Delta E > 1.4 \times 10^{36}$ erg.

In the fit process of the flare II data we encountered two problems. First, the absence of temperature-sensitive features in the spectrum – especially the hot Fe XXV feature at 6.7 keV and its Fe XXVI counterpart near 7 keV – prevents us from tightly constraining the plasma temperature. We find that any choice of the temperature beyond 10 keV leads to acceptable fits, and thus decided to apply a value of 13 keV. Second, the spectrum shows definite excess emission above the thermal continuum at 6.4 keV, which we attribute to the Fe I K_{α} line. We therefore included an additional instrumentally broadened Gaussian component centered at 6.4 keV into our model and refitted, leaving only the normalization of the Gaussian component free to vary. The thus obtained fit is shown in Fig. 3, which shows the obvious presence of the 6.4 keV line and virtual absence of the 6.7 keV Fe XXV feature. The resulting fit parameters for the thermal model are again listed in Table 1, and for the Gaussian component we arrive at a normalization of $5(3.3\text{--}6.7) \times 10^{-6}$ ph/(cm 2 s), corresponding to an equivalent width of 685(452–918) eV. As is obvious from Fig. 3, the inclusion of a Gaussian component at 6.4 keV into the model significantly increases the fit quality.

As a first result we thus note that the 6.4 keV emission feature is present – at best – only during 60 ks during flare II. In order to further temporally constrain the presence of the 6.4 keV iron line we constructed a background-subtracted 6.1–6.7 keV narrow-band light curve of COUP 331 with a 4 ks binning in addition to the 2 ks binned 2–9 keV band light curve; both light curves are shown in Fig. 4. As is clear from Fig. 4 the 2–9 keV band light curve stays more or less constant after the rise to peak, while the 6.1–6.7 keV narrow-band light curve decays quite rapidly. We therefore subdivided the flare II phase data into three consecutive 20 ks time intervals, denoted by “rise-phase”, “phase II”, and “phase III” as indicated in Fig. 4. The X-ray spectra in the 5–8 keV region corresponding to these time intervals are shown in Fig. 5. In these plots the solid line indicates the thermal model described earlier. For all spectra the same model was applied, but we allowed the normalizations of the VAPEC and Gaussian component to be fitted independently for all time intervals; all other parameters were regarded globally. Figure 5 clearly demonstrates an evolution of the

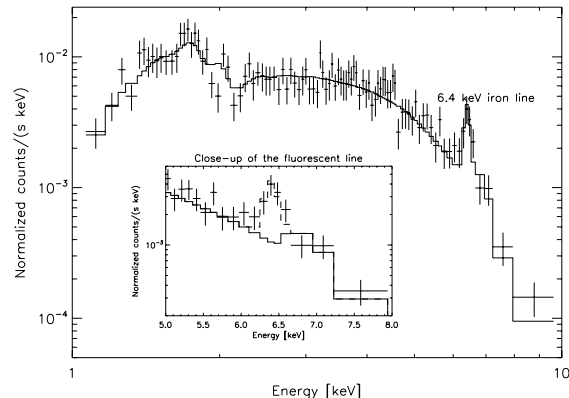


Fig. 3. The COUP 331 spectrum during flare II with a close-up of the 5–8 keV energy band. Two model fits are indicated. First, (solid line) an absorbed thermal model and second (dashed line), the same thermal model with additional instrumentally-broadened Gaussian component centered at 6.4 keV.

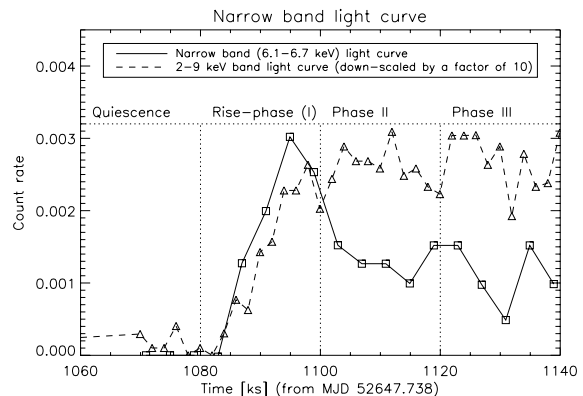


Fig. 4. The background-subtracted narrow-band light curve (solid line) of COUP 331 during the last 80 ks of the COUP observation. The light curve peaks in the rise-phase of flare II. For clarity the 2–9 keV light curve is also shown (dotted line – scaled to fit the plot range).

Fe I K_{α} line strength. Interestingly the line normalization decreases as time proceeds, while the underlying thermal spectrum remains almost unaffected. We thus interpret the variations in the narrow-band light curve shown in Fig. 4 as arising from variations in the Fe I K_{α} feature’s strength. Note that the constancy of the thermal spectrum does not imply the same for the temperature, since the latter exceeds 10 keV, producing a flat spectrum in the “low energy” band we are observing. The K_{α} feature is strongest during the flare II rise phase where our fits yield a line flux of $9.1(5.8\text{--}13.4) \times 10^{-6}$ ph/(cm 2 s) (an EW of ≈ 1400 eV) while in phase II and III it is reduced to $3.04(0.8\text{--}7.6)$ and $0.9(0\text{--}4.8) \times 10^{-6}$ ph/(cm 2 s), respectively. This is also reflected by the narrow-band light curve around 6.4 keV (cf. Fig. 4).

3. Interpretation and conclusions

Our time resolved analysis of the COUP X-ray data of the YSO COUP 331 shows that for $\approx 90\%$ of the entire observation time the object is found in a quiescent state characterized by an X-ray temperature of 30–40 MK. Two major flares are covered by the COUP observation. In the first data segment a relatively short duration event with a peak X-ray luminosity of

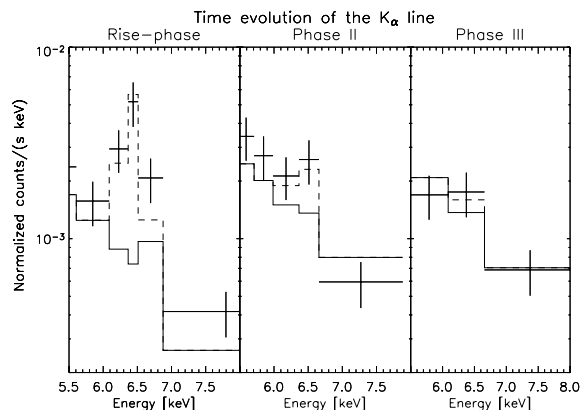


Fig. 5. Time-resolved 5.5–8 keV section of the COUP 331 spectrum (cf. Fig. 4). Note the decrease of the Fe I K_{α} line's strength.

2.6×10^{32} erg/s occurred, which clearly shows the 6.7 keV iron feature, but no Fe I K_{α} emission.

In the last COUP data segment a long duration flare event occurred; starting with a ≈ 20 ks rise phase it lasted >60 ks. The decay of this flare cannot be constrained because the COUP observations were stopped. The total amount of energy released in the 1–10 keV energy band is $>1.4 \times 10^{36}$ erg; the X-ray temperature of this flare is extremely large (≥ 10 keV) and can in fact not be well constrained with the *Chandra* data. A clear and highly significant detection of the fluorescent K_{α} line is obtained only during the 20 ks rise time of this flare; at later times the line may still be present albeit at a lower level. This event on COUP 331 resembles a huge flare observed on Algol, observed by Favata & Schmitt (1999) with BeppoSAX, which also shows a slow rise phase, followed by a nearly constant phase – lasting for ≈ 80 ks – in its 1.6–10 keV band light curve. However, the corresponding 15–100 keV band light curve clearly shows the characteristics of a decay phase (cf., Favata & Schmitt 1999, Figs. 1 and 2). The energy output of 1.4×10^{37} erg derived by Favata & Schmitt (1999) in the 0.1–10 keV band compares well to the numbers estimated for COUP 331, note however that no Fe I K_{α} line was detected.

The precise temporal association between Fe I K_{α} line emission and high energy continuum is necessary in order to quantitatively assess the origin of the Fe I K_{α} emission observed

in COUP 331; we find that the actual photon flux in the fluorescent K_{α} line during the flare II rise phase is 35 times larger than reported by Tsujimoto et al. (2005). This discrepancy arises because Tsujimoto et al. (2005) give time-averaged values, whereas our values refer to several limited time intervals. The X-ray temperature during the flare event was extremely large; the total luminosity in the Fe I K_{α} line alone is $\approx 2.3 \times 10^{30}$ erg/s. While these circumstances appear to favor the excitation of the Fe I K_{α} line through photoionization, preliminary model calculations challenge such a scenario. We repeated the calculations carried out by Bai (1979) applying a reflector with cosmic abundances. We used the same branching ratios and cross sections for iron, but slightly different cross section for absorption by other elements composed according to cosmic abundances. Furthermore, we located the source directly on the reflector to make it subtend half the sky, thus providing an upper limit for the fluorescent iron line flux. The illuminating input spectrum was modeled as a thermal X-ray spectrum with a temperature of 13 keV, normalized to the measured fluxes. Our preliminary calculations show that an already optimally assumed fluorescence geometry significantly underpredicts the observed Fe I K_{α} flux, making an interpretation of the Fe I K_{α} line through photoionization difficult to accept. However, these calculations will be extensively discussed in a larger and systematic context in a forthcoming paper, where we will also address its impact on the characteristics of COUP 331 and other sources with fluorescent K_{α} emission.

Acknowledgements. S.C. acknowledges support from the DLR under grant 50OR0105.

References

- Bai, T. 1979, *Sol. Phys.*, 62, 113
 Fabian, A. C., Rees, M. J., Stella, L., & White, N. E. 1989, *MNRAS*, 238, 729
 Favata, F., & Schmitt, J. H. M. M. 1999, *A&A*, 350, 900
 Favata, F., Micela, G., Silva, B., Sciortino, S., & Tsujimoto, M. 2005, *A&A*, 433, 1047
 Getman, K. V., Flaccomio, E., Broos, P. S., et al. 2005, *ApJS*, 160, 319
 Herbst, W., Bailer-Jones, C. A. L., Mundt, R., Meisenheimer, K., & Wackermann, R. 2002, *A&A*, 396, 513
 Imanishi, K., Koyama, K., & Tsuboi, Y. 2001, *ApJ*, 557, 747
 Neupert, W. M., Gates, W., Swartz, M., & Young, R. 1967, *ApJ*, 149, L79
 Stassun, K. G., Mathieu, R. D., Mazeh, T., & Vrba, F. J. 1999, *AJ*, 117, 2941
 Tanaka, Y., Nandra, K., Fabian, A. C., et al. 1995, *Nature*, 375, 659
 Tsujimoto, M., Feigelson, E. D., Grosso, N., et al. 2005, *ApJS*, 160, 503
 Zarro, D. M., Dennis, B. R., & Slater, G. L. 1992, *ApJ*, 391, 865

Puzzling fluorescent emission from Orion

S. Czesla and J.H.M.M. Schmitt

Hamburger Sternwarte, Universität Hamburg, Gojenbergsweg 112, 21029 Hamburg, Germany

Received 02.04.2010 / accepted 24.06.2010

ABSTRACT

Fluorescent X-ray emission offers one of the rare possibilities to study cool material in the X-ray regime. In the beginning used to analyze the composition of the solar photosphere, the availability of *Chandra* and *XMM-Newton* has made the study of fluorescent emission a major tool for investigating cool material surrounding active, young stars and the inner parts of galactic nuclei. Yet, the question whether photoionization alone is the excitation mechanism of fluorescent X-ray emission or electron collisional excitation also contributes is not completely settled. In this work, we develop a new technique to search for fluorescent emission and analyze its temporal behavior, which we apply to a sample of 106 young, active stars in Orion. Our analysis yields a sample of 23 X-ray sources with fluorescent emission, including 6 objects already reported on in an earlier study. The fluorescent sources show a large variety in their temporal behavior. While the fluorescent emission is associated with soft X-ray flares in some cases, it sometimes appears as a quasi persistent feature, or is seen during bona-fide quiescent periods. We conclude that fluorescent X-ray emission can be observed in a much larger fraction of young, active stars than previously believed. The temporal variability is often hard to reconcile with the photoionization model, which remains, however, plausible if we allow for suitable geometries. It prevails over electron collisional excitation, mainly because the energetics of the latter are physically challenging.

Key words. Stars: activity; Stars: flare; X-rays: stars

1. Introduction

Fluorescent emission pushes the horizon of X-ray astronomy beyond the observation of high energy material, carrying the imprint of cold matter into the X-ray regime. The origin of fluorescent photons is cool, neutral matter pervaded by ionizing photon or particle radiation originating in a nearby high energy source. Following an inner shell ionization in the cold matter, excited ions potentially release their energy in form of fluorescent photons, which convey information on the existence, structure, and composition of their creation site. Geometries appropriate for producing a detectable amount of fluorescent emission are common in a variety of celestial X-ray sources, and fluorescent X-ray emission has been reported in many targets including active galactic nuclei and young stellar objects.

The interaction of an ion with high energy radiation can result in the removal of one of the ion's inner shell electrons. In the context of fluorescent emission, two conceivable mechanisms of K-shell electron removal are at issue: Photoionization by soft X-rays and collisional excitation by electrons with kinetic energy in excess of the K-shell ionization edge. Independent of the interacting particle, an excited ion returns to a lower energy state through a rearrangement of its electron configuration, as a consequence of which the excess energy of the excited state is released by one of two competing processes. Either it is deposited in an "Auger electron", being expelled from the ion, or it is released in the form of a fluorescent photon. The probability of photon emission rises strongly with increasing atomic number (Bambynek et al. 1972) and is termed the "fluorescence yield". Consulting typical solar system or cosmic abundance patterns (e.g., Anders & Grevesse 1989), iron becomes the most promising candidate to search for fluorescent emission. The K-shell ionization energy of neutral iron is 7.112 keV, and the energy of its $K\alpha$ line lies in the X-ray regime at about 6.4 keV; both numbers change slowly with increasing ionization (e.g., Kaastra & Mewe 1993).

Spin-orbit interaction and the effects of photon scattering create a characteristic line profile (e.g., Sunyaev & Churazov 1996), which can, however, hardly be resolved with today's instrumentation in astronomy.

Astronomical detections of the fluorescent $K\alpha$ line of neutral or lowly ionized iron (in the following "Fe $K\alpha$ I line"), were first obtained from solar observations (e.g., Neupert et al. 1967; Doschek et al. 1971), in particular, during solar flares. The question how much photoionization and collisional excitation by electrons contributes to the observed solar fluorescent emission, was addressed by several authors. Parmar et al. (1984) analyze a sample of solar flares and conclude that 'most, if not all,' of the fluorescent X-rays are due to photoionization, and that their results agree well with associated simulations provided by Bai (1979). Even though Zarro et al. (1992) and Emslie et al. (1986) do find evidence for a contribution of fluorescent photons caused by electron collisional excitation during the impulsive phase of individual flares, they also agree that the bulk of the fluorescent emission must be attributed to photoionization. The argument for photoionization as the dominant process is based on the strength or equivalent width of the fluorescent line as well as its temporal relation to the observed hard and soft X-ray flux.

About thirty years after the reports of fluorescent emission in solar X-ray spectra, Tanaka et al. (1995) published their discovery of the Fe $K\alpha$ I line in the spectrum of the active galactic nucleus (AGN) MGC-6-30-15. In excess of an imprint of cold material, this line also carries information on the relativistic space-time structure at its origin, providing a deep insight into the inner parts of an AGN. Ballantyne & Fabian (2003) argue that also in AGN sources photoionization largely dominates over electron or proton collisional excitation. The discovery of Tanaka et al. sparked an intensification of the search for the Fe $K\alpha$ I line in X-ray sources, in the wake of which fluorescent emission was also discovered in several stellar sources other than the Sun.

Stellar sources with reported fluorescent emission include YLWA 16 (Imanishi et al. 2001) with a Fe K_{α} I line detection during a flare, HR 9024 for which Testa et al. (2008) present evidence for the Fe K_{α} I line in a *Chandra* High Energy Transmission Grating spectrum, and Elias 29, which shows a fluorescent line of variable strength (Giardino et al. 2007). With the exception of HR 9024, the above stars are young stellar objects (YSOs). While photoionization remains the most common explanation for the origin of the fluorescent photons, Giardino et al. (2007) argue that the characteristics of the fluorescent emission observed from Elias 29 are hard to reconcile with the predictions of the photoionization scenario and suggest a nonthermal electron population invisible in soft X-rays as a possible explanation for their findings.

As young stellar sources are known to possess large amounts of cold circumstellar material in the form of disks or envelopes, it seems reasonable to search for the Fe K_{α} I line in star forming regions. The Orion Nebula is a center of recent and still ongoing star formation, harboring a wealth of young stellar objects in various evolutionary states. Orion was also the target of a long *Chandra* observation known as the “*Chandra* Orion Ultradeep Project” (COUP) (e.g., Getman et al. 2005). Tsujimoto et al. (2005) carried out a search for the Fe K_{α} I line in the COUP data and presented a sample of seven COUP sources with a fluorescent Fe K_{α} I line detection. One of their sources was further analyzed by Czesla & Schmitt (2007), who reported the temporal concentration of the observed Fe K_{α} I line flux in the rise phase of one of two flares.

In this study we reanalyze the X-ray data of 106 COUP sources, including the sample presented by Tsujimoto et al. (2005). We systematically search for fluorescent Fe K_{α} I line emission and present an analysis emphasizing its temporal evolution. Therefore, we first introduce a method for obtaining the light curve of the Fe K_{α} I line feature and discuss its significance as obtained from spectral fitting. We then proceed with an analysis of the Fe K_{α} I line behavior in the Tsujimoto et al. (2005) sources and some additional sources with fluorescent emission. Finally, we discuss the impact of our findings on the commonly accepted photoionization model of fluorescent emission and its alternatives.

2. On the detection and analysis of transient spectral features

Longer integration times lead to the accumulation of signal, allowing for better constrained results unless transient features are under consideration, which are flattened out during longer integrations.

Inspired by the problem of analyzing the behavior of the fluorescent Fe K_{α} I line (Czesla & Schmitt 2007), we present a systematic method to detect transient spectral features and analyze their temporal variability, often with a higher resolution than allowed for by pure spectral analysis. In the following we apply the relations between several narrow-band light curves to derive the “light curve” of a particular spectral feature.

2.1. The “line light curve (LLC)” method

Assume we are given a spectrum with an overall shape well described by some model, M , and, further, that the overall spectral shape (but not necessarily its normalization) varies only slowly with respect to the temporal resolution of the feature under scrutiny. Our model is supposed to describe the observed

spectrum, i.e., it already accounts for our instrument. Below, we assume a thermal model, M_{th} , with an additional emission line, which is, however, not a necessary precondition.

Let the emission line have a central energy of ϵ_e , and we are interested in its temporal behavior. The line, which may be broadened by whatever effects, shall be fully comprised by the “emission band” $I_e = [\epsilon_e - \delta\epsilon_1, \epsilon_e + \delta\epsilon_2]$. The number, N_e , of photons expected within this band is given by the sum of the thermal contribution, $N_{th,e}$, given by M_{th} and the line contribution, N_{line} , so that

$$N_e = N_{line} + N_{th,e} . \quad (1)$$

Now we choose a “comparison band”, $I_c = [\epsilon_{c1}, \epsilon_{c2}]$, which comprises only continuum emission. In I_c the thermal component provides $N_{th,c}$ photons, again determined by M_{th} . Defining the “continuum ratio”, r_c , such that

$$N_{th,c} = r_c \cdot N_{th,e} \quad (2)$$

we obtain the number of expected line photons by

$$N_{line} = N_e - \frac{N_{th,c}}{r_c} . \quad (3)$$

For a given energy interval and model, the continuum ratio, r_c , is uniquely defined. Narrow-band light curves corresponding to the emission and comparison bands provide both photon numbers on the right hand side of Eq. 3 (N_e and $N_{th,c}$), and, consequently, the left hand side of Eq. 3 equates to the line strength as a function of time.

Accordingly, we define the “line light curve (LLC)” as a sequence of pairs, $\{t_i, llc_i\}$, where llc_i denotes the quantity

$$llc_i = N_{e,i} - \frac{N_{th,c,i}}{r_{c,j}} , \quad (4)$$

which is basically the number of excess photons in the i^{th} time-bin (cf. Eq. 3) and t_i represents the associated time stamp. An extra index, j , attached to r_c accounts for those cases where a single value of the continuum ratio is insufficient.

An integration of the LLC over a time span yields a measure of excess emission observed within this span. Formally, we define the “cumulative LLC” (CLLC) as

$$c llc_n = \sum_{j=j_0}^{j_0+n} llc_j . \quad (5)$$

With no excess emission the expectation value of $c llc_n$ is zero by definition; but what is its distribution? As the values of the summands are statistically determined, the problem of finding the distribution of $c llc_n$ compares to finding the end-point distribution of a random walk. By definition the quantity $N_{e,i}$ (see Eq.4) obeys a Poisson distribution with an expectation value of μ_i . If we assume that the quantity $N_{th,c,i}/r_{c,j}$ can be measured very accurately, so that its distribution is adequately approximated by a δ -peak, $dP(N_{th,c,i}/r_c) = \delta(N_{th,c,i}/r_c - \mu_i) d(N_{th,c,i}/r_c)$ (a justified simplification when r_c is sufficiently large), the distribution in the individual bins, llc_i , of the LLC becomes

$$P(llc_i) = \text{Poisson}(\mu = \mu_i, llc_i + \mu_i) , \quad (6)$$

which is effectively a shifted Poisson distribution with a variance of μ_i , but a mean of zero due to the shift, where llc_i may take values in the interval $[-\mu_i, \infty)$.

Equation 6 indicates that the cumulated LLC, $c llc_n$, is a sum of Poisson distributed quantities and, hence, Poisson distributed

(but shifted) itself. Consequently, the standard deviation of $cIlc_n$ becomes

$$\sigma(cIlc_n) = \sqrt{\sum_{i=1}^n \mu_i}. \quad (7)$$

This quantity yields an approximation to the expected width of the end-point distribution of the random walk defined by the numbers obtained from Eq. 5 increasing the upper summation boundary, n , step by step.

Combining the estimate of the line strength with that of the underlying continuum, we can also derive an estimate of the EW, which is given by

$$\text{EW [emission band width]} = \frac{N_e - N_{th}/r_c}{N_{th}/r_c} = r_c \frac{N_e}{N_{th}} - 1. \quad (8)$$

2.2. The choice of the energy intervals

For any application of the above method, appropriate emission and comparison energy bands must be found. In the specific case of the fluorescent Fe K $_{\alpha}$ I line centered at 6.4 keV, we argue in favor of the following intervals.

For the emission interval it is convenient to apply $I_e = [6.2 \text{ keV}, 6.5 \text{ keV}]$, which, at the spectral resolution provided by the *Chandra* ACIS and XMM-*Newton* EPIC instruments, contains $\approx 80\%$ of all Fe K $_{\alpha}$ I line photons. Unfortunately, the “iron line complex”, a number of lines pertaining to Fe XXV and other high ionization stages of iron, is located close to the high energy boundary of the emission band at about 6.7 keV. To avoid contamination, an asymmetric band with respect to the Fe K $_{\alpha}$ I line center was chosen.

For the comparison interval, I_c , we use an energy band extending from 6.2 keV to lower energy. Compared to an interval beyond 6.5 keV, typical stellar X-ray spectra provide more photons at lower energies, the detectors on-board *Chandra* and XMM-*Newton* are more sensitive here, and, finally, no prominent lines are located there. In practice we use 5.2 keV as a lower boundary for the comparison interval.

2.3. The dependences of the continuum ratio on spectral parameters

At the heart of the LLC approach is the subtraction of the continuum contribution underlying a spectral feature. The continuum has to be extrapolated (or maybe interpolated) from another part of the spectrum, and the “predictor” of its contribution is the continuum ratio, r_c . As we are concerned with thermal spectra, a major issue to be addressed is the temperature dependence of r_c . Source temperatures do not remain perfectly constant, and we are not able to determine them with arbitrary accuracy. Therefore, it is essential to show that small variations in temperature do not have a serious impact on the continuum ratio.

In Fig. 1 we show the continuum ratio for a wide range of temperatures. The solid and dashed lines indicate the ratio as obtained with and without considering the effect of a varying effective area. In the example we use 6.2 – 6.5 keV and 5.2 – 6.2 keV as the boundaries of the emission and comparison bands, and the effective area is modeled with a linear dependence on energy; we use $A_{eff} [\text{cm}^2] = 1000 \text{ cm}^2 - 100 \text{ cm}^2/\text{keV} \cdot \epsilon [\text{keV}]$, which in the energy range under consideration, is quite representative of numbers obtained for *Chandra* and XMM-*Newton*.

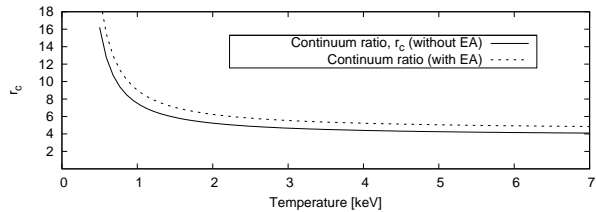


Fig. 1. The continuum ratio, r_c , as a function of temperature.

Clearly, r_c varies quickly for temperatures below $\approx 2 \text{ keV}$ and then approaches an almost constant value. When the effective area effect is taken into account, the ratio increases as more photons are detected where the effective area is larger, but the overall behavior remains unaffected. We conclude that r_c is robust against small (and even large) temperature variations for temperatures beyond 2 keV.

3. Spectral binning and the fit statistics

We are concerned with an individual feature at a well known energy. Therefore, we can adapt our binning approach to meet our purpose best. In particular, we are interested in the narrow Fe K $_{\alpha}$ I emission line at 6.4 keV. In view of that, we use a fixed bin-size of $\approx 100 \text{ eV}$ (actually 7 *Chandra* channels which is a little more than 100 eV) chosen so that one bin is centered on the Fe K $_{\alpha}$ I line energy. For spectral fitting we use the C-statistics (Cash 1979), which can handle low photon numbers per bin, but provides no goodness of fit indicator such as χ^2 does.

3.1. The significance of a spectral emission line

The test for the existence of a spectral line belongs to a category of statistical problems frequently encountered in X-ray astronomy: hypothesis testing in the case of nested models. For a given data set, D , we define two alternative models, $m_1(\theta_1)$ and $m_2(\theta_2)$, specified by their parameter vectors θ_1 and θ_2 with n_1 and n_2 free parameters. Let $n_2 > n_1$ and m_1 be a subset of m_2 , so that m_1 is nested within m_2 . The problem consists in deciding which of the models is to be preferred.

In our particular case, m_1 is a thermal model and m_2 is the same thermal model extended by a narrow Gaussian line at a fixed energy of 6.4 keV. As a measure of the “quality” with which a given parameter vector, $\theta_{1,2}$, reproduces the data, we use the likelihood statistics.

The maximum likelihood achieved with m_1 is \mathcal{L}_1 , and the fit with the additional narrow spectral line at 6.4 keV provides another likelihood \mathcal{L}_2 . As m_1 is nested within m_2 , the introduction of the additional component cannot worsen the fit result. A popular tool for finding the preferred model is the likelihood-ratio-test (LRT). Protassov et al. (2002), however, point out that this test, while being applicable in a variety of other cases, fails in this particular situation, basically because the topology of the underlying parameter space does not fulfill the requirements demanded by the test.

In the case of a narrow emission line the difference in the dimensions of the parameter spaces ($n_2 - n_1$) before and after the introduction of the line is one, and with an appropriate (valid) parameter space, the LRT test statistics, $-2 \log(\mathcal{L}_1/\mathcal{L}_2)$, follows a χ^2 distribution with a single degree of freedom. This is not the case here. A deficit that cannot be cured by more signal or better instruments, but is inherent in the mathematical structure of the

test. Protassov et al. (2002) carried out Monte-Carlo calculations (c.f. their Sect. 3.2) and found that in the case of a narrow emission line the false-positive rate is considerably overestimated by the χ^2 distribution. At the nominal 5% cut-off of the χ^2 distribution the “true” (simulated) value is only 2.6%.

To “calibrate” (cf., Protassov et al. 2002) the LRT statistics for this particular case, we consider the following argument: Assume we are given a continuum model and a narrow line at fixed energy, which may either appear as an emission or an absorption line. In this case, the quantity $-2 \log(\mathcal{L}_1/\mathcal{L}_2)$ should, indeed, follow the χ^2_1 distribution. If we now only allow for one of the possibilities, i.e. either emission or absorption, the introduction of the line will not result in any enhancement in the fit statistics where the other possibility is needed. In those cases we obtain $-2 \log(\mathcal{L}_1/\mathcal{L}_2) = 0$. How often this occurs, depends on the form of the distribution underlying the data, which, in our case, is the Poisson distribution. As this distribution is approximately symmetrical around its expectation value, μ , at least for $\mu > 1$, about half of the line fits should result in $-2 \log(\mathcal{L}_1/\mathcal{L}_2) = 0$. In spite of this, the distribution of the likelihood ratio for the emission components remains unaffected if it is present.

Following this argument the probability of obtaining a value of the LRT statistics, $lrt = -2 \log(\mathcal{L}_1/\mathcal{L}_2)$, in the interval $[lrt, lrt + d(lrt)]$ is given by

$$dP(lrt) = \frac{1}{2} (\delta(lrt) + \chi^2_1(lrt)) d(lrt), \quad (9)$$

where $\delta(lrt)$ denotes the δ -distribution. As described above half of the distribution “is glued to 0” and the other half follows a χ^2_1 distribution.

To corroborate the validity of our reasoning, we carried out Monte Carlo simulations similar to those of Protassov et al. (2002). We simulate a number of observations using a constant continuum model and Poisson statistics. First, we fit the normalization yielding a likelihood of \mathcal{L}_1 , and, second, we fit both the continuum normalization and the line normalization simultaneously to the same observation. For every simulated observation, we record the value of the LRT statistics, $-2 \log(\mathcal{L}_1/\mathcal{L}_2)$.

The results of the Monte Carlo simulations with a continuum expectation value of 2 photons per bin are shown in Fig. 2. Clearly, the nominal χ^2 distribution with a single degree of freedom fails to reproduce the simulated findings, whereas the distribution given in Eq. 9 provides a considerably better approximation.

Therefore, when testing for the presence of a narrow emission line, we can interpret the numbers obtained for the LRT statistics using Eq. 9 as a reference distribution. In practice, this means that our sensitivity is approximately twice as high as a blind application of the LRT implies.

3.2. Significance estimates in time-resolved spectroscopy

Let us assume an observation of length T to be at our disposal, and in the data we detect a source, which is only slightly variable on the time scale T . Further, we choose an arbitrary time interval of length t so that $t \ll T$ and carry out a spectral analysis, using only the data pertaining to that sub-interval. Our analysis leaves us with an emission line, to which we can assign a high probability, p_e , for being set apart from the noise along the lines of the LRT presented in the previous section. Now we ask for the probability to find an emission line with the same significance in any of the time intervals of length t – let there be an integer number

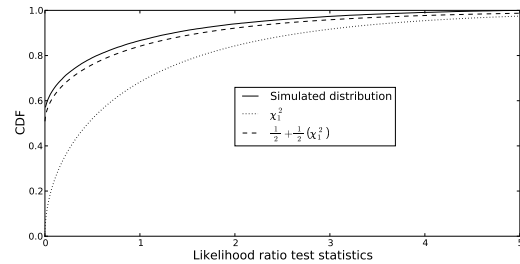


Fig. 2. Distribution of the LRT statistics obtained from Monte Carlo simulations (solid line), the nominal χ^2_1 distribution (dotted), and the distribution given in Eq. 9 (dashed).

$N \approx T/t$ – contained in our observation under the assumption that no emission line is present.

This set-up can be interpreted as a “Bernoulli experiment” with its probability of success given by the probability for a spurious detection, $1 - p_e$. Therefore, the chance, p_s , to obtain one (or more) such emission line(s) from the analysis of any of the N subintervals by pure chance amounts to

$$p_s = 1 - p_e^N, \quad (10)$$

which must be interpreted as the “true” significance of our detection.

The main restriction above is that the source may only be slightly variable. While this assumption is essential for the interpretation as a Bernoulli experiment, it is known to be invalid for many X-ray sources. For example a strong flare may provide the majority of the source photons and also Fe K_α I line photons, while being short. In such a case, Eq. 10 does no longer provide a meaningful estimate of the significance. To obtain a meaningful number in these cases, we propose to use $N = N_{tot}/N_{int}$ in Eq. 10, where N_{tot} is the total number of observed source photons in an appropriate band and N_{int} is the number of photons in the interval under consideration.

If the source is constant both approaches are equivalent and mathematically correct. In the case of a variable source, none of the above approaches is strictly correct. Nonetheless, we use Eq. 10 to obtain significance estimators, accounting for the choice of a particular fraction of the data.

4. Data analysis

The Orion Nebular Cloud is among the best studied star forming regions. In particular, it was the target of a large *Chandra* program aimed at uncovering the X-ray properties of young stars – the *Chandra* Orion Ultra Deep Project (COUP). The COUP campaign consists of six consecutive observations of Orion providing a total observation time of ≈ 840 ks distributed over nearly 13 days, which corresponds to a time coverage fraction of $\approx 75\%$.

In Table 1 we summarize the basic information on the COUP observations and refer the reader to Getman et al. (2005) for a more detailed discussion. Note that the last column in Table 1 gives the identifier we use throughout this work to refer to the individual observations.

4.1. Defining the search sample

The entire COUP source sample comprises 1616 X-ray sources (Getman et al. 2005). From these sources, we extract a subsam-

Table 1. The COUP observations.

Obs. ID	Start [ks] ^a	Length [ks]	Identifier
4395	0	100	O1
3744	156	164	O2
4373	384	172	O3
4374	616	169	O4
4396	841	165	O5
3498	1070	69	O6

^a Counted from MJD 52647.9.

ple used in our search for the fluorescent Fe K_{α} I line. Since the line has a fixed energy of 6.4 keV, it is advisable to include only those sources, which show a sufficient number of counts in an appropriate energy interval around 6.4 keV.

In our analysis we use only sources with more than 30 counts in the “emission-band” (6.2 – 6.5 keV). In particular, we iterated through the sources presented by Getman et al. (2005), extracted the source counts in the emission band, corrected them for the PSF coverage of our extraction region, and included the source when our search criterion was matched.

For the weakest source included in the sample of Tsujimoto et al. (2005) (COUP 649), we find 31 emission band photons, making our sample include the Tsujimoto et al. sources as a sub-sample.

Our final sample comprises a total of 108 COUP sources, which provide the most promising candidates for our search for fluorescent emission. For our purpose, COUP 123 and COUP 124 collapse into a single source, because they are either too close to be resolved (1.4 arcsec, \approx 5 arcmin off-axis), or a single source. Their spectrum is appropriately described by a single temperature thermal model.

Additionally, we had to exclude COUP 90 and COUP 828 from our sample, because they are located on chip edges, which prevented us from obtaining appropriate spectra (CIAO 4.1), so that the sample size reduces to 106 COUP sources.

4.2. Extraction regions and pile-up

For most of our sources we use circular extraction regions covering the entire source. Our search sample necessarily contains the most X-ray luminous sources in the COUP field, which may suffer from severe pile-up. To avoid a strong pile-up effect, we use annulus shaped extraction regions in 29 cases. Whether pile-up becomes severe depends not only on the source count rate, but also on its temporal behavior and positioning on the detector. We chose the annulus parameters in accordance with these considerations, and note whenever an annulus shaped region was used for extraction.

4.3. A standard analysis

Our search sample consists of 106 sources. To achieve a homogeneous scan for the fluorescent Fe K_{α} I line, they should be treated using standard criteria, eliminating biases arising from individual, subjective choices during the analysis.

4.3.1. Bayesian block analysis of the broad-band light curves

A key ingredient in the LLC method is the determination of the correct continuum ratio. The observed count rate for individual X-ray sources can vary by orders of magnitude during the

COUP campaign. Although the continuum ratio is relatively robust against temperature variations (see Sec. 2.3), it is advisable to distinguish between periods of different count rate regimes, possibly indicating different source spectra and continuum ratios. Of course a transition between different spectra may not always be accompanied by a count rate change, but we neglect this possibility here.

Our count rate analysis is based on the broad-band (2–9 keV) light curve. To separate the entire campaign data of individual sources into intervals with comparable count rate, we apply the concept of “Bayesian blocks” elaborated by Scargle (1998). The method of Bayesian blocks ‘converts raw photon counts into the most probable piecewise constant representation of brightness as a function of time’ (Scargle 1998).

We apply an iterative algorithm to find individual change points in the light curves. This, according to Scargle (1998), does not represent the exact mathematical treatment of the problem, but, nonetheless, yields comparable results. As was pointed out by Scargle, an appropriate condition must be found to stop the iteration before segmenting the data set excessively. Instead of applying the Bayes factor (Eq. 48 in Scargle 1998) and a prior, we use the likelihood ratio, which can be easily calculated, to decide whether to introduce a change point or not.

As the continuum ratio depends only weakly on the spectral temperature, we aim at a coarse segmentation of the light curves in order to separate periods between which the spectrum of the associated source may significantly differ and with it the continuum ratio. To introduce a change point, we demand no less than 100 counts per block, a minimum block length of 20 ks, and a value of the LRT statistics larger than 100.

With this method we separate the 106 source light curves into 419 intervals of comparable count rate, and proceed by generating spectra for every individual source and block, which can be used to determine the corresponding continuum ratio.

4.3.2. Automated model fits

For our analysis we use both thermal as well as power law models, for which we set up automated fit procedures using XSPEC.

The fits of the thermal model are based on the 0.3 – 9 keV energy band. As a basis for our fits, we use an absorbed two-temperature APEC (e.g. Smith et al. 2001) model extended by an emission line representing the fluorescent Fe K_{α} I line at 6.4 keV. Additionally, we allow for emission lines at various other energies, which are later used to substantiate our results. The nominal intrinsic width of all lines is 0 eV. All element abundances but that of iron are treated as a single fit parameter, which is also shared among the two thermal components. In contrast, the iron abundance represents an independent fit parameter in both thermal components.

Starting a fit process with unfavorable initial conditions can easily lead to unphysical results, even if the fit converges appropriately. Therefore, the process must be set up carefully to avoid converging to unrealistic solutions.

Our approach is the following: We start using only one of the two available thermal components and then add in the second. If the enhancement in C-statistics exceeds 6.4 by introducing the later component, this solution is kept, otherwise the one temperature solution is used. The value of 6.4 corresponds to the 90% cut-off in a likelihood ratio test comparing models which differ by 3 degrees of freedom, which are temperature, iron abundance, and normalization here. We note that the numerical equality with the fluorescent line energy is purely accidental.

Furthermore, we apply a number of restrictions to the temperatures and abundances to avoid unphysical solutions. If the temperature of any thermal component exceeds 8 keV, we fix it at 8 keV and reiterate the fit, because temperatures beyond this limit can hardly be resolved in *Chandra* ACIS I spectra. If one of the iron abundances exceeds 10 times the solar value, it is fixed to the value of the global abundance pattern, because it is usually not well constrained in this case. Similarly, the global abundances are fixed at solar values, if the fit result is found to exceed 10 times the solar value.

After an acceptable solution is found, we obtain fluxes and equivalent widths for the fluorescent line and the comparison line on the basis of these fits. Finally, the fits are used to derive the continuum ratio for the Bayesian block under consideration. In this vein, effective area and absorption are automatically accounted for in its derivation.

To complement the results of the thermal model, we also adapt an absorbed power law model using only the high energy tail (3 – 9 keV band) of the spectra. This model is extended by narrow emission lines accounting for the Fe K $_{\alpha}$ I line at 6.4 keV and the hot iron line complex at 6.7 keV.

The results of these fits are particularly interesting as they yield the EW of the hot iron line complex, and they provide means to check whether the adaption of the thermal model failed.

4.3.3. Line light curve analysis

As soon as the continuum ratios are determined, the LLC and CLLC can be calculated. According to our reasoning, periods of bona fide fluorescent emission are characterized by an increase in the CLLC. Taking an impartial position, the morphology of the increase is unknown. Neither can we say on what time scales the CLLC typically evolves, nor can we say whether the rise is continuous or not, or whether it is correlated with the soft X-ray continuum.

In our search for candidate intervals, we first exclude those sources, which do not show a CLLC excess larger than the expected one (cf. Eq. 7). For each remaining source, we search all conceivable connected intervals longer than 20 ks for the largest relative excess in fluorescent photons. About 4 000 of such intervals can be constructed considering that we have 89 bins of ≈ 10 ks length each. For each of these conceivable intervals, we calculate the quantity N_{σ} defined by

$$N_{\sigma} = \frac{\sum_i LLC_i}{\sqrt{\sum_i \frac{N_c(\Delta t)_i}{r_{c,i}}}} \quad (11)$$

where i is an index running over all light curve bins in the interval, N_c is the observed rate of comparison band photons, r_c the continuum ratio, and Δt is the duration of the individual bins. As an additional constraint, we demand that each interval to be considered must at least comprise 5 CLLC excess photons and ≥ 50 comparison band photons to be relevant.

The most promising candidate interval is that with the highest N_{σ} value. Yet, as every source will contain one such interval, we have to choose a reasonable limit for N_{σ} ; only beyond this limit intervals shall be considered valid candidate intervals. Replacing the Poisson distributions by normal distributions, it may be shown that N_{σ} approximately follows a standard normal distribution. Therefore, the probability that $\max(N_{\sigma})$ exceeds a limit, L , becomes

$$p(\max(N_{\sigma}) > L) = 1 - \text{Normal}_{0,1}(N_{\sigma} < L)^n, \quad (12)$$

where n is the number of intervals for which N_{σ} is determined and $\text{Normal}_{0,1}$ denotes the standard normal distribution. If, as in our case, n is ≈ 4000 and we demand $p(\max(N_{\sigma}) > L) = 0.2$, we obtain $L \approx 3.9$, which is considered a reasonable limit for N_{σ} . The preceding approximation does not take into account, that most intervals overlap and are, therefore, not independent, and it also neglects, that some may not contain enough photons to be relevant. To overcome these shortcomings, we obtain a more appropriate limit by a Monte Carlo simulation. For each source, we simulate a number of light curves based on Poisson statistic with the observation as our expectation value. From these artificial light curves a distribution of $\max(N_{\sigma})$ can be derived, which takes into account all constraints. We note, however, that the thus obtained results are in good agreement with the approximation.

Following the above stated approach, we find candidate intervals in 25 of our sample sources, and we proceed by extracting the associated spectra. We then apply the same automated thermal fits as above to find a spectral model. On the basis of this model, we calculate the significance of the fluorescent Fe K $_{\alpha}$ I line in the interval using Eq. 9 and apply Eq. 10 to account for our interval choice. We evaluate Eq. 10 using both definitions of the number of repetitions in the Bernoulli experiment, i.e., interval length and the number of enclosed photons. The maximum of both results is used as a significance estimator. We prefer the maximum to the more conservative minimum here, because latter would necessarily underestimate the significance during a flare, which is typically short but intense. We also note that the application of Eq. 10 is no longer fully justified here, because the “experiments” are not fully independent when a distinguished interval is chosen in advance. Nonetheless, the number is used as an estimate.

In Table 2 we list those sources with a line detection at a significance level of $\geq 95\%$. Our sample comprises 23 sources including 6 sources already reported on by Tsujimoto et al. (2005). Note that we excluded COUP 554 from the list, because a correct analysis of this source was impeded by pile-up. Consulting the 95% limit, we estimate that 1 – 2 detection given in Table 2 must be attributed to noise. Taking into account the difficulties in defining the true significance of the Fe K $_{\alpha}$ I line in this temporally resolved analysis, we note that also accepting 3–4 spurious detections, does not seriously alter the outcome of the analysis.

5. Discussion

This section starts with a presentation of individual sources, proceeds with an analysis of several sample properties, and, finally, closes with a discussion dedicated to the physical scenario of Fe K $_{\alpha}$ I line creation in the light of our results.

5.1. Previously known COUP sources with fluorescent emission

Tsujimoto et al. (2005) present a sample of 7 COUP sources (COUP sequence nos. 331, 561, 621, 647, 649, 1030, and 1040) with a detection of fluorescent emission. The authors, however, did not carry out time-resolved spectroscopy, but use time-averaged spectra. Below we present the outcomes obtained for the Tsujimoto et al. sources to demonstrate the techniques developed so far.

In the following values given in parentheses refer to the 90% confidence range for the given parameter.

Table 2. Most promising intervals for fluorescent emission and basic fit results.

COUP ^{a b} seq. no.	N_σ	Interval [ks]	Sign. [%]	Fe K_α I EW [eV]	$N_{6.4\text{keV}}$ [10^{-7} ph/(cm ² s)]	N_H [10^{22} H/cm ²]	T_1 [keV]	T_2 [keV]
7	3.95	60-961	99.99	446(216-667)	2.48(1.20-3.71)	0.02(0.01-0.03)	2.08(1.97-2.34)	0.83(0.81-0.85)
9	3.86	514-851	99.35	366(123-628)	7.95(2.67-13.63)	0.19(0.15-0.22)	3.72(3.12-5.14)	1.00(0.89-1.07)
245 ^a	5.32	80-891	99.98	482(261-906)	1.90(1.03-3.57)	0.16(0.10-0.20)	4.51(3.60-8.23)	0.84(0.77-1.00)
267	4.81	30-196	99.88	400(176-672)	13.02(5.73-21.88)	2.42(2.15-2.61)	8.00	-
331 ^b	6.92	1080-1110	100	1437(959-1927)	78.9(52.7-105.8)	1.79(1.60-2.00)	8.00	-
449	3.67	296-961	98.69	212(60-391)	1.62(0.46-2.98)	1.53(1.29-1.76)	2.87(2.41-3.47)	0.98(0.76-1.13)
561 ^b	4.64	100-414	99.98	569(279-914)	4.60(2.25-7.38)	0.98(0.90-1.07)	2.40(2.20-2.64)	-
599	4.65	10-1080	99.99	448(216-663)	2.07(1.00-3.06)	7.64(6.65-8.75)	3.67(2.86-4.89)	-
621 ^b	6.21	10-296	99.97	602(307-973)	4.84(2.47-7.83)	4.54(4.29-5.24)	3.25(2.64-4.98)	0.08(0.00-0.09)
647 ^b	4.22	50-626	99.85	440(194-767)	3.42(1.51-5.96)	25.23(20.33-31.63)	5.87(3.69-9.32)	-
662	4.09	246-394	98.35	206(93-434)	12.61(5.70-26.57)	16.06(14.40-17.88)	8.00	0.08(0.00-0.11)
669	4.39	384-776	99.88	384(160-616)	2.73(1.14-4.38)	0.33(0.29-0.36)	8.00	1.02(0.95-1.06)
680	4.21	80-716	99.94	410(190-689)	2.25(1.04-3.77)	11.63(9.68-13.41)	8.00	0.08(0.00-0.09)
682	3.53	851-1130	98.62	312(108-591)	3.01(1.04-5.71)	1.52(1.22-1.76)	3.05(2.71-3.71)	0.09(0.00-0.11)
797 ^a	3.26	20-951	96.85	82(11-151)	3.28(0.45-6.08)	29.04(27.23-30.92)	8.00	-
801	4.79	166-636	99.54	456(163-785)	5.91(2.11-10.20)	0.41(0.36-0.48)	3.08(2.40-4.25)	1.04(0.89-1.23)
942	3.90	286-716	99.99	308(173-506)	4.68(2.62-7.69)	1.08(0.99-1.15)	3.44(3.16-3.87)	-
1030 ^{a,b}	3.17	206-716	99.68	143(56-231)	6.35(2.50-10.25)	16.14(13.85-18.68)	8.00	0.28(0.22-0.33)
1035	4.09	394-686	98.26	410(153-851)	2.78(1.04-5.77)	1.76(1.59-2.02)	2.24(1.92-2.53)	-
1040 ^b	3.80	266-544	98.62	307(110-664)	3.14(1.12-6.78)	1.44(1.29-1.60)	2.95(2.58-3.46)	-
1080	4.35	766-961	98.58	332(107-578)	6.99(2.26-12.19)	2.35(1.95-2.86)	3.28(2.68-3.86)	0.63(0.00-0.88)
1380	3.95	554-786	96.37	187(49-336)	5.68(1.49-10.21)	0.51(0.45-0.59)	8.00	1.15(0.93-1.47)
1499	4.50	384-524	99.69	372(145-631)	7.25(2.83-12.30)	0.43(0.37-0.49)	4.56(3.88-5.40)	-

^a Annulus shaped source region.^b Sources present in the sample of Tsujimoto et al. (2005).

5.1.1. COUP 331 - V 1486 Ori

This source was already discussed in detail in a previous publication by Czesla & Schmitt (2007). V 1486 Ori shows two major flare events during the COUP campaign. The first, rather short one, takes place towards the end of O1 (“Flare I” in Czesla & Schmitt 2007); no significant fluorescent Fe K_α I line emission was detected here.

In Fig. 3 (panel A) we show the broad-band light curve, the change points returned by the Bayesian analysis, and the resulting CLLC. The first flare is not accompanied by a considerable excess in the CLLC. The spectrum is well fitted by an absorbed thermal model with a strong (hot) iron line complex at ≈ 6.7 keV.

The CLLC clearly indicates that the fluorescent Fe K_α I line emission is present during the rise-phase of a second, more violent flare ignited during O6, which is in line with previous findings (Czesla & Schmitt 2007). The automated search for intervals with fluorescent Fe K_α I emission returned the 1080 – 1110 ks period (cf. Table 2) as the most promising candidate interval. In Fig. 4 we present the LLC and the spectrum for the corresponding part of the observation. The LLC clearly shows the concentration of Fe K_α I line emission in the rise phase of the flare, and the spectral analysis yields an EW of 1440(960 – 1930) eV for the line.

The measured EW of this Fe K_α I line exceeds typical model predictions (see Sect. 6) by an order of magnitude, and it is, thus, particularly interesting. A more detailed discussion about the origin of this Fe K_α I line is given later in Sect. 6.3.

5.1.2. COUP 561

Figure 3 (B) shows the results of our light curve analysis for COUP 561. The CLLC shows two phases of increase. During the second COUP observation, as in the longest part of the COUP

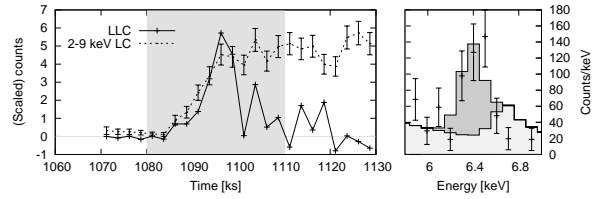


Fig. 4. Left: LLC and (scaled) broad-band light curve (2.5 ks binning) for COUP 331 (O6). Right: Excerpt of the spectrum (corresponding to the gray shaded time span in the left panel). Both a model with and without extra line emission are indicated.

campaign, COUP 561 is encountered in a quiescent state to judge from the BBLC. Nonetheless, the CLLC indicates about 10 excess photons in the emission band.

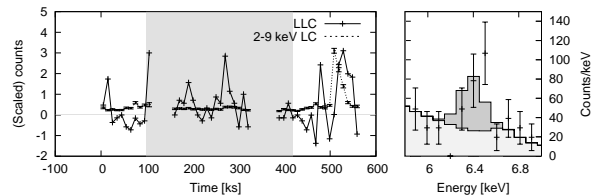


Fig. 5. Left panel: The LLC and the broad-band light curve (both 10 ks binning) of COUP 561. Latter scaled to show the same maximal count rate as the LLC. The gray shaded area denotes the time span for which an excerpt of the spectrum is shown in the right panel. There we show the X-ray spectrum around 6.4 keV and indicate both a thermal model with and without excess emission at the energy of the fluorescent Fe K_α I line.

S. Czesla and J.H.M.M. Schmitt: Puzzling fluorescent emission from Orion

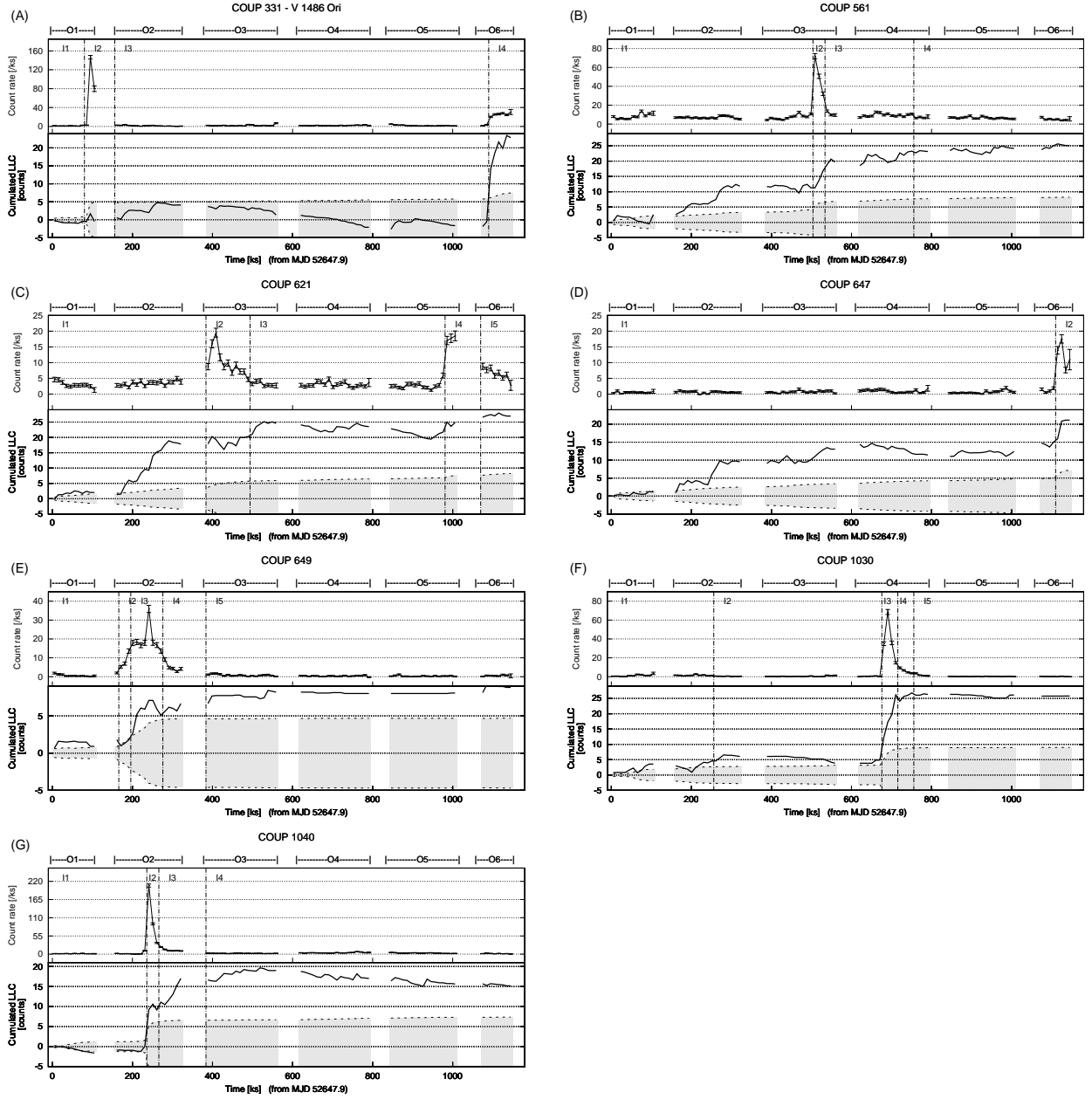


Fig. 3. Panel A to G: Light curves for the objects reported on by Tsujimoto et al. (2005). The time axis refers to the begin of the COUP campaign (MJD 52647.87). Upper panel: Broad-band (2 – 9 keV) light curve (BBLC). Lower panel: The cumulated LLC (CLLC) and an estimate of its width (gray shaded, see Eq. 7). Vertical separators mark change points associated with a shift of the activity level (determined by the Bayesian block analysis of the BBLC).

In Fig. 5 (left panel) we show the LLC pertaining the first half of the COUP campaign, and the most promising candidate interval (100 – 414 ks) for fluorescent emission is gray shaded. In the right panel we plot the spectrum obtained for this interval, which shows a fluorescent line with an EW of 570(280–910) eV. The hot iron-line complex is virtually absent.

During the flare in the following observation, the CLLC indicates another increase by about 10 photons. This num-

ber is confirmed by a spectral analysis of the associated span (504 – 544 ks), where we find a Fe K_{α} I line with an EW of 132(12 – 270) eV. Because of the larger flare continuum the line is much less prominent here, and with 96% it is also much less significant.

5.1.3. COUP 621

The outcome of the light curve analysis for COUP 621 is shown in Fig. 3 (C). COUP 621 shows two flares with the first one fully covered by the observation (except for a probably small fraction of the rise-phase) and the second one remaining unobserved for ≈ 60 ks of its central phase. None of these flares is accompanied by a CLLC excess. The CLLC shows an increase, which is not associated with one of the flares, but rather emerges during a period of quiescence to judge from the BBLC.

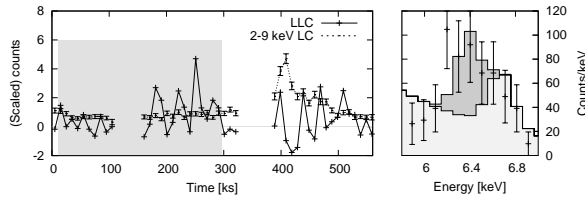


Fig. 6. COUP 621; as in Fig. 5

In Fig. 6 we show the LLC corresponding to O2 and O3 in the left panel where we also indicate the most promising interval (cf. Table 2). In the right panel we show the associated spectrum. Excess emission at the location of the fluorescent line is prominent with a line EW of $600(310 - 970)$ eV, and the hot iron line complex is weak compared to it.

This case is special because two flares detected in soft X-rays are not accompanied by fluorescent Fe K_{α} I line emission, while there is a line detection during a period preceding the first flare. The line emission may be attributed to a hidden flare located at a geometrically quite favorable position. At least it must be attributed to an event, which does not show up in soft X-rays.

5.1.4. COUP 647

Among the sources analyzed by Tsujimoto et al. COUP 647 is by far the most deeply embedded one with a hydrogen column density of $\approx 31 \times 10^{22} \text{ cm}^{-2}$.

The CLLC shows two phases of increase. One associated with a flare towards the end of the COUP campaign, and another one earlier in a presumably quiescent phase of the source (see Fig. 3 D). Our automated CLLC analysis returns the first phase, in particular the 50 – 626 ks interval, as the most promising candidate interval, for which we show the spectrum in the left panel of Fig. 7. The EW of the line in this phase is $440(194 - 767)$ eV.

Additionally, we show the spectrum of the flare during which the line shows up with an EW of $150(10 - 300)$ eV.

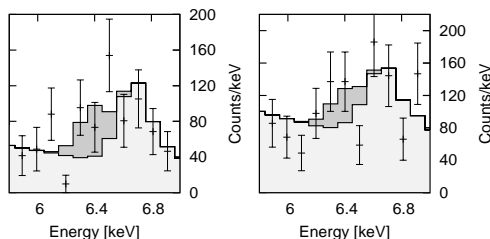


Fig. 7. Left panel: excerpt of the spectrum during the bona fide quiescent phase of COUP 647. Right panel: The same part of the spectrum during the flare.

5.1.5. COUP 649

Among the sources of fluorescent emission reported on by Tsujimoto et al. (2005), COUP 649 is the one with the weakest Fe K_{α} I line.

Figure 3 (E) shows the BBLC and the associated CLLC. The source signal is dominated by a single flare, beyond which the source is virtually invisible. This source was rejected by our automated analysis, because the determined excess is not sufficient to fulfill our criteria. The light curve of COUP 649 shows rapid variability where the source is visible, and we speculate that this impedes an appropriate light curve analysis.

In a spectral analysis of the flare, however, we find a fluorescent emission with an EW of $\approx 260(80 - 450)$ eV, compatible with the results given by Tsujimoto et al. (2005). We note that, in this case, the EW is not affected by time averaging, because only the flare contributes signal.

5.1.6. COUP 1030

Figure 3 (F) shows the light curves pertaining to COUP 1030. A flare occurs in O4, and we find that the source is piled-up in this state. In the following analysis we, therefore, revert to an annulus-shaped source region neglecting the innermost 0.6 arc-sec.

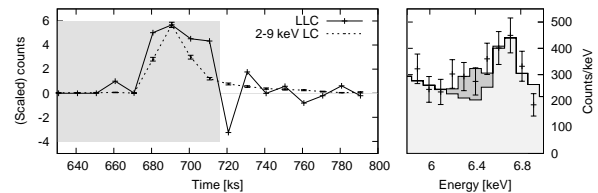


Fig. 8. COUP 1030; as in Fig. 5

The automated CLLC analysis yields the 206 – 716 ks interval to be the most promising to detect fluorescent Fe K_{α} I emission. This interval covers the flare, which, according to the CLLC, provides the largest contribution of fluorescent photons. In the right panel of Fig. 8 we show the spectrum of COUP 1030 during the most promising interval, and our spectral analysis shows a fluorescent line with an EW of $143(56 - 231)$ eV. The result is compatible with the values given by Tsujimoto et al. (2005); time averaging has no effect on the EW if the signal is strongly concentrated in a single flare. This source appears much like a “text book” example of fluorescent emission originating from photoionization both with respect to temporal behavior and EW.

5.1.7. COUP 1040

COUP 1040 remains virtually invisible in the > 6.2 keV band, except for a flare period during O2.

Figure 3 (G) shows the light curves. The LLC indicates fluorescent emission accompanying a flare. There is a steep rise in a short (≈ 10 ks) interval in the central flare, and the CLLC continues to rise during the decay phase. Our automated analysis determines an interval containing the decay phase (266 – 544 ks) of the flare to be the most promising candidate interval to be searched for fluorescent Fe K_{α} I emission. In Fig. 9 (left panel) we show the spectrum pertaining to this interval. Indeed, there

may be excess emission at 6.4 keV, however, the continuum in the 5.2 – 6.2 keV range is not well fitted by the model, so that the CLLC may be misleading in this case.

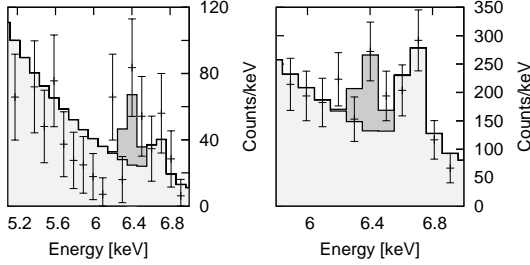


Fig. 9. Left panel: The spectrum during the automatically determined, most promising fluorescent interval of COUP 1040. Right panel: The spectrum during the second COUP observation (O2).

The right panel of Fig. 9 shows the spectrum during the O2, which covers the flare and its decay phase. The signal is much stronger here, and the fluorescent line is detectable. While the line flux of $11(6 - 20) \times 10^{-7}$ ph/(cm² s) is considerably higher than the value reported by Tsujimoto et al. (2005), our EW of 178(90 – 310) eV is compatible with their result, as it remains unchanged by time averaging if no further signal is accumulated.

5.2. Three individual sources with distinct behavior

In the following section we present three additional individual sources with a detection of fluorescent emission. The sources show three different types of temporal behavior of the Fe K_α I line, and further demonstrate the variety of Fe K_α I line emitters.

5.2.1. COUP 267

The X-ray spectrum of COUP 267 shows the characteristics of a “two absorber X-ray source” (TAX source, e.g., Güdel et al. 2007), with a mildly absorbed soft component dominating below about 1 keV and a hard component hidden behind a significantly higher column of material. During the leading 100 ks of COUP campaign data, COUP 267 shows a flare (see Fig. 10, upper panel). A comparison of the soft (0.3 – 1.2 keV) light curve and its hard counterpart (1.2 – 9.0 keV) uncovers that the flare exclusively affects the hard band.

In Fig. 10 we show the light curves and the spectrum of COUP 267 during the 30–196 ks time span selected by our automatic search for fluorescence, which basically covers the decay phase of the flare. The EW of the fluorescent line amounts to 400(180 – 670) eV here. The two differently absorbed thermal components can clearly be distinguished in the spectral model, and excess emission at the energy of the fluorescent line is visible. The upper right box in Fig. 10 shows a close-up of this region, where the best-fit line is also indicated.

The TAX nature of this source implies the presence of considerable amounts of circumstellar material surrounding the central star, where fluorescent emission may well have its origin. Although the measured EW appears high compared to the model predictions (see Sect. 6), the fluorescent emission is associated with the flare, and we conclude that photoionization provides a reasonable explanation for the observation.

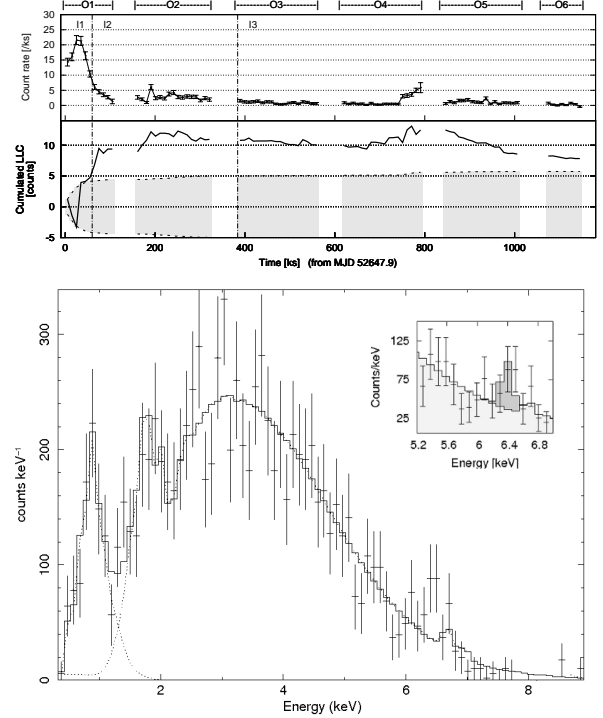


Fig. 10. Upper panel: The 2 – 9 keV band light curve and the CLLC of COUP 267. Lower panel: The spectrum during the 30 – 196 ks interval with a close-up of the Fe K_α I line region.

5.2.2. COUP 599

The strength of the X-ray source COUP 599 remains constant through the entire COUP campaign as demonstrated by the light curve shown in Fig. 11. The CLLC rises almost without interruption. Accordingly, the most promising fluorescent interval found in our automated search comprises virtually the entire data.

In the lower panel of Fig. 11, we show the spectrum of the source in the 10 – 1080 ks interval. There is excess emission at 6.4 keV, which we attribute to the fluorescent line, and we determine an EW of 450(220 – 660) eV for it.

The position of COUP 599 is about 1 arcsec northwest of the Becklin-Neugebauer object (Becklin & Neugebauer 1967), and, as already noted by Garmire et al. (2000) in a pre-COUP study, it may be related to it, although an independent origin cannot be excluded.

The X-ray luminosity of this source is constant and so is its Fe K_α I line flux. Again, the EW is high compared to values rarely exceeding 100 eV as derived by Drake et al. (2008), but the strong absorption with a column density of $N_H = 7.6(6.6 - 8.7) \times 10^{22}$ H/cm², points towards the presence of circumstellar material, which could yield a quite favorable geometry.

5.2.3. COUP 1499, V NX Ori

While V NX Ori is found in quiescence for the longest part of the COUP campaign, it also shows a period of remarkable activity. This begins with a very short flare taking place towards the end of the second observation. Here, the count rate skyrockets to about 40 c/ks (2 – 9 keV band) within 2 ks and then de-

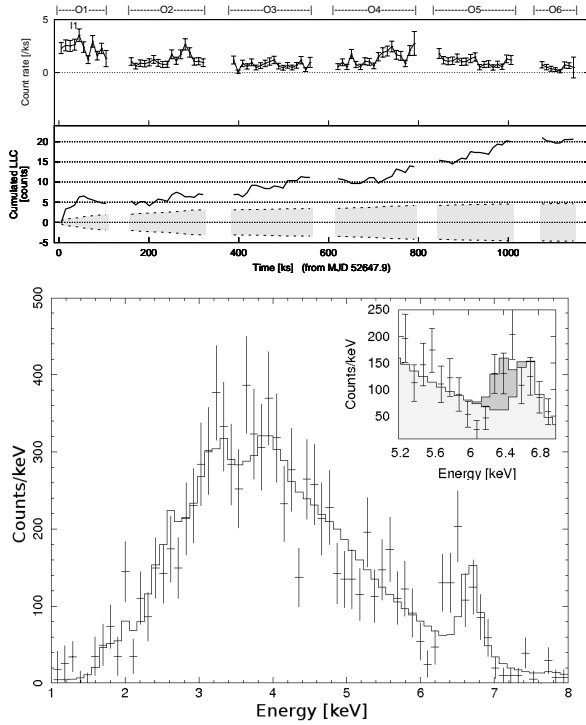


Fig. 11. Upper panel: The 2 – 9 keV band light curve and the CLLC of COUP 599. Lower panel: The spectrum in the 10 – 1080 ks interval and a close-up of the Fe K_{α} I line region.

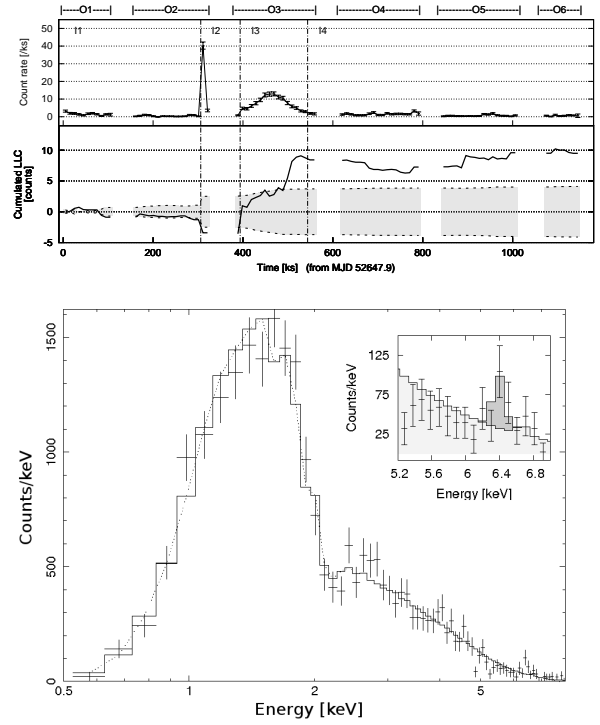


Fig. 12. Upper panel: The 2 – 9 keV band light curve and the CLLC of COUP 1499. Lower panel: The spectrum in the 384 – 524 ks interval and a close-up of the Fe K_{α} I line region.

cays quickly, so that the entire event does not last for more than ≈ 15 ks.

After the interruption due to the *Chandra* orbit, the next observation starts with another short flare which shades into a long lasting, possibly related flare event. In Fig. 12 we show the spectrum during the 384 – 524 ks time span found by our automated analysis (see Table 2), which approximately covers the second, long lasting flare.

While the CLLC does not indicate fluorescent emission during the first, short and more violent event, it does during the longer flare. The associated spectrum demonstrates line emission for which we measure an EW of 370(145 – 630) eV.

5.3. Consequences of temporal resolution on the Fe K_{α} I line equivalent widths

In the preceding passages we demonstrated the temporal behavior of the Fe K_{α} I line for a number of sources including those presented by Tsujimoto et al. (2005). The EW of the Fe K_{α} I line is often used to check whether the observations can be reconciled with predictions from theory or not. Therefore, it is worth briefly discussing the effects of the time resolution on this quantity.

In sources where one major flare provides the majority of all source photons, including Fe K_{α} I line photons, such as COUP 649 and COUP 1030, time averaging over a larger span has no effect on the calculated EW, because line and continuum emission are both scaled by the same factor. It, however, has an effect on the measured fluxes, which are then too low.

The measured EW will be too low, if the quiescent phases, which are usually much longer than active periods, or several flares contribute a significant amount of flux, as for instance in COUP 331 and COUP 621. In these cases, continuum signal is accumulated, which, afterwards, is compared to the Fe K_{α} I line signal being collected during a shorter period. Here, both the measured average Fe K_{α} I line flux and the associated EW will be lower than values determined for appropriate time spans.

As it is not possible to accumulate negative signal in the Fe K_{α} I line or the underlying continuum, maybe with the exception of background and statistical fluctuations, the time averaged values can be regarded a lower limit on both the Fe K_{α} I line flux and EW.

5.4. Combined excess emission

In the previous sections, we presented a sample of sources with excess emission at 6.4 keV, which we attribute to the fluorescent Fe K_{α} I line. In this section we combine a larger amount of data, to further corroborate this statement.

In Fig. 13 we show the summed residuals corresponding to all intervals listed in Table 2 in the upper panel and, in the lower panel, the summed residuals for all sources showing no fluorescent emission according to our analysis. For each spectrum we determined the residuals by subtracting the best-fit model from the observed data and added up the individual results. We prefer this approach to adding up the individual spectra themselves, because these differ significantly from each other both in flux level and spectral shape. The residuals already account for the dif-

ferences in spectral shape, and the contribution of spectra with more photons grows with the square root of the photon number, and not linearly as would be the case otherwise.

An emission line feature, which is not accounted for in the models but present in some or all of the spectra, should lead to an accumulation of residual photons at the respective energy. In Fig. 13 we show the result using the residuals with respect to the thermal model (cf. Sec.4.3) and a power law model extended by a Gaussian line of variable width (but < 0.1 keV) and normalization at a fixed energy of 6.7 keV to account for the hot iron lines.

In both cases, an excess at 6.4 keV can clearly be identified. We find that this excess is well represented by a Gaussian centered at 6.4 keV. The best-fit width of the Gaussian is 100 eV, which is consistent with an intrinsically narrow, instrumentally broadened line at the location of the fluorescent Fe K_{α} I line. We note that leaving the central energy as a free fit parameter does not alter this result. Depending on the considered energy range for the adaption of the Gaussian, and on whether we allow an offset for the Gaussian line, we find amplitudes of 300–400 photons. Therefore, we argue for the presence of ≈ 350 excess photons, which can be attributed to the fluorescent Fe K_{α} I line in these spectra. This number can be converted into an average line EW of roughly 250 eV, which we find in good agreement with previous results.

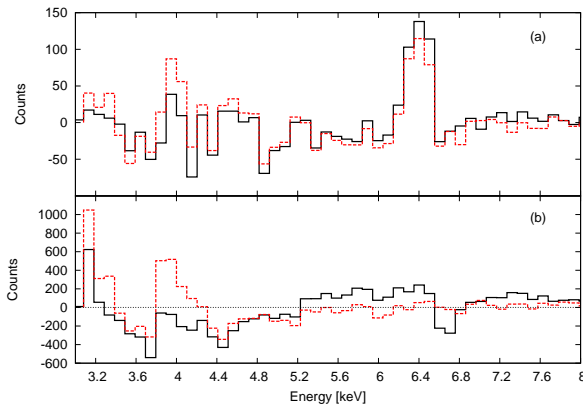


Fig. 13. The summed residuals from all bona-fide fluorescent intervals (panel a) and the same for all sources not showing intervals with fluorescent emission (panel b). Solid (black) line: The residuals with respect to thermal models, dashed (red) line: The residuals with respect to a power law model with additional hot iron line at 6.7 keV.

Instead of collecting the residuals only from the periods of bona-fide fluorescent emission, the collection can also be inverted to comprise only data of those sources in which no Fe K_{α} I line emission was detected. Neither of the resulting curves, whether calculated with respect to the thermal or the power law models, shows a distinct feature at 6.4 keV (Fig. 13, lower panel). The residuals collected from the thermal models show a substructure indicating that the average spectral slope is too steep. Such an effect is not present in the power-law models, which, however, cover a much smaller fraction of the spectrum. Consulting the power law fit residuals, a small excess of ≈ 100 photons at 6.4 keV may still be present, but it is not clearly set apart from the noise. We note that we also find no surplus of

negative residuals here as would be expected, if we only had removed sources showing a positive noise excess from the sample.

5.5. Comparison features at different energies

For the following analysis we revert to the Bayesian block data, i.e., a subdivision made without paying special attention to the presence or absence of the Fe K_{α} I line, even though this might be the case due to physical reasons. Starting from the best-fit thermal model, we add a narrow emission line at various energies between 5.5 keV and 6.7 keV. For each Bayesian block, we record the best-fit line fluxes and EWs.

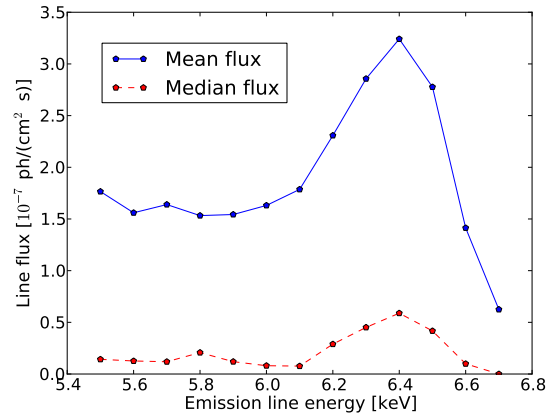


Fig. 14. Mean (solid line) and median (dashed line) flux for narrow emission line at various energies.

In Fig. 14 we show the mean and median line flux determined for the emission line, shifting it from 5.5 keV to 6.7 keV in steps of 100 eV. This set-up includes the actual Fe K_{α} I line at 6.4 keV as a special case. Both mean and median line flux are > 0 everywhere, since we demand an emission line. We do not expect any strong features between 5.5 keV and 6.3 keV, so that the results can be attributed to the photon noise.

The mean line flux shown in Fig. 14 remains constant until the line energy exceeds 6.1 keV, after which the mean flux rises, reaches a maximum at 6.4 keV, and falls again. We note that the decrease towards 6.7 keV happens because the thermal models include the hot iron lines. To assure that not a few large values dominate the plot, which is conceivable if the mean line flux is considered, we also give the median line flux, which is more stable against outliers. At a lower level, the median flux shows the same basic pattern with a maximum at 6.4 keV. The level shows that many values are close to zero, reflecting the cases in which an absorption line would formally yield a better fit.

At each line energy the statistic for the comparison line is different, because it is affected by the spectral shape and the effective area. Under the hypothesis that there is nothing special about the Fe K_{α} I line energy, so that the majority of our detections should actually be attributed to noise, the derived result is implausible. If this hypothesis was to be accepted, there should be a gradual evolution of the mean and median line fluxes over the entire range, which is, indeed, the case until the line energy exceeds 6.1 keV, but not beyond.

The findings summarized in Fig. 14 are compatible with an instrumentally broadened emission line at 6.4 keV, and we ad-

duce this as a corroboration of our interpretation of the observed excess emission as fluorescent Fe K_{α} I line emission, which is distinct from photon noise.

5.6. Duty cycle of Fe K_{α} I line emission

In Table 2 we list the sources and time spans, which show significant Fe K_{α} I line emission according to our analysis. The table comprises 23 sources, with a total observation time of 23×838 ks \approx 19 000 ks. Summing up the interval lengths, we find that fluorescent emission is detected during \approx 50% of this time.

Using the entire sample of 106 sources as a reference, fluorescent emission is detectable during about 10% of the observation time, and it is distributed among 20% of the sample sources. This consideration does only take into account those sources in which fluorescent emission can be claimed with reasonable certainty. Based on the creation scenario of fluorescent emission, it seems likely that the number of fluorescent sources is actually larger, yet a detection cannot be claimed where the signal remains insufficient. The duty cycle derived here should, therefore, be regarded a minimum, limited by the sensitivity of the instrument and, of course, our method.

6. On the origin of the Fe K_{α} I line emission

The reality of the fluorescent Fe K_{α} I line has so far been established in quite a number of stellar sources. While all authors agree that neutral or lowly ionized iron gives rise to the photons making up this spectral component, there is still some debate whether nonthermal electrons contribute to the excitation of the iron ions. In the following, we briefly juxtapose photoionization and electron collisional excitation regarding the expected EWs and temporal behavior.

6.1. Implications of photoionization

The fluorescent emission caused by photoionized neutral or lowly ionized iron was investigated theoretically by a number of authors. Bai (1979) and Drake et al. (2008) carried out Monte Carlo calculations, simulating solar and stellar flares. George & Fabian (1991) simulated an accretion disk illuminated with a power law spectrum, approaching the situation in AGN sources. George & Fabian (1991) obtain typical EWs between 100 – 200 eV for a centrally illuminated disk using power law photon-indices between $\Gamma = 1.3 - 2.3$. The EWs obtained by Bai (1979) and Drake et al. (2008) for thermal input spectra tend to be smaller, rarely exceeding 100 eV.

While the above results refer to solar iron abundances of $\approx 4 \times 10^{-5}$ Fe/H, the Fe K_{α} I line EW caused by photoionized iron can be increased, when larger iron abundances are assumed (Drake et al. 2008). In an analysis of the correlation between iron abundance and Fe K_{α} I line EW, however, Ballantyne et al. (2002) find that the EW cannot be increased beyond any limit. As already indicated by Bai (1979) (Fig. 4) or Matt et al. (1997), the EW rises linearly for iron abundances of the order of or lower than the solar value beyond which the relation flattens. According to Ballantyne et al. (2002), the maximal obtainable Fe K_{α} I line EW is around 800 eV.

The Fe K_{α} I line EWs expected from photoionized iron is, thus, of the order of \approx 100 eV and may reach \approx 800 eV under very favorable conditions. The light curve of the Fe K_{α} I line should be correlated with the light curve of the incident soft

X-ray continuum, but reverberation effects may be present. Assuming a typical scale of 20 AU for the extent of a stellar source, delays, if present, would be of the order of \approx 10 ks.

High Fe K_{α} I line EWs and a virtually unpredictable temporal behavior may be obtained, if totally or partially hidden X-ray sources are considered as proposed by Drake et al. (2008). The continuum emission by those sources can contribute to the reprocessed photon field, but their direct continuum radiation remains invisible, so that the measured Fe K_{α} I line flux may be significant providing a large EW, which appears to be uncorrelated with the measured continuum.

6.2. Electron collisional excitation

The subject of electron collisional excitation of the fluorescent Fe K_{α} I line was for example investigated by Emslie et al. (1986). These authors calculate the Fe K_{α} I line photon flux, Φ , due to electron excitation; the result is given in their Eq. 12. In combination with their Eq. 7, the relation can be recast and written as

$$\frac{4\pi R^2}{AF(> E_1)} \Phi = \omega \beta (Ab_{Fe}) \frac{\gamma - 1}{\gamma} \frac{E_1^{\gamma-1}}{K\nu} \int_{\chi}^{\infty} E^{1-\gamma} Q_I(E) dE, \quad (13)$$

where Ab_{Fe} is the iron abundance, $\gamma + 1$ is the spectral index of the incident electron power law spectrum, E_1 is the lower cut-off energy of the electron spectrum, $K = 2.61 \times 10^{-18}$ keV²/cm², $\nu = 1.6 \times 10^{-9}$ is the conversion factor from keV to erg, $\chi = 7.112$ keV is the K-shell ionization energy of neutral iron, ω is the iron fluorescence yield, β is the branching between K_{α} and $K_{\beta,\gamma,\dots}$, Q_I is the cross section for K-shell ionization by iron (see e.g., Hombourger 1998), R is the distance to the source, $F(> E_1)$ is the total injected electron energy flux in ergs/(s cm²), and A is the area of the flare. We note that in Eq. 13 we already assumed that there is no hydrogen column between the electron injection site and the neutral iron, which corresponds to $N^* = 0$ in Emslie et al. (1986).

Assuming $\gamma = 2.1$, $Ab_{Fe} = 4 \times 10^{-5}$, $E_1 = 20$ keV, and a distance of 450 pc, Eq.13 can be partially evaluated

$$AF(> E_1) \approx 4.5 \times 10^{41} \frac{\text{cm}^2 \text{ erg}}{\text{photon}} \times \Phi, \quad (14)$$

where $AF(> E_1)$ is the incident energy flux in the form of electrons in ergs/s. Using Eq.14 we derive that, for the typical Fe K_{α} I line fluxes of several times 10^{-7} ph/(cm² s) measured for the COUP sources (Tsujimoto et al. 2005), the injected flux of electrons in excess of 20 keV should be of the order of 10^{35} erg/s.

This number is enormous compared to solar values, where the total energy deposited in nonthermal electrons during a flare is of the order of 10^{32} erg. Even though flares in Orion YSOs may be ‘several orders of magnitude more powerful than any solar flare’ (Getman et al. 2008), the energetics remain problematic. Using Eq. 17 from Saint-Hilaire & Benz (2005), we estimate the amount of thermal energy, E_{th} , contained in the plasma of a large flare to be

$$E_{th} = 3k_b T \sqrt{EM^2/n^2} \cdot f \approx 10^{36} \text{ erg}, \quad (15)$$

assuming an emission measure of 10^{55} cm⁻³, a density of $n = 10^{12}$ cm⁻³, a temperature of $k_b T = 10$ keV, and a filling factor, f , of unity. In their analysis of RHESSI data of medium sized solar flares, Saint-Hilaire & Benz (2005) concluded that E_{th} is of the order of the energy contained in nonthermal particles. Extrapolating this result to the Orion flares, we conclude

that currents sufficient to provide significant Fe K_{α} I line fluxes cannot be sustained for longer than a few seconds.

As pointed out by Emslie et al. (1986), a contribution of electron induced fluorescent emission may be observed during the impulsive phase of a flare. The Fe K_{α} I line flux due to electron collisional excitation should be temporally correlated with the hard X-ray flux, which was, indeed observed by Emslie et al. (1986). Such data are, however, not available for Orion, so that we cannot revert to this line of argumentation.

Recently, Peterson et al. (2010) presented high resolution radio images of the Algol binary system resolving a large coronal loop reaching from one to the other pole of the K giant secondary, being orientated towards the primary B star. The authors modeled the radio emission observed from this loop by assuming synchrotron emission from an electron population with a homogeneous density of $n_e = 10^{-3}$ electrons/cm $^{-3}$ and a power law spectrum so that $n(E) = n_e(E/E_{min})^{-3/2}$ where $E_{min} = 80$ keV. Assuming that the electrons are moving at the speed of light, we estimate an electron flux of roughly $3 \times 10^{10} \text{ cm} \cdot 1000 \text{ cm}^{-3} = 3 \times 10^{13}$ electrons/cm $^{-2}$. Further assuming a loop length of 10^{12} cm and a radius to loop length ratio of 0.1 (Favata et al. 2005), the electron flux over the entire loop cross section becomes $\approx 10^{35}$ electrons/cm 2 . If we attribute an energy of 100 keV to all of these electrons, the resulting energy flux in form of energetic electrons becomes 10^{28} erg/s. Although this number is still far below the needed value, we note that Favata et al. (2005) find evidence for large magnetic loops with half lengths of $\approx 10^{12}$ cm in their analysis of large COUP flares, which may connect the stellar photosphere with a disk. Without being able to give a detailed physical modeling, we do not exclude that under certain conditions sufficient fluxes of energetic electrons may be sustained in large magnetic structures.

When a population of high energy electrons hits a thick target such as a stellar photosphere, the electrons thermalize in the plasma and heat it. This gives rise to the evaporation of soft X-ray emitting loops observed during solar and stellar flares. Inspired by their findings, Giardino et al. (2007) elaborate on a mechanism, which can prevent a population of accelerated electrons from causing a soft X-ray flare. Basically, the authors suggest that, if the plasma density in the flux tube into which the electrons are injected, is high enough, the electrons do not thermalize in the photosphere, but are decelerated in situ. During this process, energy is deposited in nonthermal hard X-rays and collisional excitation of heavier ions such as iron, potentially resulting in Fe K_{α} I line photons. Appropriate conditions for this mechanism to work may, indeed, be found in young stars with ongoing accretion.

6.3. Putting our analysis into the context

As outlined in Sec. 6, model calculations of the Fe K_{α} I line strength based on photoionization rarely predict line EWs > 100 eV. Yet, the EWs listed in Table 2 tend to be significantly larger than 100 eV, even though some may be smaller considering the errors. The values reported in Table 2 are qualitatively compatible with the numbers published for Elias 29, for which Giardino et al. (2007) derive EWs of up to ≈ 800 eV during their second time segment.

If photoionization is to be held responsible for the line emission, it must explain *all* of these observations; both the observed EW and the temporal behavior. As the observed EWs tend to be higher than typical predictions, this issue should be addressed first. Drake et al. (2008) discuss four ways in which the Fe K_{α} I line EW may be raised. These are supersolar Fe abun-

dances, disk flaring, a contribution of electron collisional excitation, and line-of-sight obscuration of the central flaring source. According to Drake et al. disk flaring, which increases the solid angle coverage of the reflector, can increase the expected EW by factors < 2 , and increasing the iron abundance ensues a roughly linear response of the line EW. EWs of the order of 400 eV as in the majority of our detections, are, therefore, within reach without reverting to extreme physical conditions. Additionally, we note that obscuration of the X-ray source does not only increase the Fe K_{α} I line EW when the absorber is impenetrable, but also if it has only small optical thickness. The reason is that fluorescent photons at 6.4 keV can be created as the X-rays are passing the absorber, while continuum photons can only be destroyed. Yaqoob et al. (2010) show, in a different context, that the optically thin approximation for the fluorescence problem breaks down for column densities as low as $\approx 2 \times 10^{22}$ H/cm 2 , which should also be the scale on which this effect may become noticeable. The effect may well be responsible for a fraction of the observed EW in sources with sufficiently large absorbing columns, i.e., in about half of our sources (see Table 2).

The most extreme Fe K_{α} I line is observed during the rise phase of a flare in V 1486 Ori, where we determine a line EW of ≈ 1400 eV (see Sect. 5.1.1) exceeding typical model predictions by an order of magnitude. To explain this measurement in the frame of photoionization, Drake et al. (2008) suggest that the Fe K_{α} I line is due to photoionization by a partially hidden X-ray source. While this is an appealing idea, the LLC shown in Fig. 4 is also suggestive of an impulsive peak, as presented by Emslie et al. (1986) (Fig. 3) for the case of the Sun. According to Emslie et al. (1986) this peak, which, however, lasted for no longer than ≈ 20 s there, is associated with Fe K_{α} I line emission due to electron collisional excitation. Assuming that this is also true for the case of V 1486 Ori, we can calculate the electron flux needed to excite the observed line. Applying Eq. 14 substituting the line flux of $\approx 8 \times 10^{-6}$ ph/(cm 2 s) during the time span given in Table 2, yields an energy input of about 3×10^{36} ergs/s that would be required to sustain this line by electron collisional excitation. Whether or not the observed Fe K_{α} I line emission of V 1486 Ori contains a contribution originating from electron collisional excitation cannot ultimately be decided from the data at hand, but if it does, the energy released into electrons must be enormous.

Even though EWs of ≈ 400 eV may be explained by photoionization, some sources still show a puzzling temporal behavior. For example COUP 621, one of the Tsujimoto et al. (2005) sources, shows two flares, which seem not to be accompanied by fluorescent emission, whereas Fe K_{α} I line emission is observed during a bona-fide quiescent period preceding the first flare. This observation may be attributed to a ‘‘hidden flare’’ somewhere behind the star or the disk, which is only visible in its reprocessed light. It may also be associated with an event preceding and maybe preparing the first flare such as magnetic reconnection releasing high energy electrons. Feigelson et al. (1998) show that there are large scale magnetic structures in an X-ray protostar in Corona Australis and that the observed polarized radio emission arises from a nonthermal electron population spiraling along the field lines. Giardino et al. (2007) argue that magnetic reconnection could be sustained for several days, but they do not give a physical model for it. As, however, the energetics of collisional electron excitation is very challenging (see Eq.14), this explanation seems physically problematic, and, in light of current knowledge, photoionization by a hidden flare appears a more straight forward answer. Similar to COUP 621, other sources like V 1486 Ori and V NX Ori show both, flares

with and without detectable fluorescent emission. We interpret this as a relic of a manifold geometry. Depending on the location of flare eruption, the conditions for photoionizing iron and creating fluorescent photons, at least towards our line of sight, can be quite different. Perhaps some flares are associated with large magnetic structures connecting photosphere and disk, as proposed by Giardino et al. (2007) or Favata et al. (2005), but also different locations above the photosphere itself have considerable consequences for the observed Fe K_{α} I line EW (e.g., Bai 1979; Drake et al. 2008).

7. Conclusion

As a first result of this work, we state that there are far more X-ray sources with detectable fluorescent Fe K_{α} I line emission in the COUP field than previously reported. While extending the sample of known stellar Fe K_{α} I line sources, the major part of this study is dedicated to the analysis of the temporal behavior of the Fe K_{α} I line emission, which yields another result: a large diversity in the relation between Fe K_{α} I line emission and soft X-ray continuum.

Fluorescent emission is found to accompany a flare in some cases, sometimes it is a persistent feature, and in other cases it appears “out of nothing” with no obvious response by the soft X-ray continuum.

The diverse temporal behavior of fluorescent Fe K_{α} I line emission cannot always easily be reconciled with the picture of photoionization as the dominant excitation mechanism of this emission. Even in sources which show flares during the COUP campaign, the majority of fluorescent photons may still be observed in bona-fide quiescent phases. In those cases, but also in others, the observed EWs are often appreciably higher than predicted by photoionization-based model calculations applying conventional assumptions on geometry and elemental abundances.

Nonetheless, we argue that photoionization remains the most promising explanation for the observations. The alternative mechanism of electron collisional excitation is appealing in some cases, because it provides an explanation for Fe K_{α} I line emission not accompanied by a change in the level of soft X-ray emission, but the energetics are challenging. In order to explain the observed Fe K_{α} I line fluxes, enormous fluxes of energetic electrons, which remain invisible otherwise, must be sustained sometimes for days. Electron collisional excitation may certainly provide a fraction of the fluorescent line photons, but it can hardly serve as an explanation for their majority.

The observations can be reconciled with predictions based on photoionization, if we assume more complicated environments. This includes partially or completely hidden X-ray sources as well as a modification of the iron abundance. Also fluorescence occurring in the circumstellar absorbing material, currently not accounted for in the models, possibly accounts for a fraction of the observed EWs.

Our current understanding of the fluorescent Fe K_{α} I line is certainly not satisfactory. The great diagnostic power of the line for a variety of celestial sources makes further observations, covering the line in even more detail, clearly desirable.

Acknowledgements. This work has made use of data obtained from the *Chandra* data archive. S.C. acknowledges support from the DLR under grant 50OR0105. We thank Eric D. Feigelson for providing us with the outcomes of the analysis of the COUP data carried out by his collaborators and him.

References

- Anders, E. & Grevesse, N. 1989, *Geochim. Cosmochim. Acta*, 53, 197
 Bai, T. 1979, *Sol. Phys.*, 62, 113
 Ballantyne, D. R. & Fabian, A. C. 2003, *ApJ*, 592, 1089
 Ballantyne, D. R., Fabian, A. C., & Ross, R. R. 2002, *MNRAS*, 329, L67
 Bambynek, W., Crasemann, B., Fink, R. W., et al. 1972, *Reviews of Modern Physics*, 44, 716
 Becklin, E. E. & Neugebauer, G. 1967, *ApJ*, 147, 799
 Cash, W. 1979, *ApJ*, 228, 939
 Czesla, S. & Schmitt, J. H. H. M. 2007, *A&A*, 470, L13
 Doschek, G. A., Meekins, J. F., Kreplin, R. W., Chubb, T. A., & Friedman, H. 1971, *ApJ*, 170, 573
 Drake, J. J., Ercolano, B., & Swartz, D. A. 2008, *ApJ*, 678, 385
 Emslie, A. G., Phillips, K. J. H., & Dennis, B. R. 1986, *Sol. Phys.*, 103, 89
 Favata, F., Flaccomio, E., Reale, F., et al. 2005, *ApJS*, 160, 469
 Feigelson, E. D., Carkner, L., & Wilking, B. A. 1998, *ApJ*, 494, L215+
 Garmire, G., Feigelson, E. D., Broos, P., et al. 2000, *AJ*, 120, 1426
 George, I. M. & Fabian, A. C. 1991, *MNRAS*, 249, 352
 Getman, K. V., Feigelson, E. D., Broos, P. S., Micela, G., & Garmire, G. P. 2008, *ApJ*, 688, 418
 Getman, K. V., Flaccomio, E., Broos, P. S., et al. 2005, *ApJS*, 160, 319
 Giardino, G., Favata, F., Pillitteri, I., et al. 2007, *A&A*, 475, 891
 Güdel, M., Telleschi, A., Audard, M., et al. 2007, *A&A*, 468, 515
 Hombourger, C. 1998, *Journal of Physics B Atomic Molecular Physics*, 31, 3693
 Imanishi, K., Koyama, K., & Tsuboi, Y. 2001, *ApJ*, 557, 747
 Kaastra, J. S. & Mewe, R. 1993, *A&AS*, 97, 443
 Matt, G., Fabian, A. C., & Reynolds, C. S. 1997, *MNRAS*, 289, 175
 Neupert, W. M., Gates, W., Swartz, M., & Young, R. 1967, *ApJ*, 149, L79+
 Parmar, A. N., Culhane, J. L., Rapley, C. G., et al. 1984, *ApJ*, 279, 866
 Peterson, W. M., Mutel, R. L., Güdel, M., & Goss, W. M. 2010, *Nature*, 463, 207
 Protassov, R., van Dyk, D. A., Connors, A., Kashyap, V. L., & Siemiginowska, A. 2002, *ApJ*, 571, 545
 Saint-Hilaire, P. & Benz, A. O. 2005, *A&A*, 435, 743
 Scargle, J. D. 1998, *ApJ*, 504, 405
 Smith, R. K., Brickhouse, N. S., Liedahl, D. A., & Raymond, J. C. 2001, *ApJ*, 556, L91
 Sunyaev, R. A. & Churazov, E. M. 1996, *Astronomy Letters*, 22, 648
 Tanaka, Y., Nandra, K., Fabian, A. C., et al. 1995, *Nature*, 375, 659
 Testa, P., Drake, J. J., Ercolano, B., et al. 2008, *ApJ*, 675, L97
 Tsujimoto, M., Feigelson, E. D., Grosso, N., et al. 2005, *ApJS*, 160, 503
 Yaqoob, T., Murphy, K. D., Miller, L., & Turner, T. J. 2010, *MNRAS*, 401, 411
 Zarro, D. M., Dennis, B. R., & Slater, G. L. 1992, *ApJ*, 391, 865

3.7 Towards the substellar regime

The Hertzsprung-Russel diagram of ROSAT sources (see Fig. 8) impressively demonstrated that X-ray emitters are distributed all over the main sequence. While the upper limit of the main sequence is clearly marked by the massive O type stars, which are powerful sources of X-ray emission, the situation is more uncertain for objects with low mass, especially as the substellar regime is approached.

In the stellar population with subsolar masses, an important border is crossed at a mass of $\approx 0.3 M_{\odot}$, below which stars become fully convective. Solar like $\alpha\Omega$ dynamos are thought to be located at the “tachocline”, the interface shear layer connecting the rigidly rotating radiative core and the differentially rotating outer convection zone. As a tachocline does not exist in fully convective stars, a change of dynamo type from a solar like $\alpha\Omega$ to a distributed α^2 dynamo is expected at this border, suggesting a change in the structure of the magnetic field. This, in turn, might lead to a sudden change in the X-ray properties at that point, which, however, seems not to be confirmed by observations (e.g., Fleming et al. 1995), maybe indicating a smooth transition from $\alpha\Omega$ to α^2 dynamos. Whatever the actual reason for this might be, it is another example of the already emphasized connection between the stellar interior and stellar activity.

Whether the gravitational collapse of fragments of a molecular cloud gives rise to the formation of a star or not depends on the mass involved, or, more precisely, on the ability of the resulting bodies to sustain hydrogen burning. Objects with a mass below about $0.07 M_{\odot}$ cannot fuse hydrogen into helium and become brown dwarfs or maybe Jupiters. Although, brown dwarfs are believed to be among the most numerous objects in the Galaxy, their faintness complicates direct observations, and, while a number of candidates were already known, the first confirmed discovery of a brown dwarf had to await the year 1995 (e.g., Rebolo et al. 1995).

In late M type stars and evolved brown dwarfs the photospheres become virtually

neutral, which ensues potential magnetic field configurations above the photosphere. As this is already a minimum energy configuration, energy transport via magnetic reconnection, i.e., a topological reconfiguration to a lower energy state, can hardly contribute to the energy budget of the outer atmosphere (Fleming et al. 2000). Nonetheless, flare events are often observed to take place on these late M type stars and also on evolved brown dwarfs (Fleming et al. 2000; Schmitt & Liefke 2002; Rutledge et al. 2000), and Fleming et al. (2000) argue that these must arise from topologically more complex magnetic configurations without a footpoint in the photosphere. The question whether there is a quiescent contribution and, hence, a corona has not yet been completely settled, although observational evidence has been assembled, which points into that direction (Fleming et al. 2003; Schmitt & Liefke 2002; Robrade & Schmitt 2008, 2009; Berger et al. 2008; Robrade et al. 2010).

The faintness of brown dwarfs makes a determination of parameters such as mass and radius particularly difficult. Yet, there is one system in which these quantities can be determined with high accuracy, namely 2MASS J05352184-0546085, the first known eclipsing binary system consisting of two brown dwarfs discovered by Stassun et al. (2006). Although the constituents of that system are young and, therefore, have not yet reached an evolved state in which they spend the longest time of their lives, 2MASS J05352184-0546085 represents an exceptional system, which may greatly contribute to our understanding of low-mass objects and their activity. In the following work, my coworkers and I present the X-ray detection of 2MASS J05352184-0546085 as well as a careful analysis of its properties.

For this work, I provided the major part of the *Chandra* data analysis, while P. Christian Schneider did the XMM-*Newton* data analysis. The interpretation was reached in collaboration with equal contributions by me and P.C. Schneider.

A&A 491, 851–854 (2008)
 DOI: 10.1051/0004-6361:200810818
 © ESO 2008

**Astronomy
&
Astrophysics**

Discovery of X-ray emission from the eclipsing brown-dwarf binary 2MASS J05352184-0546085

S. Czesla, P. C. Schneider, and J. H. M. M. Schmitt

Hamburger Sternwarte, Universität Hamburg, Gojenbergsweg 112, 21029 Hamburg, Germany
 e-mail: stefan.czesla@hs.uni-hamburg.de

Received 18 August 2008 / Accepted 12 September 2008

ABSTRACT

The eclipsing brown-dwarf binary system 2MASS J05352184-0546085 is a case sui generis. For the first time, it allows a detailed analysis of the individual properties of young brown dwarfs, in particular, masses, and radii, and the temperature ratio of the system components can be determined accurately. The system shows a “temperature reversal” with the more massive component being the cooler one, and both components are found to be active. We analyze X-ray images obtained by *Chandra* and XMM-*Newton* containing 2MASS J05352184-0546085 in their respective field of view. The *Chandra* observatory data show a clear X-ray source at the position of 2MASS J05352184-0546085, whereas the XMM-*Newton* data suffer from contamination from other nearby sources, but are consistent with the *Chandra* detection. No indications of flaring activity are found in either of the observations (together ≈ 70 ks), and we thus attribute the observed flux to quiescent emission. With an X-ray luminosity of 3×10^{28} erg/s we find an L_X/L_{bol} -ratio close to the saturation limit of 10^{-3} and an $L_X/L_{\text{H}\alpha}$ -ratio consistent with values obtained from low-mass stars. The X-ray detection of 2MASS J05352184-0546085 reported here provides additional support for the interpretation of the temperature reversal in terms of magnetically suppressed convection, and suggests that the activity phenomena of young brown dwarfs resemble those of their more massive counterparts.

Key words. stars: low-mass, brown dwarfs – stars: binaries: eclipsing – stars: activity – X-rays: individuals: 2MASS J05352184-0546085

1. Introduction

Magnetic activity is extremely common among late-type stars with outer convection zones (e.g., Schmitt 1997). The cause of that activity as diagnosed by chromospheric and coronal emissions is ultimately thought to be a magnetic dynamo operating near the base of the convection zones of these stars. Near the spectral type $\sim M3$, stars are thought to become fully convective, thereby preventing the emergence of a solar like dynamo in their interiors, and yet the activity properties seem to remain unchanged across this borderline (e.g. Fleming et al. 1993). A saturation level of $L_X/L_{\text{bol}} \sim 10^{-3}$ is observed also for fully convective stars, although with substantial dispersion. Ultra cool dwarfs (spectral type M7 and later) show a drop in activity as measured through their H_α emission, and among L-type dwarfs H_α emission is rarely found (Gizis et al. 2000). For the majority of active M dwarfs the ratio between H_α and bolometric luminosity is $\log(L_{\text{H}\alpha}/L_{\text{bol}}) \sim -3.8$, while for most objects of spectral class L this ratio drops below -5 . Mohanty et al. (2002) argue that the high degree of neutrality in the outer atmospheres of very low-mass stars effectively diminishes the activity level with effective temperature.

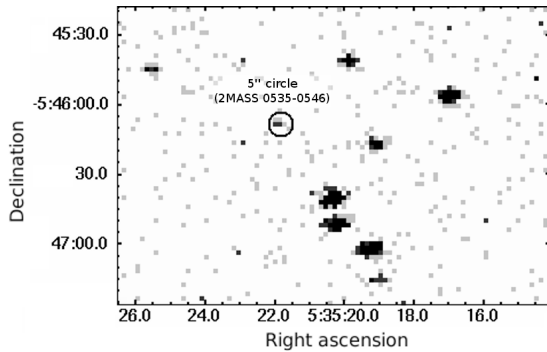
X-ray detections from ultra cool dwarfs are quite sparse, and only a few objects have been identified as X-ray sources during flaring and quiescent periods. Examples comprise the binary system GJ 569 B consisting of two evolved (age ≈ 500 Myr) substellar objects of late-M spectral type detected by Stelzer (2004) and the latest (with respect to spectral type) object being the M9 dwarf LHS 2065 (e.g., Schmitt & Liefke 2002; Robrade & Schmitt 2008). Hence, the behavior of X-ray

emission is unclear as one approaches the boundary towards the substellar brown dwarfs and also the role played by the different stellar parameters for the activity evolution of these objects remains unclear (Stelzer & Micela 2007). It is particularly surprising that some of the very rapidly rotating substellar objects show little or no signs of activity. During the very early phases of their evolution, however, when the optical characteristics of brown dwarfs resemble those of stars with spectral type M6 or so, they are often found to be quite active. Starting with the first X-ray detection of Cha H α 1 in the Chamaeleon I star forming region (Neuhauser & Comeron 1998), quite a number of brown dwarfs settled in star forming regions and (young) clusters have been detected in X-rays. The detection rate is higher for young brown dwarf compared to evolved ones, which might be related to a higher intrinsic X-ray luminosity, hotter outer atmospheres, or both.

A crucial advance in the observational endeavor to unravel the nature of low-mass objects was the discovery of an eclipsing brown-dwarf binary (“2MASS J05352184-0546085” – in the following 2MASS 0535-0546, Stassun et al. 2006), which allowed to directly measure masses, radii, and a temperature ratio for brown dwarfs for the first time. The 2MASS 0535-0546 system is thought to be a member of the Orion Nebular Cluster (ONC) and, hence, very young (age $\approx 10^6$ years). It consists of two $M 6.5 \pm 0.5$ dwarfs in an eccentric ($e = 0.31$) 9.78 day orbit, such that the two eclipses are separated by a phase difference of 0.67. In their analysis of 2MASS 0535-0546 Stassun et al. (2006) determine masses of $M_1 = 56 \pm 4 M_{\text{Jup}}$ and $M_2 = 36 \pm 3 M_{\text{Jup}}$ as well as radii of $R_1 = 0.67 \pm 0.03 R_\odot$ and

Table 1. X-ray data of 2MASS 0535-0546.

Instr.	ID	Obs. time [ks]	Obs. date [MJD]
<i>Chandra</i>	2548	48.5	52 523.54
<i>XMM-Newton</i>	0112660101	22.1	52 167.08

**Fig. 1.** X-ray image (2 arcsec/bin) of the surrounding of 2MASS 0535-0546. A circular (5 arcsec radius) region centered on the nominal target position is superimposed on the image.

$R_2 = 0.49 \pm 0.02 R_\odot$ for the primary and secondary component, respectively. Astonishingly, a “temperature reversal” is observed in this system, i.e., the higher-mass primary component was found to be cooler than its lower-mass companion ($T_1 \approx 2700$ K and $T_2 \approx 2800$ K, Stassun et al. 2007; Reiners et al. 2007).

From the activity point of view 2MASS 0535-0546 is particularly interesting since both components appear to be substantially active, and according to Reiners et al. (2007) the H_α -emission of the primary exceeds that of the secondary by a factor of 7. The same authors find a rotational velocity of about $v \sin(i) = 10 \text{ km s}^{-1}$ for the primary, while they give only an upper limit of 5 km s^{-1} for the secondary. Assuming a magnetic origin of this activity and the same scaling between H_α -emission and magnetic field strength as found for earlier type stars, Reiners et al. (2007) argue for the presence of magnetic fields of $B_f \approx 4 \text{ kG}$ for the primary and $B_f \approx 2 \text{ kG}$ for the secondary.

In this letter we report the discovery of X-ray emission of the eclipsing brown-dwarf binary 2MASS 0535-0546, which provides further support for the presence of magnetic activity in this system.

2. Observations and data analysis

2MASS 0535-0546 was serendipitously covered by observations with both the *Chandra* and *XMM-Newton* observatories; the basic properties of these observations are provided in Table 1.

2.1. The *Chandra* data

The “flanking field south” of the ONC containing 2MASS 0535-0546 was observed with the “ACIS I” instrument onboard *Chandra*. In the associated image 2MASS 0535-0546 is located relatively far off-axis (6.7 arcmin), but is still well exposed, so that a sensitive search for X-ray emission is feasible. The *Chandra* image in the vicinity of 2MASS 0535-0546 is shown in Fig. 1.

In an effort to suppress background and with the knowledge, that young brown dwarfs have X-ray spectra with median energies of the order of or higher than 1 keV (e.g. Preibisch et al. 2005), we limited the energy range of the image to the 0.5–2.5 keV band; a circle of radius 5 arcsec is drawn around the nominal position of 2MASS 0535-0546. According to our point-spread-function (PSF) modeling the encircled region contains $\approx 95\%$ of the 1 keV photons from a point source at the respective off-axis position of the target. Within this circle we find a total of 8 photons. Extrapolating the photon numbers measured in the same energy band from nearby source-free regions yields an expectation value of 0.8 background counts. The Poisson probability of obtaining 8 or more counts with an expectation value of 0.8 is only 2×10^{-7} . Therefore, we attribute the recorded signal to an X-ray source with a count level of 7.2 ± 2.8 photons. What about out-of-band photons? In the considered source region not a single photon with an energy below 500 eV was detected, while two photons are contained in the 2.5–10 keV band. This number is, however, in good agreement with the expectation value derived from the close-by comparison region, and we, thus, attribute these photons to background.

The median energy of the source photons is 1.4 keV, a value going well with those obtained by Preibisch et al. (2005) for 8 other brown dwarf members of the ONC detected in a quiescent state. For the depth of the absorbing column towards 2MASS 0535-0546 we estimated a value of $n_H = 10^{21} \text{ cm}^{-2}$ combining the visual extinction of $A_V \approx 0.75 \text{ mag}$ given by Stassun et al. (2006) with the relation

$$n_H [\text{cm}^{-2}] = 1.79 \times 10^{21} \text{ mag}^{-1} \cdot A_V$$

derived by Predehl & Schmitt (1995); a result consistent with the lower values derived from brighter, close-by X-ray sources. Assuming an absorbed one-component thermal spectrum with subsolar (0.3) abundances, a plasma temperature of $\approx 2 \text{ keV}$, and a distance of 450 pc (e.g. Stassun et al. 2006) we compute an X-ray luminosity of $(3.0 \pm 1.2) \times 10^{28} \text{ erg/s}$ in the 0.5–2.5 keV band, which – again – is well covered by the range determined by Preibisch et al. (2005).

To check the uniqueness of our identification we searched for other potential emitters close (30 arcsec) to 2MASS 0535-0546, but neither Simbad¹, NED², nor the 2MASS-survey provided any candidates in the environment under consideration. Therefore, we attribute the detected X-ray emission to 2MASS 0535-0546.

2.1.1. Timing

Do the source photons arrive homogeneously distributed in time or not? In Fig. 2 we present the background-subtracted 0.5–2.5 keV band light-curve of 2MASS 0535-0546 in the upper panel and the individual photons (registered by their energies) plotted against arrival time in the lower panel. While no photons arrived during the first quarter of the observation, the assumption of a constant arrival rate is still consistent with the observations. More importantly, the light curve (cf., Fig. 2) suggests the presence of persistent X-ray emission more or less homogeneously distributed in arrival time and not flaring emission as – for example – observed in a number of brown dwarf ONC members (Preibisch et al. 2005) or the ultra cool dwarf LHS 2065 (Schmitt & Liefke 2002).

¹ <http://simbad.u-strasbg.fr/simbad/>

² <http://nedwww.ipac.caltech.edu/>

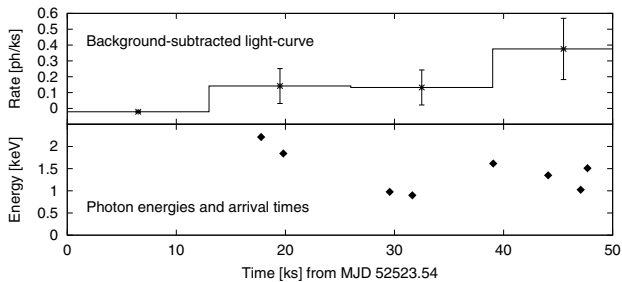


Fig. 2. *Upper panel:* background-subtracted 0.5–2.5 keV band light curve (13 ks binning). *Lower panel:* photon energy against arrival time.

2.2. The XMM-Newton data

As 2MASS 0535-0546 is clearly detected in the *Chandra* data, we searched for further evidence in other serendipitous X-ray observations. In an XMM-Newton observation of ι Orionis 2MASS 0535-0546 is located roughly 9 arcmin off-axis and we perform a similar analysis as for the *Chandra* data, i.e., we define a source-free background region in the vicinity of 2MASS 0535-0546 and concentrate on the energy range 0.5–2.5 keV. We calculate the excess counts in a circular region with a radius of 15 arcsec (to take into account the larger XMM-Newton PSF) around the nominal source position.

While in the *Chandra* image 2MASS 0535-0546 is clearly separated from all neighboring sources (see Fig. 1), we can unfortunately not exclude some contamination from close-by sources in the XMM-Newton data. Furthermore, in the image constructed from the pn data (i.e., the most sensitive instrument onboard XMM-Newton) the readout strip generated by the out of time events from the central bright source (ι Orionis) is located less than one arcmin from 2MASS 0535-0546 providing yet an additional source of possible contamination. Momentarily neglecting these problems, we find 8 ± 4 , 7 ± 4 and 13 ± 6 excess photons above the background for the MOS 1, MOS 2, and pn, data respectively. Converting into count rates and fluxes using the same model as for the *Chandra* photons (cf. Sect. 2.1) and a vignetting factor of 0.6 (see XMM-Newton-Users Handbook Sect. 3.2.2.2), we find a value of $(14.0 \pm 4.0) \times 10^{28}$ erg/s for the averaged X-ray luminosity in the MOS 1, MOS 2, and pn data using WebPIMMS³. This is a factor of five higher than the X-ray flux from 2MASS 0535-0546 observed with *Chandra*. If we now estimate the contamination level of the source region by placing a similarly sized region at a comparable position with respect to the neighboring, contaminating sources, the observed flux level decreases to values roughly consistent with the *Chandra* measured flux. Although the XMM-Newton data alone are insufficient to claim a detection, we conclude that they are at least consistent with the assumption of X-ray emission from 2MASS 0535-0546 at the same level as observed with *Chandra*, and from an inspection of the arrival times of individual photons we can also exclude the presence of (stronger) flares.

2.3. Phase coverage of X-ray observations

In Fig. 3 we show the phase folded optical light curve of 2MASS 0535-0546 as given by Stassun et al. (2006), where we indicate those phase intervals covered either by XMM-Newton or *Chandra*. The XMM-Newton observation

³ <http://heasarc.nasa.gov/Tools/w3pimms.html>

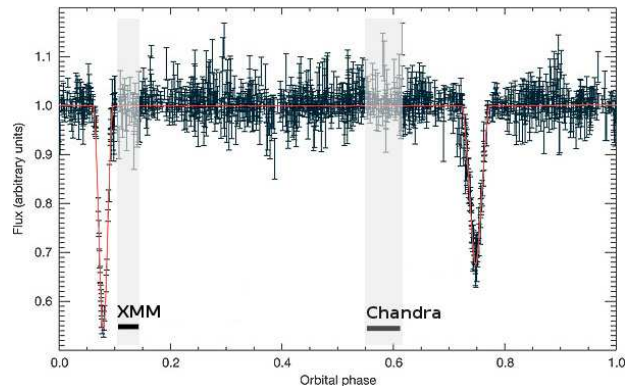


Fig. 3. Phase folded photometric data from Stassun et al. (2006). Observation phases of *Chandra* and XMM-Newton are indicated by black bars at the bottom and a gray column.

takes place shortly after the eclipse of the secondary, but unfortunately, none of the eclipses is covered by the presently available X-ray data. Therefore, we are unable to unambiguously attribute the detected X-ray emission to any of the individual components of 2MASS 0535-0546, which is clearly a task for follow-up observations.

2.4. Chromospheric and coronal activity

The bolometric luminosity, L_{bol} , of the individual components can be calculated from

$$L_{\text{bol}} = 4\pi r^2 \sigma T^4, \quad (1)$$

with r denoting the radius of the brown dwarf, σ the Stefan-Boltzmann constant, and T the effective temperature. Using the values given by Stassun et al. (2007) for the radii and temperatures of 2700 K and 2800 K, we find bolometric luminosities of 8×10^{31} erg/s and 5.1×10^{31} erg/s for the primary and secondary component.

As the primary shows strong magnetic activity (Reiners et al. 2007), we naturally blame it to be also responsible for the X-ray emission. Comparing the X-ray luminosity of 3×10^{28} erg/s to its bolometric luminosity leads to a ratio of $\log L_X/L_{\text{bol}} = -3.4$, and similar results of -3.2 and -3.6 are obtained if not the primary but the secondary or both were the X-ray bright component(s).

Preibisch et al. (2005) detected quiescent emission from 8 young brown dwarfs in the ONC. We find that both the X-ray luminosity of 2MASS 0535-0546 and the $\log L_X/L_{\text{bol}}$ -ratio (no matter whether the primary or the secondary is held responsible for the X-ray emission) point to a rather active, however, not unprecedented object. From the activity point of view, it appears similar to the late M dwarf 2MASS J05350705-0525005 (COUP 280), which is the most active brown dwarf in the (quiescent) Preibisch et al. (2005) sample showing an $\log L_X/L_{\text{bol}}$ -ratio of -3.3 ; with an X-ray luminosity of 5×10^{28} erg/s it is also among the most luminous. This provides further support for our attribution of the recorded X-ray flux to the 2MASS 0535-0546 system.

What do these outcomes imply for the relation between chromospheric and coronal activity in 2MASS 0535-0546? Reiners et al. (2007) derive values of $\log(L_{\text{H}\alpha}/L_{\text{bol}}) = -3.5$ for the primary and $\log(L_{\text{H}\alpha}/L_{\text{bol}}) = -4.3$ for the secondary. Substituting our results we obtain $\log(L_X/L_{\text{H}\alpha}) = 0.1$ if the primary were the X-ray bright constituent and $\log(L_X/L_{\text{H}\alpha}) = 0.7$ if it is the secondary.

These values compare well to those given by Dahm et al. (2007) for similarly young low-mass ($M < 0.5 M_{\odot}$) classical and weak-line T-Tauri stars in NGC 2264, and are also within the range of $\log(L_X/L_{Ha})$ -ratios obtained by Hawley et al. (1996) for active cluster and field M-dwarfs in a more advanced evolutionary state.

3. Summary and conclusions

In summary, we find an unambiguous X-ray detection of the eclipsing brown-dwarf binary 2MASS 0535-0546. An X-ray source at the nominal position of 2MASS 0535-0546 is clearly seen with the *Chandra* observatory, and the results are also compatible with an XMM-*Newton* image observed about one year earlier. The X-ray luminosity of 2MASS 0535-0546 is of the order of 3×10^{28} erg/s, and even though the *Chandra* light curve might indicate some moderate increase in luminosity, no flaring activity is seen in either of the observations. Therefore, we attribute the flux to quiescent X-ray emission.

An inspection of the source photons recorded by *Chandra* shows that the observed plasma emits at a temperature of at least 1 keV and probably more. The relative hardness of the spectrum is compatible with the results obtained by Stelzer & Micela (2007) for a wide and similarly young brown-dwarf binary system. From the bolometric luminosity of the primary component we compute a value of -3.4 for the $\log(L_X/L_{bol})$ -ratio, which is close to the saturation limit of ≈ -3 and within the range of values determined by Preibisch et al. (2005) for other brown dwarf members of the ONC detected in quiescence as well as compatible with values computed by Stelzer et al. (2006) for other young brown dwarfs. Invoking the findings of Reiners et al. (2007) we find $\log(L_X/L_{Ha})$ values well consistent with previously published results for low-mass stars. Unfortunately, none of the optical eclipses is covered by the available X-ray data, so we have no way at the moment to assign the X-ray flux to the individual components of 2MASS 0535-0546.

What can our results tell us about the origin of the temperature reversal? The effect may be caused either by a non-coeval formation of the brown dwarfs or by the impact of magnetic fields, which hamper energy transport by convection. The X-ray detection of 2MASS 0535-0546 alone supports the presence of magnetic fields causing the X-ray emission; further evidence is the hardness of the source photons indicating that magnetic processes are the source of the activity. Our results are, therefore, fully in line with those of Reiners et al. (2007), pointing towards the presence of strong magnetic activity in 2MASS 0535-0546 near the saturation limit and hence a magnetic origin of the observed temperature reversal.

Acknowledgements. This work has made use of data obtained from the *Chandra* and XMM-*Newton* data archives. S.C. acknowledges support from the DLR under grant 50OR0105. P.C.S. acknowledges support from the DLR under grant 50OR703.

References

- Dahm, S. E., Simon, T., Proszkow, E. M., & Patten, B. M. 2007, *AJ*, 134, 999
 Fleming, T. A., Giampapa, M. S., Schmitt, J. H. M. M., & Bookbinder, J. A. 1993, *ApJ*, 410, 387
 Gizis, J. E., Monet, D. G., Reid, I. N., et al. 2000, *AJ*, 120, 1085
 Hawley, S. L., Gizis, J. E., & Reid, I. N. 1996, *AJ*, 112, 2799
 Mohanty, S., Basri, G., Shu, F., Allard, F., & Chabrier, G. 2002, *ApJ*, 571, 469
 Neuhauser, R., & Comeron, F. 1998, *Science*, 282, 83
 Predehl, P., & Schmitt, J. H. M. M. 1995, *A&A*, 293, 889
 Preibisch, T., McCaughrean, M. J., Grosso, N., et al. 2005, *ApJS*, 160, 582
 Reiners, A., Seifahrt, A., Stassun, K. G., Melo, C., & Mathieu, R. D. 2007, *ApJ*, 671, L149
 Robrade, J., & Schmitt, J. H. M. M. 2008, *ArXiv e-prints*, 806
 Schmitt, J. H. M. M. 1997, *A&A*, 318, 215
 Schmitt, J. H. M. M., & Liefke, C. 2002, *A&A*, 382, L9
 Stassun, K. G., Mathieu, R. D., & Valenti, J. A. 2006, *Nature*, 440, 311
 Stassun, K. G., Mathieu, R. D., & Valenti, J. A. 2007, *ApJ*, 664, 1154
 Stelzer, B. 2004, *ApJ*, 615, L153
 Stelzer, B., & Micela, G. 2007, *A&A*, 474, 129
 Stelzer, B., Micela, G., Flaccomio, E., Neuhauser, R., & Jayawardhana, R. 2006, *A&A*, 448, 293

4 Summary and conclusion

In this thesis, stellar activity was investigated from several points of view, making use of different observation techniques and facilities.

In the first part, it was demonstrated what amount of information can be extracted from light curves of planetary eclipses. While the main target of the ongoing transit surveys is finding unknown planets, we developed a new technique to use the same data to investigate the host stars of transiting planets. The technique was demonstrated using the data of the milestone system CoRoT-2, a particularly active star orbited by a close-in Jovian planet.

In a first step, my coworkers and I revisited the planetary parameters derived by transit modeling taking stellar activity into account. We came to the conclusion that the activity of the host star leaves detectable traces in the transit light curves, and that these cannot generally be neglected when the planetary parameters are determined; at least, if the values are to be accurate to more than a few percent.

In a second step, we applied a novel light-curve inversion technique to reconstruct the surface brightness distribution and its evolution on the host star in two observationally separate regions; the first is given by the surface fraction recurrently eclipsed by the planet and the second covers the entire rest. The map of the noneclipsed section shows that the centers of spot coverage alternate between opposing hemispheres of CoRoT-2a, which may be explained by differential rotation, the flip-flop phenomenon, or a combination of both. The map corresponds well to previously published results, which were obtained using maximum entropy regularizations. The map of the eclipsed section shows a relatively stable configuration with two active regions about 180° apart, fitting well into the picture of a star with two active longitudes already suggested by the map of the noneclipsed section.

While our analysis clearly shows the intricacies for the determination of planetary parameters introduced by activity, it also reveals that a lot of valuable information can be extracted

from the photometry of active stars and, in particular, those active stars with transiting planets.

In the second part of the thesis, I left the field of planet research and concentrated on X-ray emission of young stars, which may, right now, be in the process of forming planets.

Many young stars are known to be powerful X-ray emitters and are surrounded by substantial amounts of circumstellar material in the form of accretion disks and envelopes. The disks are believed to be the birthplace of planets, and a good understanding of planet formation, therefore, requires knowledge of the disks.

The fluorescent Fe K_α I line represents one of the few possibilities to study cool material in the X-ray regime, and the geometry of circumstellar disks makes them a particularly promising target for Fe K_α I line studies. However, before definite conclusions on the disk geometry and state can be drawn from such analyses, the creation mechanism of the Fe K_α I line has to be understood precisely. In this thesis, fluorescent Fe K_α I line emission of young stars in Orion was investigated with a special emphasis on its temporal evolution. The most widely accepted creation scenario attributes the Fe K_α I line emission to photoelectric excitation of neutral or lowly ionized iron by X-rays and, thus, suggests a temporal correlation of high energy X-ray continuum and Fe K_α I line emission. While this was found to be true in many cases, some examples were presented, which seem to contradict this scenario. The results indicate that either another excitation mechanism, such as electron excitation, is responsible for these observations, or more complicated geometries must be taken into account to explain the observations. A decisive answer cannot be given using the data at hand, and will probably have to await the next generation of X-ray observatories.

On the mass scale, brown dwarfs lie between planets and stars. Their low luminosity impedes detailed studies so that many facets of their formation and evolution remain elusive. We reported on the X-ray detection of the first eclipsing brown dwarf binary. As has become clear, eclipses are a powerful tool, which, in

this case, allowed the determination of accurate brown dwarf radii and temperatures for the first time. Surprisingly, the structure of the system, most notably the observed temperature reversal, is not compatible with conventional evolutionary tracks, which is probably related to the presence of the magnetic field, also believed to be responsible for the X-ray emission. Unfortunately, it is hardly possible to assign the X-ray emission to one of the constituents (or both) by observing an eclipse with the currently available X-ray instrumentation, because the flux is too low. Nonetheless, this X-ray detection underlines the importance of magnetic phenomena during the early phases of (sub)stellar evolution.

5 Outlook

A major part of this thesis focuses on the Fe K $_{\alpha}$ I line observed in young stars in Orion. The work concentrated first on a detection of the line and second on its temporal behavior. Already the analysis of these basic line properties is complicated, because usually only a low number of line photons is detected. The Fe K $_{\alpha}$ I line lies at an energy not favored by the effective area and resolving power of today's X-ray observatories. The enormous power of an analysis of its profile can today only be exploited in the case of active galactic nuclei, where the distortion is extreme due to relativistic effects and much more distinct than in stars.

A higher sensitivity and about an order of magnitude enhancement in resolution at the Fe K $_{\alpha}$ I line energy is envisaged by using a new kind of astronomical X-ray detector, namely a bolometer. A bolometric detector was already part of the *Suzaku* mission launched in 2005, where it, unfortunately, failed. While the current detectors on board *Chandra* and XMM-*Newton* will still allow for some progress in stellar Fe K $_{\alpha}$ I line research, the next big step, in my opinion, will have to await the advent of an observatory equipped with a bolometric detector or some instrument with similar capabilities. This will allow to study the line strength

and temporal behavior as well as the line profile in much more detail.

The line profile will provide us with new insights into the nature of the reprocessing material such as its ionization fraction, velocity dispersion, and composition. A larger signal will also allow a more detailed study of the temporal association of Fe K $_{\alpha}$ I line flux and continuum flux, yielding a more decisive answer on the question whether photoelectric excitation is the only creation mechanism responsible for Fe K $_{\alpha}$ I line emission.

Far from stagnation, the field of planetary science has recently been boosted by the successful launch of Kepler and CoRoT, two space-based observatories providing photometric data of unparalleled quality. Doubtlessly targeted at finding a second Earth, the data gathered by these instruments is also very interesting in the context of stellar activity as the brightness of thousands of stars is continuously monitored for months. The work carried out in the frame of this thesis concentrated on a single, even though outstanding, target. In future analyses it will be possible to study further single targets as well as large samples of objects, using high accuracy, short cadence data extending for years.

These analyses will significantly contribute to answering key questions of starspot research; to name but a few: Which stars show spots and what is the coverage fraction? What are the spot temperatures and lifetimes? The long-time, short cadence monitoring provided by the space-based missions offers a great opportunity to study the surface evolution of active stars in great detail, and it will help to gain more insight into the distribution and nature of active longitudes and the flip-flop effect. This, in turn, allows to refine theories of the stellar dynamo.

A question also particularly interesting during the search for extrasolar planets of low mass is how stellar activity influences the observed radial velocity signals, and whether the activity signature can be modeled so that more accurate radial velocity curves can be derived.

Beyond all those excellent scientific opportunities, I will not forget to mention that the discovery of a second Earth, may elevate the

public attention and acceptance gained by astronomy to a level perhaps last reached by astrology.

5.1 Projects in progress

The space of further work is vast, but a number of projects have already been started by my coworkers and me personally.

In response to the results of the Fe K_{α} I line searches, I started modeling the influence of absorbing material on the X-ray Fe K_{α} I line and search for possibilities to increase the observed equivalent width using photoexcitation.

A numerical code is being build up to study the influence of starspots on the apparent radial velocity shifts of stars. Spectroscopic observation are envisaged, which are to be carried out simultaneously with the Kepler photometric measurements, so that the information contained in high resolution spectra and high accuracy photometry can be combined.

A number of spectroscopic follow-up observations of stars showing a similar light curve as that of CoRoT-2, however, without transits, were successfully proposed to gain further insight into the nature of these objects. In particular, these observations will allow us to derive the spectral type, luminosity class, and the strength and variability of several activity indicators, providing us with valuable information on the class of stars showing these characteristic light curves.

Finally, a series of VLT UVES spectra of CoRoT-2, proposed by U. Wolter and observed by K.F. Huber, was obtained, which is currently analyzed to investigate the transit in even more detail.

References

- Auvergne, M., Bodin, P., Boisnard, L., et al. 2009, *A&A*, 506, 411
- Baliunas, S. L., Donahue, R. A., Soon, W. H., et al. 1995, *ApJ*, 438, 269
- Berdyugina, S. V. 2005, "Living Rev. Solar Phys., 2, (2005), 2. [Online Article]: 11.05.2010"
- Berdyugina, S. V., Pelt, J., & Tuominen, I. 2002, *A&A*, 394, 505
- Berger, E., Gizis, J. E., Giampapa, M. S., et al. 2008, *ApJ*, 673, 1080
- Berghoefer, T. W., Schmitt, J. H. M. M., & Cassinelli, J. P. 1996, *A&AS*, 118, 481
- Bohlin, J. D., Vogel, S. N., Purcell, J. D., et al. 1975, *ApJ*, 197, L133
- Burnight, T. R. 1949, *Phys. Rev.*, 76, 165
- Catalano, S., Biazzo, K., Frasca, A., & Marilli, E. 2002, *A&A*, 394, 1009
- Catura, R. C., Acton, L. W., & Johnson, H. M. 1975, *ApJ*, 196, L47
- Czesla, S., Huber, K. F., Wolter, U., Schröter, S., & Schmitt, J. H. M. M. 2009, *A&A*, 505, 1277
- Czesla, S. & Schmitt, J. H. M. M. 2007a, *A&A*, 465, 493
- Czesla, S. & Schmitt, J. H. M. M. 2007b, *A&A*, 470, L13
- Czesla, S., Schneider, P. C., & Schmitt, J. H. M. M. 2008, *A&A*, 491, 851
- Deutsch, A. J. 1958, in *IAU Symposium*, Vol. 6, *Electromagnetic Phenomena in Cosmical Physics*, ed. B. Lehnert, 209–+
- Donati, J., Semel, M., & Praderie, F. 1989, *A&A*, 225, 467
- Fan, Y. 2009, "Living Rev. Solar Phys., 6, (2009), 2. [Online Article]: 04.05.2010"
- Feigelson, E. D. & Decampli, W. M. 1981, *ApJ*, 243, L89
- Feigelson, E. D., Getman, K., Townsley, L., et al. 2005, *ApJS*, 160, 379
- Fleming, T. A., Giampapa, M. S., & Garza, D. 2003, *ApJ*, 594, 982
- Fleming, T. A., Giampapa, M. S., & Schmitt, J. H. M. M. 2000, *ApJ*, 533, 372
- Fleming, T. A., Schmitt, J. H. M. M., & Giampapa, M. S. 1995, *ApJ*, 450, 401
- Getman, K. V., Feigelson, E. D., Grosso, N., et al. 2005a, *ApJS*, 160, 353
- Getman, K. V., Flaccomio, E., Broos, P. S., et al. 2005b, *ApJS*, 160, 319
- Giacconi, R. 2003, *Reviews of Modern Physics*, 75, 995
- Giacconi, R., Gursky, H., Paolini, F. R., & Rossi, B. B. 1962, *Physical Review Letters*, 9, 439
- Gray, D. F. 1996, in *IAU Symposium*, Vol. 176, *Stellar Surface Structure*, ed. K. G. Strassmeier & J. L. Linsky, 227–+
- Güdel, M., Briggs, K. R., Arzner, K., et al. 2007, *A&A*, 468, 353
- Hall, D. S. 1994, *International Amateur-Professional Photoelectric Photometry Communications*, 54, 1
- Hall, J. C. 2008, "Living Rev. Solar Phys., 5, (2008), 2. [Online Article]: 27.03.2010"
- Hatzes, A. P. 1995, *ApJ*, 451, 784
- Henry, G. W., Eaton, J. A., Hamer, J., & Hall, D. S. 1995, *ApJS*, 97, 513
- Huber, K. F., Czesla, S., Wolter, U., & Schmitt, J. H. M. M. 2009a, *A&A*, 508, 901
- Huber, K. F., Czesla, S., Wolter, U., & Schmitt, J. H. M. M. 2010, *A&A*, 514, A39+
- Huber, K. F., Wolter, U., Czesla, S., et al. 2009b, *A&A*, 501, 715

- Hünsch, M., Schmitt, J. H. M. M., Sterzik, M. F., & Voges, W. 1999, *A&AS*, 135, 319
- Hünsch, M., Schmitt, J. H. M. M., & Voges, W. 1998a, *A&AS*, 127, 251
- Hünsch, M., Schmitt, J. H. M. M., & Voges, W. 1998b, *A&AS*, 132, 155
- Jetsu, L., Pelt, J., & Tuominen, I. 1993, *A&A*, 278, 449
- Kron, G. E. 1947, *PASP*, 59, 261
- Lucy, L. B. & White, R. L. 1980, *ApJ*, 241, 300
- Mandel, K. & Agol, E. 2002, *ApJ*, 580, L171
- Mayor, M. & Queloz, D. 1995, *Nature*, 378, 355
- McKee, C. F. & Ostriker, E. C. 2007, *ARA&A*, 45, 565
- Mewe, R., Heise, J., Gronenschild, E. H. B. M., et al. 1975, *ApJ*, 202, L67
- O’Neal, D., Saar, S. H., & Neff, J. E. 1996, *ApJ*, 463, 766
- Parker, E. N. 1955a, *ApJ*, 122, 293
- Parker, E. N. 1955b, *ApJ*, 121, 491
- Piskunov, N. E., Tuominen, I., & Vilhu, O. 1990, *A&A*, 230, 363
- Preibisch, T., Kim, Y., Favata, F., et al. 2005, *ApJS*, 160, 401
- Priest, E. & Forbes, T. 2000, *Magnetic Reconnection*, ed. Priest, E. & Forbes, T.
- Radick, R. R., Lockwood, G. W., Skiff, B. A., & Baliunas, S. L. 1998, *ApJS*, 118, 239
- Radick, R. R., Mihalas, D., Lockwood, G. W., et al. 1983, *PASP*, 95, 621
- Rebolo, R., Osorio, M. R. Z., & Martín, E. L. 1995, *Nature*, 377, 129
- Roberts, W. O. 1945, *ApJ*, 101, 136
- Robrade, J., Poppenhaeger, K., & Schmitt, J. H. M. M. 2010, *A&A*, 513, A12+
- Robrade, J. & Schmitt, J. H. M. M. 2008, *A&A*, 487, 1139
- Robrade, J. & Schmitt, J. H. M. M. 2009, *A&A*, 496, 229
- Rodono, M., Cutispoto, G., Pazzani, V., et al. 1986, *A&A*, 165, 135
- Rosner, R., Tucker, W. H., & Vaiana, G. S. 1978, *ApJ*, 220, 643
- Rutledge, R. E., Basri, G., Martín, E. L., & Bildsten, L. 2000, *ApJ*, 538, L141
- Schmitt, J. H. M. M. 1997, *A&A*, 318, 215
- Schmitt, J. H. M. M., Fleming, T. A., & Giampapa, M. S. 1995, *ApJ*, 450, 392
- Schmitt, J. H. M. M. & Liefke, C. 2002, *A&A*, 382, L9
- Semel, M., Donati, J., & Rees, D. E. 1993, *A&A*, 278, 231
- Silva, A. V. R. 2003, *ApJ*, 585, L147
- Skumanich, A. 1972, *ApJ*, 171, 565
- Solanki, S. K. 2003, *A&A Rev.*, 11, 153
- Stassun, K. G., Mathieu, R. D., & Valenti, J. A. 2006, *Nature*, 440, 311
- Stokes, G. G. 1852, *Philosophical Transactions of the Royal Society of London*, 142, 463
- Strassmeier, K. G. 1999, *A&A*, 347, 225
- Strassmeier, K. G. 2009, *A&A Rev.*, 17, 251
- Struve, O. 1952, *The Observatory*, 72, 199
- Tas, G. & Evren, S. 2000, *Inform. Bull. Var. Stars*, 4992, 1
- Vaiana, G. S., Cassinelli, J. P., Fabbiano, G., et al. 1981, *ApJ*, 245, 163
- Vogt, S. S. 1979, *PASP*, 91, 616
- Vogt, S. S. 1981, *ApJ*, 250, 327
- Vogt, S. S., Penrod, G. D., & Hatzes, A. P. 1987, *ApJ*, 321, 496

- Wolter, H. 1952, *Annalen der Physik*, 445, 94
- Wolter, U., Schmitt, J. H. M. M., Huber, K. F.,
et al. 2009, *A&A*, 504, 561
- Young, J. S., Baldwin, J. E., Boysen, R. C.,
et al. 2000, *MNRAS*, 315, 635
- Zeilik, M., de Blasi, C., Rhodes, M., & Bud-
ding, E. 1988, *ApJ*, 332, 293
- Zombeck, M. V., Vaiana, G. S., Haggerty, R.,
et al. 1978, *ApJS*, 38, 69

Danksagung - Acknowledgements

I thank Astronomy and Astrophysics for the kind permission to reproduce the papers Czesla & Schmitt (2007b), Czesla et al. (2008), Czesla et al. (2009), Huber et al. (2009a), and Huber et al. (2010).

For the rest of this section I will switch to German.

In meinem bisherigen Leben war es mir vergönnt viele Menschen zu treffen, von denen ich viel gelernt habe. Den Wert und oft auch die Bedeutung dessen was sie mich gelehrt haben, habe ich jedoch oft erst später erkannt, und ich wünsche mir von Zeit zu Zeit diesen Menschen deutlicher dafür gedankt zu haben, was sie mir gegeben haben.

In der wahrscheinlich vergeblichen Hoffnung dieses jetzt zu vermeiden, möchte ich im Folgenden denen danken, die mich während der Anfertigung meiner Arbeit unterstützt haben.

Zuvorderst danke ich Prof. Schmitt dafür sein Wissen und seine Erfahrung mit mir geteilt zu haben. Ich danke ihm für seine fortwährende Unterstützung, seine Geduld und seinen Scharfsinn und möchte ihn wissen lassen, daß ich ihn sowohl als Wissenschaftler als auch als Menschen schätze.

Ich danke meinem Freund und Kollegen Klaus Huber ohne dessen Ideen, Visionen und Verstand diese Arbeit nicht möglich gewesen wäre.

Ich danke meinem Kollegen und Mitmusikliebhaber Uwe Wolter für viele Diskussionen und unzählige hilfreiche Anmerkungen, die mich vorangebracht haben.

Ich danke meinen Kollegen und Freunden Christian Schneider und Sebastian Schröter für ihre Beiträge und wertvolle Diskussionen.

Ferner möchte ich bei all meinen nicht namentlich aufgeführten Kollegen für ihre Unterstützung und ein wunderbares Arbeitsklima bedanken.

Die Liste derer denen ich zu danken habe, könnte nicht vollständig sein ohne meine Familie, insbesondere meiner Mutter Renate, meinem Vater Axel D. und meiner Schwester Sabine, ohne deren Unterstützung diese Arbeit nicht möglich gewesen wäre.

Besonderer Dank gilt auch meiner Freundin Maire für soviel was nicht hierhin gehört.